Laser developments and study of Rydberg and autoionizing Rydberg states in Tm, La and At using resonant ionization laser spectroscopy

by

Maryam Mostamand

A thesis submitted to the Faculty of Graduate Studies of
The University of Manitoba
in partial fulfillment of the requirements of the degree of

DOCTOR OF PHILOSOPHY

Department of Physics and Astronomy
University of Manitoba
Winnipeg

Abstract

The resonant ionization laser ion source is an element-selective, efficient and versatile ion source which generates radioactive ion beams at on-line mass separator facilities. Elements with complex atomic structures and incomplete spectroscopic data require ionization scheme development. A grating-tuned titanium:sapphire (Ti:Sa) laser was used in applications for spectroscopy studies. A regiment of automated and continuous frequency-doubled and frequency tripled scans was developed to investigate different energy regions and electronic configurations of the elements. An intra-cavity frequency doubled chromium:forsterite laser was built, to cover the spectral gap between the orange and red wavelengths as these are not attainable using Ti:Sa lasers. Laser resonance ionization spectroscopy has been performed on lanthanum (La) and thulium (Tm) at TRIUMF's off-line laser ion source test stand to identify the highest efficiency ionization scheme for delivery of radioactive ion beams. Upon identification of possible two-step Ti:Sa laser based ionization schemes, systematic laser resonance ionization spectroscopy was performed by conducting laser scans across Rydberg states, ionization potentials, and auto-ionizing states. The spectroscopy of high-lying Rydberg states and auto-ionizing Rydberg states allowed to confirm and remeasure the ionization potential of Tm and La atom with improved accuracy. In-source resonance ionization spectroscopy of the purely radioactive astatine (At) atom was performed at the ISAC/TRIUMF radioactive ion beam facility to search for an efficient ionization scheme throughout auto-ionizing states. Apart from developing and implementing resonance ionization spectroscopy (RIS) schemes for elements, the issue of isobaric contamination in radioactive ion beam (RIB) delivery was addressed. On the newly implemented ion guide laser ion source (IG-LIS) for isobarically pure

RIB, operating modes and parameters were being developed and optimized. Design improvements are being implemented into the prototype for more robust and efficient on-line operation, and based on simulation (SIMION 8.0.4) studies further refinements are being implemented on the quadrupole ion guide based IG-LIS and a higher efficiency octupole based IG-LIS is being proposed.

Dedicated to:

My beautiful mother Zahra,

my supportive brothers Mohamadreza and Alireza,

and the memory of my father Masoud who always inspired me.

Acknowledgements

I would like to thank everyone who helped me along the way. Whilst there are many who lent their hands in many ways, who supported me and offered assistance when I truly needed it, there are a few of note who come to mind. I deeply appreciate every contribution each person made along my journey, though specific mention goes to the following:

My entire family, including those in my dedication, for their ongoing support and love.

The University of Manitoba for the Graduate Fellowship that helped me with the financial support to pursue my PhD.

TRIUMF, for providing the opportunity to work at such an esteemed research lab, to meet amazing people, and for unforgettable travel opportunities.

Prof. Jens Lassen, TRIUMF's 2019 Winner of the Award for best Mentor, for truly being the best mentor. Jens was my supervisor and guide, the most influential in my PhD, and the backbone of my doctoral studies.

Prof. Gerald Gwinner, the ol' Winner, for also being my supervisor, for being my advocate at the University, my tether, and my liaison for all University matters. Also, for some great meals along the way.

Dr. Ruhong Li, my teammate, colleague and confidant, for her instruction, insight, friendship, and for lending a helping hand throughout my research, and our group experiments.

Silke Bergelt-Bruckner, my point person at TRIUMF, who was also a mentor, guide, and confidant as well, but who first helped me getting settled into Vancouver in my earliest days, in finding accommodation, and learning the ins and outs and inner-workings of TRIUMF.

Susan Beshta, another liaison and advocate of mine at the university, for always helping me navigate the maze of administrative processes.

Tatjana, Mary, and their cats, for opening their home to me in my first two semesters in the ice-farm of Winnipeg.

Contents

List of Tables

List of Figures

1 | Introduction

A radioactive ion beam (RIB) is an ensemble of radioactive charged particles with a well defined velocity. Such beams are used for instance in astrophysics, nuclear- and atomic-physics, material- and medical-science experiments. The required beam energies for these experiments range from a few eV/u for atomic physics to MeV/u for inelastic scattering cross section measurements in nuclear physics. The RIB production techniques typically produce multiple radioactive species. Mass selection techniques are necessary to select out (purify) the isotope of interest from isobaric contamination. Recent developments seek to improve beam purity without sacrificing beam intensity.

There are two commonly used methods for RIB production called "in-flight" and "ISOL" [1]. Both production methods have in common an accelerator for the primary beam, a production target and a separation facility for the selection of the secondary radioactive beam of interest.

The in-flight (IF) or fragmentation method uses accelerated heavy ions impinging on a thin target. The production process for the in-flight occurs via projectile fragmentation, nucleon transfer, fission and Coulomb excitation [2] and can make use of nuclear reactions to enhance the production of a specific species. In this case the primary beam is a heavy ion, like ^{238}U, ^{208}Pb, or ^{197}Au, that is accelerated at high energies in the order of MeV/u. This type of RIB production has been used in IGISOL facilities (Louvain-la-Neuve, JYFL) as well as the higher energy facilities like GANIL in France, GSI in Germany, RIKEN in Japan [3], and the new Facility for Rare Isotope Beam (FRIB) at Mitchigan State University (MSU) [4].

The typical transverse emittance and energy spread for the in-flight method is poor compared to what an on-line ion source can typically produce [5–7]. On the other hand, this method is a fast production method that allows the delivery of isotopes with half-lives, down to μs [8], where the limitation is due to selection rather than production process. Beam intensities up to a few 10^{10} pps can be reached with the IF method at present.

The second production method is called Isotope Separator On-Line (ISOL) where light projectiles are accelerated toward a tick target. These light projectiles which are usually protons or deutrons, interact with the targets, heavy nuclei, producing radioactive isotopes via spallation, fragmentation or induced fission. The target container is heated up to 2000 °C in order to allow the neutral radioactive atoms to diffuse out of the target material and effuse towards an ion source [9]. Here they are ionized and extracted at source potential up to a few tens of kV. Different types of ion sources can be used depending on the atomic species [10]. The simplest is the surface source [11] which works efficiently for elements with low ionization potential (~ below 6 eV). Other sources include: plasma and electron impact (EI) ion sources like the FEBIAD [1] [12], Electron Cyclotron Resonance (ECR) [13] and Laser Ion Source (LIS) [14].

The produced beam has to be at high quality and small transverse emittance. The energy spread out of the source is in the order of few eV. Singly-charged ions are then extracted from the ion source and transported to a dipole magnet (mass separator) where the isotope of interest can be selected. The beam can be delivered at energies as low as 10 keV. Post-acceleration might be needed in order to reach energies up to 20 MeV/u. The ISOL method is limited in terms of half-lives (down to ms) and to non-refractory species. The relatively slow extraction process limits the possibility of extracting isotopes with few ms. Often RIB intensities up to of few 10^3 pps are produced. Facilities where the ISOL method is used include ISOLDE-CERN in Switzerland, GANIL and IPN in France, and TRIUMF in Canada, where the research for this work was conducted. A more detailed description of the RIB production and delivery at TRIUMF's Isotope Separator and ACcelerator (ISAC) facility is given in the following section.

[1] Forced Electron Beam Induced Arc Discharge

1.1 The isotope separator and accelerator (ISAC) facility at TRIUMF

RIBs are produced in the ISAC facility at TRIUMF using the ISOL method. An overview of the ISAC facility is given in Figure 1.1 with the three highlighted experimental areas.

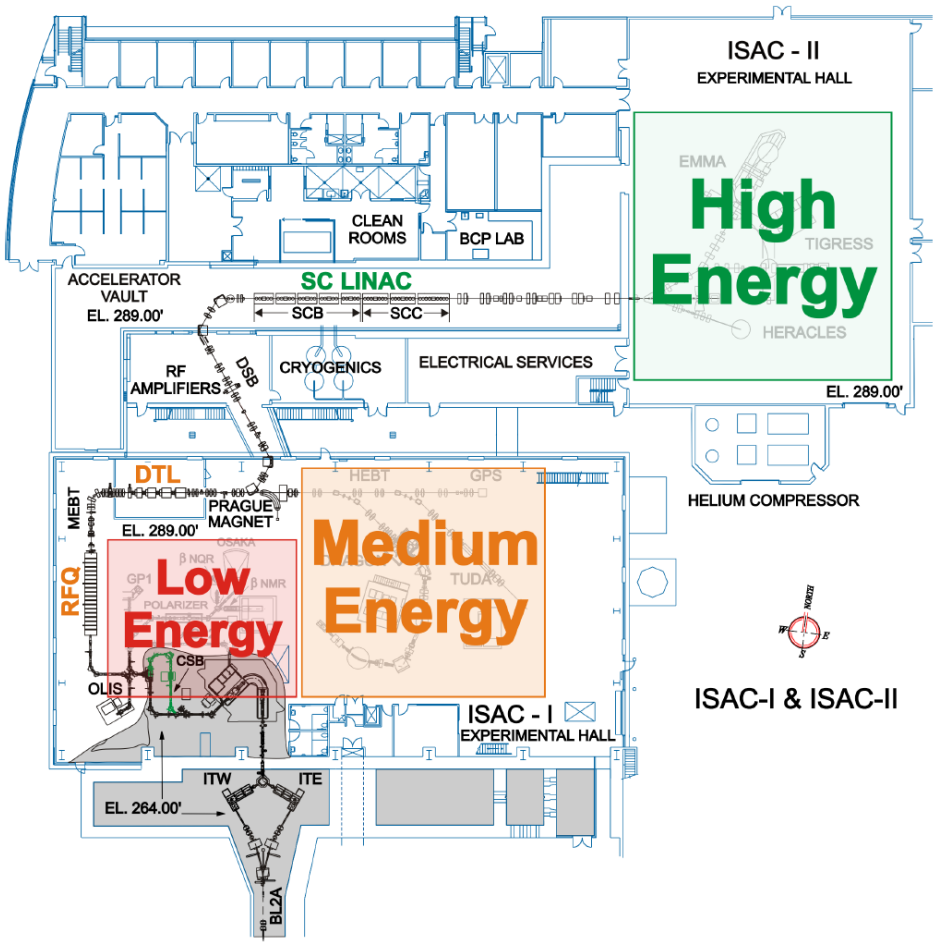

Figure 1.1: ISAC facility at TRIUMF. The three experimental areas (low, medium and high energy) are highlighted [15].

The TRIUMF cyclotron accelerates H^- ions up to an intensity of 300 μA to a maximum energy of 500 MeV. In order to extract protons, the H^- ions are intercepted with a thin carbon foil resulting in the stripping of the electrons; the resulting H^+ beam is extracted. Thin stripper foils allow for partial stripping and simultaneous extraction of multiple p^+ beams. By choosing the location of

the stripper foils in the cyclotron, the p^+ beam energy can be selected. At ISAC the protons are delivered at 480 MeV with up to 100 μA of current. This proton beam can be directed to one of two independent ISAC target stations, EAST (ITE) and WEST (ITW), as shown in Figure 1.2. RIB from the target stations at ISAC are directed to a main mass-separator magnet through a magnetic switch yard dipole magnet. This switch yard magnet also serves as a low resolution mass-separator magnet (resolution R $\sim$ 300). Isotope separation is performed by a second dipole magnet, mass separator, operating at a resolving power of up to R $\approx$ 2000. This resolution allows for some isobar separation in the light atomic mass region, however, it only allows for isotope separation in the heavy atomic mass region as R:= m/Δm.

The target container is a 20 cm long and 19 mm diameter tantalum tube, containing a stack of D-shaped foils of the target material. Figure 1.3 is a schematic drawing of the ISAC surface ion source (SIS) with a high power target. Rare isotopes are produced by different nuclear reactions from the accelerated proton beam interacting with the target material atoms. Once the isotopes are produced and have migrated from the target container to the transfer tube, the isotope of interest needs to be ionized for extraction, transport, further mass separation, and possibly post acceleration. Three different ion sources: SIS, TRIUMF's Resonant Ionization Laser Ion Source (TRILIS) and FEBIAD, are available at ISAC. Each of these ion sources is particularly suited to limit a specific group of elements.

Particles that get in contact with a hot surface have probability that they desorb from the surface in a certain charge state. This effect can be used for positive as well as negative ion production and is known as surface ionization. Only positive ions are extracted at the ISAC facility. Surface ionization is the most common ionization method for elements with low ionization potential (IP $\leq$ 6 eV) such as the alkali metals, heavy alkali earth metals, lanthanides, and actinides. However, this ionization mechanism is not element selective. To date the only ion source at ISAC that can selectively ionize a chosen chemical element is the resonant ionization laser ion source (RILIS).

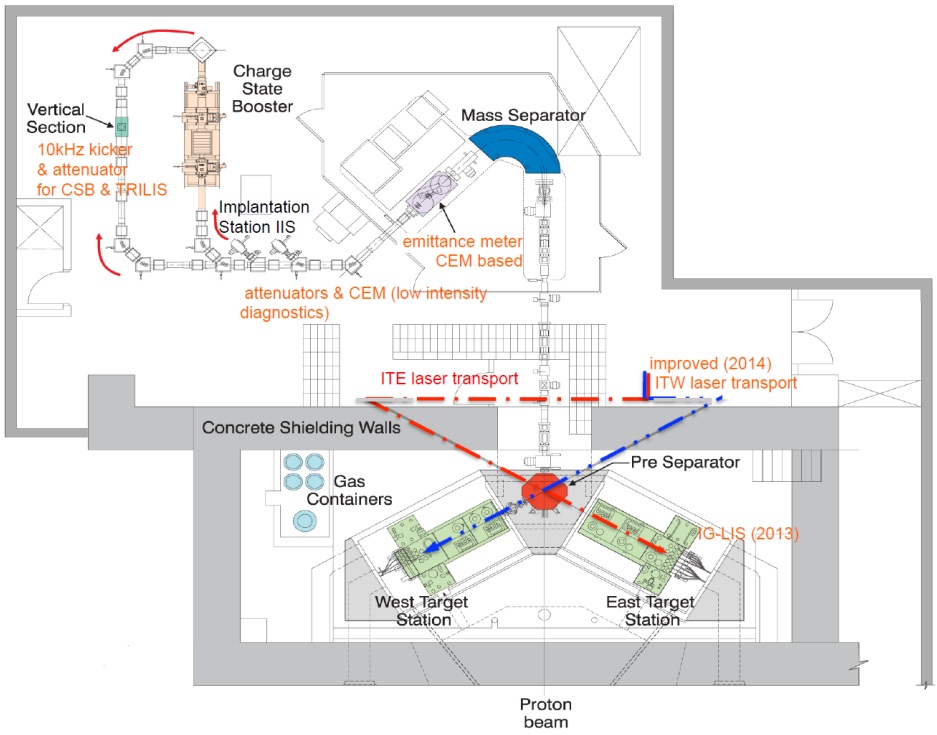

Figure 1.2: Laser beam transport in the mass separator area. Dedicated anti-reflection coated lens in each beam path focuses the laser beam into the ion source region [16].

Because of its high degree of selectivity and efficiency as well as the great number of different beams available, it has become the most frequently used ion source at ISAC.

1.2 TRIUMF resonance ionization laser ion source TRILIS

Laser resonance ionization spectroscopy has been applied to study atomic structures, especially high-lying Rydberg and autoionizing (AI) states since 1970s [18]. With its inherent element-selective ionization, resonance ionization spectroscopy (RIS) has become widely used at various accelerator facilities to deliver isobar free radioactive beam to nuclear physics experiments. On-line RIS appeared on the scene in 1983, when this highly sensitive technique was applied at the ISOL facility at Gatchina (Russia) [19, 20]. Laser ion sources are based on the step-wise excitation of a valence electron until, in the ionization step, its energy is greater than its binding energy (the ionization potential of the given element). Ionization can be realized either resonantly into a

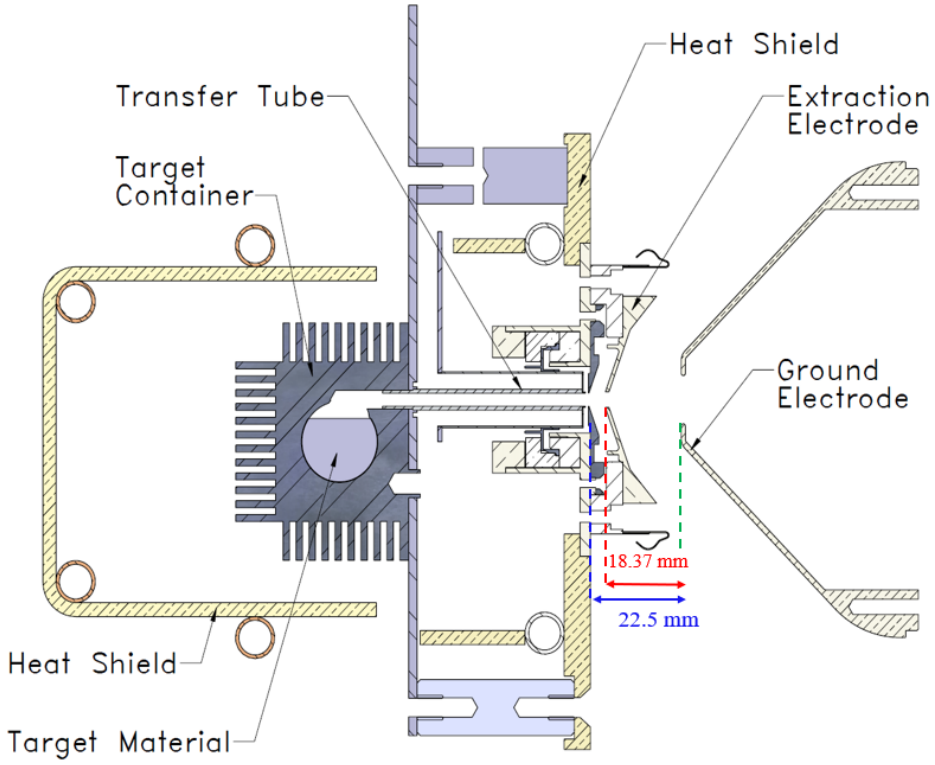

Figure 1.3: Schematic view of the surface ion source at ISAC [17]. It consists of a hot transfer tube connected to the target volume, to surface ionize the isotopes diffusing out from a heated target. An extraction electrode and a subsequent ground electrode then accelerate these ions to the desired energy. A Rhenium foil is rolled and inserted into the inner face of the transfer tube. This increases the work function and the ionization efficiency.

Rydberg or AI state or non-resonantly into the continuum by a high power laser; more details are given in Section 3.3.

Since 2003, titanium-doped sapphire (Ti:Sa) lasers were successfully tested at different radioactive ion beam facilities for their application as a laser ion source [21]. Tests were performed at TRIUMF-ISAC, ISOLDE (CERN, Geneva), IGISOL (Jyväskylä, Finland), ORNL-HRIBF (Oak-Ridge, USA). In the ISAC facility at TRIUMF, the RILIS has become one of the most subscribed ion source for RIB delivery. By now, at TRIUMF laser ionization schemes for 35 elements have been developed and used successfully on-line for beam delivery (Figure 1.4).

The TRILIS laser system is based on tunable Ti:Sa lasers pumped by a single or multiple, multimode, q-switched, frequency doubled Nd:YAG lasers (currently there are two Nd:YAG lasers, one is 50 W

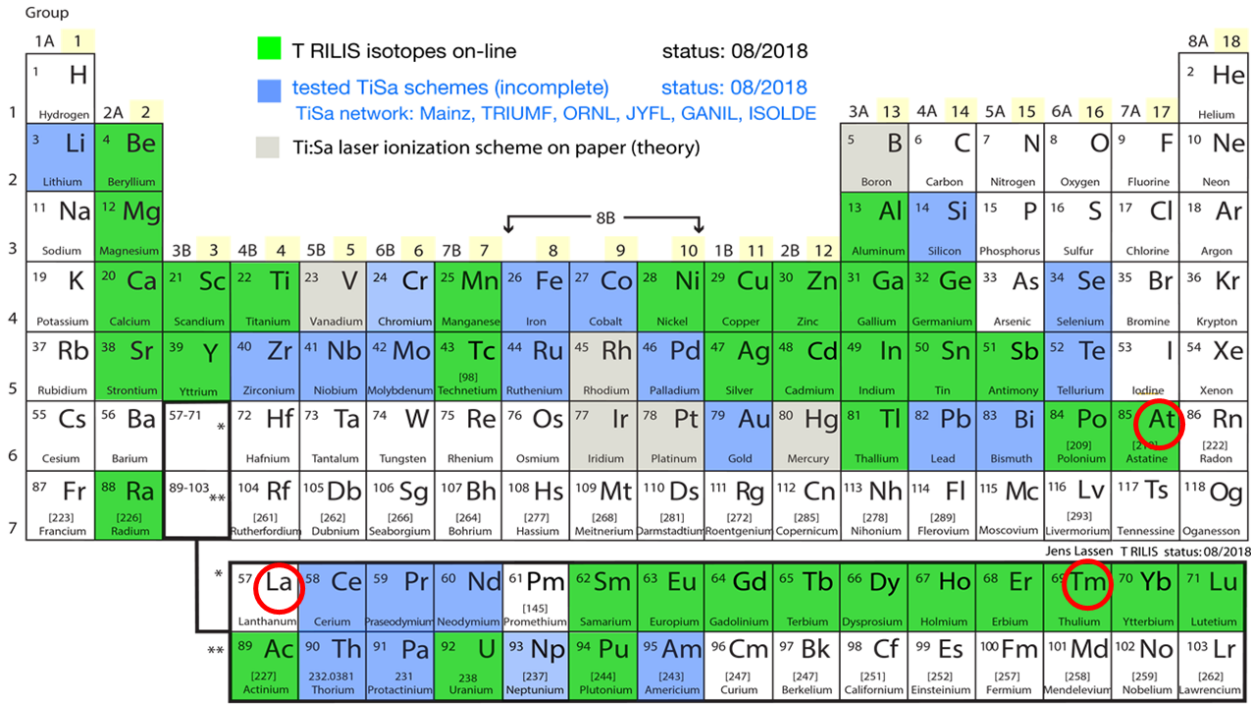

Figure 1.4: Elements delivered with the TRIUMF RILIS (status 08/2018) using Ti:Sa laser based resonance ionization. Isotopes from 35 different elements have been delivered on-line at ISAC with TRILIS so far. Detailed, up to date yield information is publicly available at http://mis.triumf.ca/science/planning/yield/beam. Red circles mark the elements studied in this work.

and the other is 100 W), typically operated at 10 kHz repetition rate. Currently five birefringent filter / Lyot filter (BRF) tuned Ti:Sa lasers with a tuning range from 680 nm-1000 nm are available. Shorter wavelength laser light can be generated by higher harmonic generation in non-linear crystals (e.g. BBO, S-LBO). The frequency coverage of the Ti:Sa laser system is thereby extended by intra-cavity frequency doubling, as well as external frequency doubling, tripling and quadrupling. For non-resonant ionization a frequency doubled Nd:YVO_4 laser provides a 532 nm light with an overall power of up to 6.7 W with 35 ns pulse length and an M^2 = 1.1 (quality factor of laser) at 10 kHz repetition rate. Temporal synchronization of the Ti:Sa lasers can be achieved by means of intra-cavity Pockels cells, which proved to be easier than adjusting the cavity build up time by means of the pump power and the Ti:Sa crystal position within the laser cavity. In order to maintain proper

spatial overlap of the laser beams in the ionization region during a long wavelength range scan, a commercial beam stabilization system [2] was employed.

The development of ionization schemes is usually performed off-line with either stable or long lived isotopes. The isotopes of short-lived elements cannot be studied off-line, therefore the required spectroscopy work has to be performed on-line. The spectroscopy on atomic species inside the ion source is called in-source spectroscopy. This method was demonstrated by in-source spectroscopy of astatine in this thesis (Chapter 9).

For the spectroscopy of Rydberg and autoionizing resonances and the development of new ionization schemes, a grating-tuned Ti:Sa laser was developed and applied as it allows for extended continuous frequency scans. The ionization potential of lanthanum and thulium were deduced from the analysis of observed Rydberg and AI Rydberg resonances.

1.3 Scope of the thesis

The goals for this dissertation, within the group's overall mission, were (0) characterization of an intra-cavity doubled CrFor laser system, to extend the wavelength reach of solid state lasers for RILIS applications, (1) to develop a resonant ionization scheme for Tm and La that can be used with the ion guide-laser ion source, (2) to develop optimized operating parameters and gain operational experience with the IG-LIS prototype and develop design criteria for the production type, on-line IG-LIS system, and (3) perform in-source laser resonance ionization spectroscopy on At.

The current development goal is to eliminate the need for non-resonant ionization in RILIS and to develop laser ionization schemes for all elements with improved ionization efficiency that can be implemented with solid state (Ti:Sa) laser systems only. Chapter 2 and Chapter 3 provide a detailed description about the theory of Rydberg atoms and the methods in resonance photo-ionization spectroscopy which was used in this work to analyze the atomic structure of Tm and La.

[2] BeamLock-TEM 4D

Further developments to laser systems, ion sources, and laser ionization schemes, including laser spectroscopy of highly excited atomic states and AI states must be done. To this end the ISAC-RILIS system shall be upgraded to enable accessing a wide range of wavelengths in atoms. TRILIS comprises Ti:Sa lasers [22] and higher harmonic generation. Current Ti:Sa laser system at TRIUMF as well as developments that was done as part of this work towards laser beam pointing stabilization during automatic scan across energy region of elements are elaborated in Chapter 4. The frequency doubling of a chromium-doped forsterite (Cr:Forsterite or Cr:Mg_2SiO_4) laser is the most promising option which would allow to extend the wavelengths available to solid state lasers based RILIS from ~ 590 nm to ~ 640 nm. Development and characteristics of the intra-cavity frequency doubled Cr:forsterite laser at TRIUMF as part of this work is illustrated in more details in Chapter 5.

The ion guide laser ion source (IG-LIS) is a further development to produce radioactive beams of enhanced isobaric purity. This laser ion source in combination with a linear radio-frequency quadrupole delivers high purity beams. Simulation results in Chapter 6 provide valuable information about the performance of current IG-LIS in TRIUMF as well as possible advancement that can be considered for the next generation of IG-LIS, in order to obtain highly efficient isobar free radioactive ion beam [23].

The chemical properties of an element are primarily governed by the configuration of electrons in the valence shell. Precise and accurate experimental determination of ionization potential (IP) gives information on binding energy of valence electrons, and also, on the degree of relativistic stabilization. Relativistic effects influence the electronic structure of heavy elements, and these effects increase dramatically in the seventh row–including the actinides–even affecting electronic ground-state configurations. Precision spectroscopy of high-lying Rydberg and AI Rydberg levels can be used to deduce the first ionization potential of these elements with high accuracy. Chapter 7 presents the study of odd-parity Rydberg and AI Rydberg states of Tm by laser resonance ionization spectroscopy which resulted in more accurate measurement of thulium IP [24]. An efficient ionization scheme was discovered as a result of this spectroscopy and was applied successfully for

Tm radioactive ion beam delivery. Furthermore, study of even-parity AI Rydberg states of La in Chapter 8 lead to a consistent value for the IP [25] which is two orders of magnitude more precise than what has been reported previously [26]. For radioactive elements in general and astatine in particular, resonance ionization in-source spectroscopy will be deployed to search for autoionizing states and subsequently to develop ionization schemes. A detailed description of in-source laser spectroscopy of astatine to search for autoionizing states and the results of this spectroscopy are provided in Chapter 9.

Part I

Theory and Methods in Resonance Ionization Mass Spectroscopy

2 | Rydberg atoms

The objective of this chapter is to introduce the basic properties of highly excited atoms (Rydberg atoms), such as level energies and quantum defect, and the ionization potential. Using these principles, we can analyze the principal quantum number n dependency of the measured level energies to extract the ionization potential.

2.1 Features of Rydberg atoms

The Rydberg atom is the atom in which one of its electrons is in a highly excited to a state with a large principal quantum number n. As a result, the Rydberg atom has a number of peculiar physical properties [27–29] as compared to the atoms in the ground or low excited states. One specific feature of the Rydberg atom is a great number of closely spaced energy levels. The radiation lifetime of the Rydberg atom increases drastically with increasing n. It is proportional to n^3 and n^5 for the highly excited states with small ($l \ll n$) and large ($l \sim n$) values of the orbital angular momentum l, respectively. At the same time, the highly excited atom turns out to be very sensitive to the influence of various perturbations and external fields. Thus the Rydberg atom is a rather unusual object having simultaneously both pure quantal and classical properties and a number of exotic features. In general, however, the structure and basic features of any atom in highly excited state are similar to the hydrogen atom since the interaction between the Rydberg electron and the parent ionic core is primarily determined by their Coulomb interaction at large distances.

2.2 Rydberg series in atomic spectra

Rydberg atoms have been produced by charge exchange, electron impact, and photoexcitation. Thermal beams of Rydberg atoms have been made by electron impact or optical excitation of beams of ground state atoms, and many of the relevant considerations are described by Ramsey [30]. The cross section for the production of Rydberg atoms is the continuation below the limit of the ionization cross section, leading to an n^{-3} dependence of the excitation cross section.

In optical excitation the exciting photon is absorbed by the target atom. As a result, specifying the energy and angular momentum of the absorbed photon specifies the produced Rydberg state. In contrast, for electron impact process, specifying the energy of an incoming electron does not specify the energy of the produced Rydberg state because there is no way to control how the energy is shared between the incident electron and the electron which is excited to the Rydberg state.

Above the ionization limit, the photoionization cross section is given by σ_I. Below the limit, the cross section is averaged over an integral number of n states equals σ_I. The cross section $\sigma(n)$ for exciting a resolved Rydberg state is given by [28]:

$$\sigma(n) = \frac{\sigma_I}{\Delta W n^3} \tag{2.1}$$

where ΔW is the energy resolution of the excitation. The cross section for exciting the Rydberg state is the photoionization cross section times the ratio of the Δn energy interval to the experimental resolution.

In most optical excitations, the resolution is determined by the Doppler effect or the finite linewidth of the light source. The Doppler effect gives a typical frequency width of 1 GHz, and the width of light source can be anywhere from 1 kHz to 30 GHz. In this work, the atoms are generated in a hot crucible up to 2000 °C, and for the case of the first transition in ^{169}Tm (371.897 nm), the Doppler

broadening can be calculated as ~ 2 GHz. The Ti:Sa lasers that have been applied for spectroscopy in this work have a typical linewidth of 1-6 GHz, which is larger than the Doppler width.

2.3 Energy levels in H and H-like atoms

To an excellent approximation, the energy levels E_n of H and hydrogenic atoms or ions obey the formula [31]:

$$E_n = E_\infty - \frac{R_\mu Z^2}{n^2} \tag{2.2}$$

where n is the principal quantum number, E_∞ is the series limit or ionization potential, R_μ is the Rydberg constant for the species of reduced mass $\mu = m_e m_p/(m_e + m_p)$ and Z is the nuclear charge (i.e. $Z = 1$ for a neutral species).

The energy formula is obtained by solving the radial Schrödinger equation, which can be written as

$$-\frac{\hbar^2}{2m}\frac{d^2u_{nl}}{dr^2} + \left(\frac{l(l+1)\hbar^2}{2mr^2} - \frac{Ze^2}{4\pi\varepsilon_0 r}\right)u_{nl} = E_n u_{nl} \tag{2.3}$$

where the complete eigenfunction of the electron

$$\psi_{nl}(r,\theta,\phi) = R_{nl}(r)Y_{lm}(\theta,\phi) \tag{2.4}$$

is separable in radial and angular coordinates and $u_{nl}(r) \equiv rR_{nl}(r)$ [31].

For alkaline or hydrogen-like atoms, the reduced mass (or mass correction) of R_μ can be calculated as

$$R_\mu = R_\infty/(1 + \frac{m_e}{M}) \tag{2.5}$$

where M is the mass of the hydrogen-like atom and $R_\infty = 109737.31568\,\mathrm{cm}^{-1}$ [32] is the Rydberg constant obtained from

$$R_\infty = \frac{me^4}{8\varepsilon_0^2 h^3 c}. \tag{2.6}$$

The Rydberg series of energy levels E_n obeys the formula [33–35]:

$$E_{nl} = E_\infty - \frac{R_\mu Z^2}{(n-\delta_l)^2} = E_\infty - \frac{R_\mu Z^2}{n^{*2}}, \tag{2.7}$$

Where δ_l is an approximate constant, known as quantum defect (more details can be found in Section 2.5), for a given series of angular momentum l and $n^* = n - \delta_l$. Non-hydrogenic cores may have such a large effect on the lowest members that they may not seem to belong to the same Rydberg series (quantum defect will not be constant and might change for lower numbers of n).

2.4 Ionization potential determination

The value for the IP in this work is extracted from the individual positions E_n of the resonances on one Rydberg series with high precision using the Rydberg-Ritz formula [33, 36]:

$$E_{n,l} = E_{IP} - \frac{R_\mu}{(n-\delta_{n,l})^2}. \tag{2.8}$$

This formula describes the level energies with principal quantum numbers n, converging to the limit of the series E_{IP} for $n \to \infty$. $\delta_{n,l}$ is the n-dependent quantum defect, which can be described by the Ritz expansion [28]:

$$\delta_{n,l} = \delta_0 + \frac{\delta_1}{(n-\delta_0)^2}. \tag{2.9}$$

In this expansion δ_0 is an n-independent constant part of the quantum defect and δ_1 is the slope of the form factor which depends on the configuration of the series. In this work, for high-lying Rydberg members, further expansions and possible Stark shifts can be neglected owing to the large spectral linewidth of the lasers and only small electric fields.

2.5 Quantum defect and series perturbation

A simple way to introduce the quantum defect is to suppose that the potential of the atom is nearly Coulombic, but differs at short range by an α/r^2-dependent term. Thus, the effective potential can be written as [35]:

$$V_{eff}(r) = -\frac{Ze^2}{4\pi\varepsilon_0 r} + \frac{\hbar^2}{2m}\frac{\alpha}{r^2} \tag{2.10}$$

where α is merely an adjustable parameter and the factor $\hbar^2/2m$ is introduced for convenience. Hence Equation (2.3) is replaced by

$$-\frac{\hbar^2}{2m}\frac{d^2u_{nl'}}{dr^2} + \left(\frac{l'(l'+1)\hbar^2}{2mr^2} - \frac{Ze^2}{4\pi\varepsilon_0 r}\right)u_{nl'} = E_n u_{nl'} \tag{2.11}$$

where $l'(l'+1) = l(l+1) + \alpha$. If we let $l' = l - \delta_l$, then

$$\delta_l = l + \frac{1}{2} \pm \left((l+\frac{1}{2})^2 + \alpha\right)^{\frac{1}{2}} \tag{2.12}$$

where the sign + is unphysical, as $lim_{\alpha \longrightarrow 0}\, \delta_l = 0$. It follows that

$$E_{nl} = -\frac{R}{n - \delta_l}. \tag{2.13}$$

This approach shows that the quantum defect results from the short range part of the potential.

Quantum defects are large for s-electrons, $l = 0$, and decrease for increasing angular momentum.

When Gentile et al. [37] measured the intervals between the low angular momentum states of Ca, they determined the quantum defects of the observed series and fit them to two forms

$$\delta(n) = \delta_0 + \frac{\delta_1}{(n-\delta_0)^2} + \frac{\delta_2}{(n-\delta_0)^4}, \tag{2.14}$$

which takes into account the slow variation of the quantum defect with energy. If there is a perturber in the bound series of alkaline earth, the energy perturbation can be represented in the quantum defect as [28]:

$$\delta(n) = \delta'_0 + \frac{\delta'_1}{(n-\delta'_0)^2} \ldots + \frac{\alpha}{(n-\delta'_0)^{-2} - 2W_p}, \tag{2.15}$$

where W_p is the energy of the perturber.

2.5.1 Role of quantum defect theory for bound states

As described in the previous sections, the quantum defect is defined from a slight modification of the Rydberg formula for hydrogen to account for the extended core of complex atoms. Quantum defect theory (QDT) was developed by Seaton and collaborators [34].

Quantum defect is found experimentally to be nearly constant for different series members, especially for unperturbed series in atoms with a compact core. The first task of QDT is to explain this fact, and to extract from this empirical observation an appropriate wavefunction, consistent with an effective one-electron Schrödinger equation, such that the quantum defect would turn out to be nearly constant as the principal quantum number n is changed.

QDT provides a framework which relates a few energy independent parameters to a wealth of spectroscopic data. It is used both as an efficient way to parametrize data and as a way of comparing theoretical results to experimental data.

QDT has nothing to say about the value of δ except that it is assumed to remain constant as n is changed for a channel free of perturbations.

2.5.2 Lu-Fano graphs

Single channel QDT introduces an unperturbed Rydberg series to a small number of constants, which include δ [35]. A constant value of δ is a rarity, since most series in the spectra of many-electron atoms are in fact perturbed.

In order to assign the observed unsorted levels from an experiment to one or other series, the procedure is to calculate quantum defects referring them to both possible limits, and choose the best fit to two series. If the series are unperturbed (i.e. constant quantum defects), the points will lie on two intersecting straight lines, and we can use such a plot to read off directly which line belong to which series. However, if a point lies far off the lines, the quantum defects can no longer remain constant because both series will be perturbed. The extent of the perturbation will depend on the energy interval between the series members. By standard second-order perturbation theory, the strength of the perturbation fall off as the inverse of the energy interval. Therefore, the branches of the graph must affect each other most at the intersection. There is a fundamental rule by von Neumann and Wigner [38] which states that two curves representing the energies of interacting states (states with the same quantum numbers J) as a function of a continuously adjustable perturbation cannot actually cross, but must exhibit an avoided crossing. For an exact or true crossing, there can be no interaction between series and they must possess different quantum numbers.

For series members close to the avoided crossing, the distance to the two branches in the graph may easily become equal, It is then impossible to distinguish the series and they are completely mixed.

Figure 2.1 as plots of δ_1 against δ_2 introduces this theory. Since theory yields a continuous function $\delta_1(n_2^*)$ ($n^* = n - \delta$ is the reduced variable energy or effective quantum number) representing a continuous variation in δ_1 as a function of the continuous energy variable δ_2, it is conventional to

plot δ_1 against n_2^* mod 1 (i.e. taking account only of the fractional part), which (neglecting a sign change) is the same diagram. Such graphs are called Lu-Fano graphs [34, 39] and are commonly used to analyze interactions between series when they are simple enough to involve only two distinct limits.

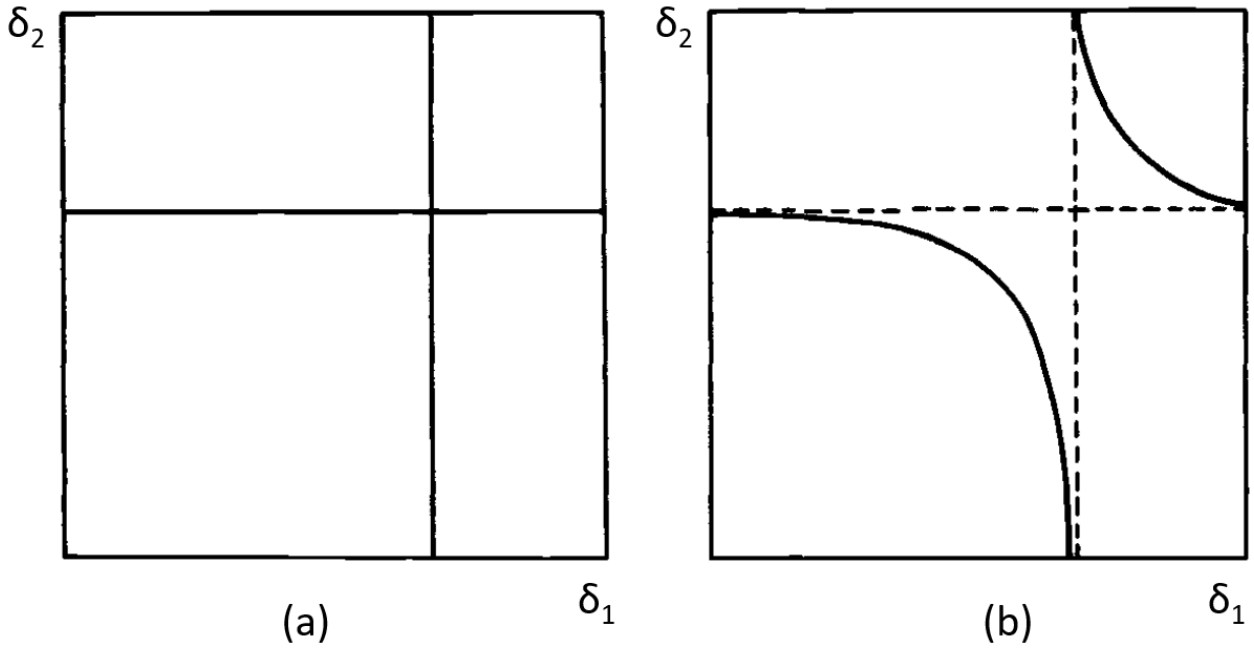

Figure 2.1: Plot of quantum defects for the bound states of two Rydberg series converging to different limits: (a) for no inter-channel coupling; (b) for non-zero inter-channel coupling. The picture is taken from [35].

2.6 Autoionization

Autoionization is an interaction between a bound state that belongs to a closed channel (energy below the ionization threshold) and a continuum state (belonging to an open channel) that is energy degenerate. Thus, the bound state is only quasi-bound because the interaction leads to its decay into the continuum state and a free electron [40]. The stronger the interaction the faster the decay and the wider, in energy space ($\Delta E \Delta t \sim \hbar$), the resonance. The wider resonances indicate that they autoionize faster. In most cases, electron wave functions have a significant overlap and thus, the energy transfer happens quite fast. As a consequence, these AI states are

usually rather short-lived with lifetimes below nanoseconds [35]. This causes a large spectral width of corresponding transitions, which can reach more than 100 GHz, exceeding the typical natural linewidths for radiative decay of ~ 10 MHz by many orders of magnitude. In addition, the observed resonance peaks in the spectrum often show a characteristic asymmetry which is caused by the interference of the excitation into the discrete AI state with the competing process of excitation into the continuum [40, 41].

As the excitation is a resonant transition into an upper state, this excitation step offers higher efficiency compared to non-resonant ionization and can exhibit saturation. In combination with the high probability of ionization, this fact results in ionization cross-sections about 10^4 times larger than those of non-resonant ionization [42]. Detailed studies of the electronic configuration of those states are difficult, as the autoionization hinders any further transition. The underlying atomic configuration with multiple excited atoms is also non-trivial and hardly predictable by theory. Hence, for most elements, detailed documentation of AI states and reliable level assignments are missing in the literature. Nevertheless, experimental observations confirm the expected high number of AI states in atoms with many open shells. Prominent examples are the lanthanides and actinides, which show exceptionally pronounced continuum structures with large numbers of AI states [43–45].

Autoionizing Rydberg states

One of the inherent properties of autoionizing Rydberg states is that both the excited autoionizing state and the degenerate continuum have non-zero excitation amplitudes from the initial state. These amplitudes can interfere constructively or destructively. Typically if the interference is constructive on the high energy side of the autoionizing state it is destructive on the low energy side and vice versa. The interference term between the two excitation amplitudes changes sign across the autoionizing resonance due to the continuum phase shift of π on going through the resonance. The resulting asymmetric line profiles are termed Beutler-Fano profiles [41]. While the line profiles of

autoionizing states are not symmetric, it is still possible to extract the energies and widths of the autoionizing states from the spectra.

Sometimes the spectrum is irregular due to the inter-series interaction. Such spectra, are particularly difficult to analyze because both the bound-continuum excitation interference and the inter-series interactions lead to peculiar lineshapes, and it is difficult to disentangle the two effects present in the spectra.

3 | Resonant laser ionization

The theoretical background of the interaction between light and the atomic system is well established. This chapter will provide only the basic information necessary to understand the experimental studies highlighted in this work. Further information may be found in various text books, for example in [46, 47].

3.1 Multi-electron systems and electronic configurations

In the ground state of a multi-electron atom, the electrons occupy the available orbitals according to the Pauli exclusion principle and Hund's rule. Independent of the atomic state, the Hamiltonian can be separated into an unperturbed part containing the experience of a mean field potential H_{mean}, the second part which contains the rest of the term of the full Hamiltonian H_{rest}, and the spin-orbit interaction H_{s-o} which results from the spin-orbit interaction of the individual electrons and describes angular momentum coupling [48]:

$$H_{tot} = H_{mean} + H_{rest} + H_{s-o}. \tag{3.1}$$

The state of each electron can be described with quantum numbers n, l, m_l, m_s. The coupling of the orbital and spin angular momenta is determined by the relative strength of the individual contributions. However, most atoms show a mixture of coupling mechanisms, or different couplings for sub-groups of electrons. The two limiting cases for coupling arise from the different length

scales of distances between preferred regions of the electrons around the nucleus in differently sized atoms. This goes along with the relative size of the two perturbative terms.

LS-coupling: The spin-orbit coupling is weak in relation to global coupling if the distances are small, yielding LS-coupling and coming along with $H_{rest} \gg H_{s-o}$. The individual moments couple to the total moments

$$L = \sum_{i=1} l_i \quad \text{and} \quad S = \sum_{i=1} s_i. \tag{3.2}$$

The total angular momentum is

$$\overrightarrow{J} = \overrightarrow{L} + \overrightarrow{S} \quad \text{with} \quad | L - S | < J < | L + S | . \tag{3.3}$$

This is called *LS* coupling or Russel-Saunders coupling and is the dominant coupling mechanism in light atoms, with $Z < 30$ [49]. Energy levels are described by the total quantum numbers L, S, J and are denoted using the term symbol

$$^{2S+1}L_J^{(o)}, \tag{3.4}$$

where the o indicates an odd parity of the atomic state. $L = 0, 1, 2, ...$ is denoted by the letters $S, P, D, ...$ The term $2S + 1$ is referred to as spin multiplicity. As the fine structure splitting is small compared to the separation of states with different L or S, the individual fine structure components lie closely together within the energy spectrum. These groups of fine structure components belonging to a specific L and S are called fine structure multiplets or, correspondingly to their number of components, singlets, doublet, triplets and so on.

jj-coupling: In the case of a heavy system ($Z > 60$) the distances are large; so the effect of the spin-orbit coupling is no longer negligible in relation to electrostatic effects ($H_{s-o} \gg H_{rest}$). This

fact leads to the behavior of the atoms that their electrons first couple their l_i and s_i to single electron total angular momenta j_i and those add up to a whole system total angular momentum J:

$$j_i = l_i + s_i \quad \text{and} \quad J = \sum_{i=1}^{N} j_i. \tag{3.5}$$

The total orbital angular momentum L and the total spin S are not defined. These atoms tend to exhibit quite complex spectra, because the strong individual spin-orbit coupling causes the energy levels for a specific l_i to distribute across a larger energy region. As a result, the typical formation of a multiplet structure, like in the LS-coupling, is missing.

3.2 Selection rules

Selection rules may be rigorous (strong) or approximate (weak), depending on whether the quantum numbers involved are well-characterized constants of the motion for the complete many-electron system or whether they are only approximate constants, or describe only one electron or a subgroup of electrons. Thus, for electric dipole transitions, in the absence of external fields, the parity selection rule, which allows only transitions from even to odd or odd to even states to occur is a strong rule. Likewise, if ΔJ is the difference in total angular momentum quantum number between the initial and final states, then $\Delta J = 0, \pm 1$ and $J = 0 \nrightarrow J = 0$ is also a strong rule. On the other hand, the rules $\Delta L = \pm 1$ and $\Delta S = 0$ are valid only for LS-coupling, and will give way to different rules (or, perhaps, no strict rules) when the coupling conditions change. These are called weak selection rules.

Although the parity rule is a strong one, the individual l_i angular momentum of electron i is not an exact quantum number for a many-electron system. Thus, while the parity, which is defined as $(-1)^{\sum_i l_i}$ remains a good quantum number, the individual values of l_i which are involved in defining it are not unique. This is how configurations involving more than one excited electron can be accessed by photo-excitation.

For the conservation of angular momentum, since the angular momentum of the photon is $\pm\hbar$, the angular momentum of the atom must also change by $\pm\hbar$ upon absorption or emission of one photon, which may be coupled to the change ΔL in the angular momentum of an individual electron via the independent particle approximation.

3.3 Photo-ionization process

The principle of resonant excitation and ionization is visualized in Figure 3.1. Valence electrons are excited from the ground state to higher excited levels. Thereby, the energy difference between two atomic levels is bridged by photons which fulfill the resonance condition.

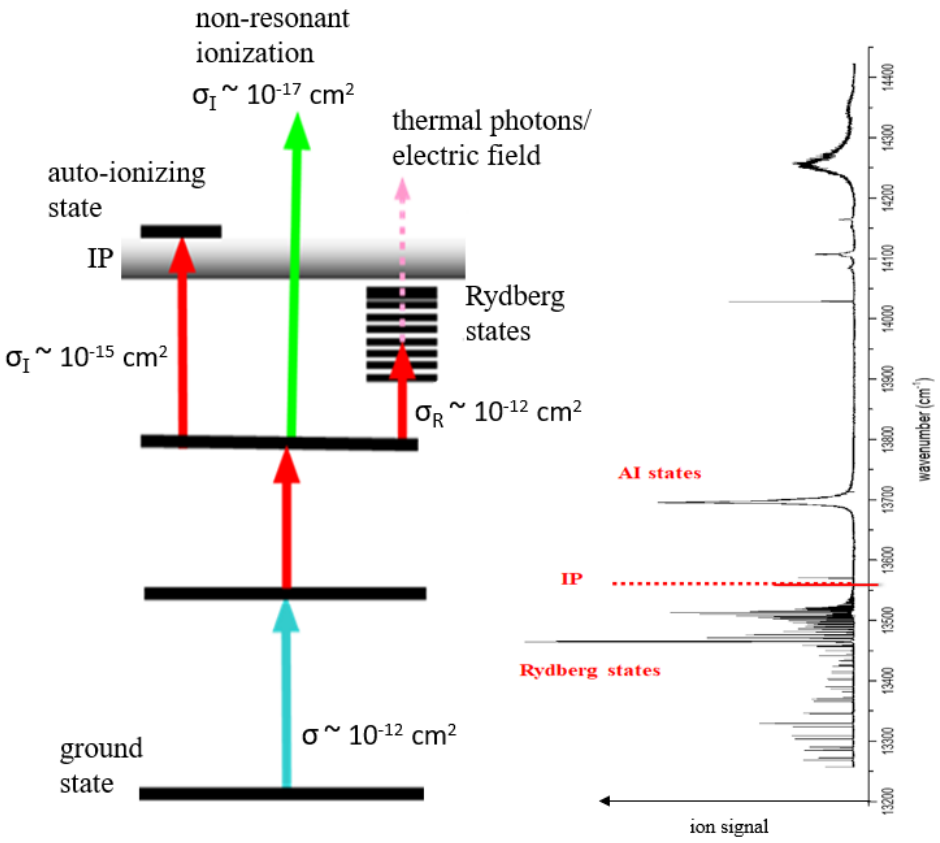

Figure 3.1: Working principle of resonant laser excitation and possible ionization scheme. In resonance ionization photon beams from a tunable laser are used to selectively excite and promote electrons from ground state to higher excited states. The spectrum shows a sample ionization spectrum of antimony measured at TRIUMF [50].

As the absolute energy levels and the corresponding energy differences are characteristic fingerprints of the individual elements, only the selected element can be excited by proper wavelength adjustment of tunable lasers. Typical excitation cross sections for these resonant transitions are on the order of $10^{-10}\,\mathrm{cm}^2$. After single or step-wise resonant excitation, three different ionization processes are possible, which all find their application in laser resonance ionization of different elements. The simplest approach, lacking any selectivity in the ionization step, involves a non-resonant excitation of the valence electron above the ionization potential into the continuum. In this case, the cross section for this non-resonant process is on the order of only $10^{-17}\,\mathrm{cm}^2$ [18, 46]. This can be somewhat compensated by using a high power ionizing fixed-frequency laser. In contrast to non-resonant ionization, significantly lower laser powers are sufficient for resonant excitation of the valence electron into well localized states situated above the IP. Such so-called autoionizing resonances exist for many elements with complex atomic structure. Similar to the lower level excitation steps between bound energy levels, this ionization process also contributes to elemental selectivity, while typical cross sections are in the range of 10^{-12}–$10^{-15}\,\mathrm{cm}^2$ [42]. In the presence of high electric fields/thermal photons, a third ionization process can be applied for LIS. By resonant laser radiation a valence electron is excited into a high-lying bound Rydberg state, located slightly below the IP from where the atom can then be ionized in the electric field/thermal photons of an extraction electrode. Cross sections as for auto-ionization can be achieved by field ionization of Rydberg states.

Resonance ionization mass spectrometry combines the resonant ionization process with a subsequent mass selection process. This can be achieved by using a magnetic mass separator or a quadrupole mass filter or time of flight mass spectrometer. As illustrated in Figure 3.2, the combination of the mass resolution with the element selectivity of the resonance ionization provides access to an isobaric pure ion beam.

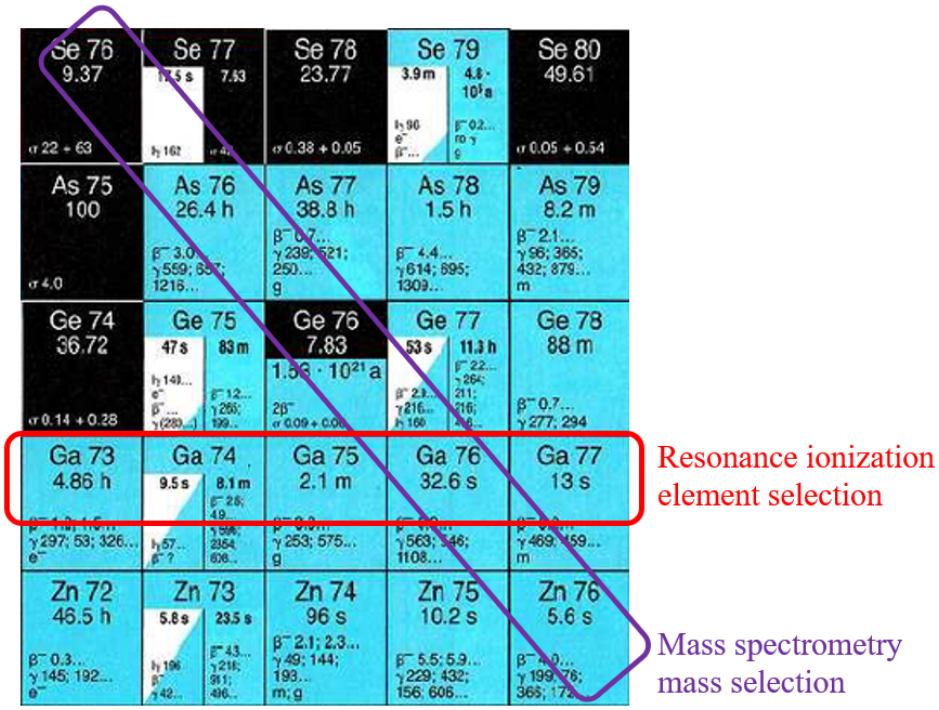

Figure 3.2: Isotope selection by combining element selective resonance ionization and mass separation. Reproduced from [51].

3.4 Ionization scheme development

Ionization scheme development at the RILIS has become a well established procedure comprising of a few key steps:

Literature search: After studying the various sources of atomic spectral line data, theoretical ionization schemes can be constructed. Some predictions about the relative efficiencies of the proposed schemes can be made if the data includes measurements of the line strengths or excited state lifetimes. Web based atomic spectral line databases [26] and a series of resonance ionization spectroscopy data compilations by E.B. Saloman [52–56] have been particularly useful for this data collection procedure.

Resonance ionization spectroscopy of stable isotope: a small sample of the stable isotope is placed in an oven. Heating the oven releases the sample as an atomic vapor that effuses into the ionizer cavity. This work will be described in later Chapter 7 and Chapter 8, where two step resonance

ionization schemes are investigated. Resonance ionization spectroscopy (RIS) involves scanning the last excitation frequency across the range of possible transitions whilst the frequency of the first transition steps is kept fixed. The ion current is monitored for example on a channeltron electron multiplier (CEM) detector.

Saturation measurement: For selected transitions, the dependence of the ion current versus the power of the laser beam was measured. The experimentally measured saturation power gives an indication of minimal required power for RILIS operation without a loss of efficiency.

In many cases non-resonant ionization is combined with a single resonant excitation step. This scheme is the simplest ionization process, especially for elements of which high-lying Rydberg states or AI resonances are not known from literature or preparatory studies.

3.5 Spectral line broadening

Several effects influence the spectral line shape of an optical transition. The contribution of all effects add up to the experimental line shape which is observed in the recorded data. Throughout the present work, the word linewidth is always used in terms of the full width at half maximum ($FWHM$) of a peak.

3.5.1 Natural linewidth

Natural broadening is directly related to the uncertainty principle of Heisenberg.

$$\Delta E \Delta t \sim \frac{h}{2\pi}. \tag{3.6}$$

This type of spectral line broadening arises from the spontaneous decay rate γ. A photon in a certain energy state will therefore have a range of possible frequencies when it decays to a lower state:

$$\Delta\nu \sim \frac{\Delta E}{h} \sim \frac{1}{2\pi\Delta t}. \tag{3.7}$$

The line profile function ϕ_ν resulting from natural broadening is the Lorentzian profile and is proportional to γ:

$$\phi_\nu = \frac{\gamma}{4\pi^2}\frac{1}{(\nu-\nu_0)^2 + (\frac{\gamma}{4\pi})^2}. \tag{3.8}$$

The peak value of the profile occurs when $\nu = \nu_0$. This can be used to calculate the $FWHM$ by setting $\frac{\phi_{peak}}{2} = \phi(\nu)$ and solving for $2 \times (\nu - \nu_0)$. The result is

$$\Delta\nu_{FWHM} = \frac{\gamma}{2\pi}. \tag{3.9}$$

Stimulated emission effects must be added to the spontaneous emission ones for a radiation. Overall, natural line broadening is not often directly observed, except in the line wings in low-pressure environments [40, 46]. Other broadening mechanisms usually dominate.

3.5.2 Thermal Doppler broadening

Doppler-shifted frequency ν for an atom moving at velocity v_x along the line of sight differs from υ_0 in rest frame of atom. Combining Doppler shift with the one-dimensional distribution of velocities, which results from Maxwell-Boltzmann statistics, follows a Gaussian velocity distribution and leads to

$$\phi_\nu = \frac{2\sqrt{ln2}}{\sqrt{\pi}\Delta\nu_D} exp\left\{-\left(\frac{2\sqrt{ln2}}{\Delta\nu_D}(\nu-\nu_0)\right)^2\right\} \tag{3.10}$$

where Doppler width $\Delta\nu_D$ is defined as

$$\Delta\nu_D(FWHM) = \frac{2\nu_0}{c}\sqrt{\frac{2ln2\,k_BT}{m}}. \tag{3.11}$$

Where ν_0 is the mean optical frequency and m is the mass of the atoms. The lasers applied at TRILIS have a linewidth of 1 GHz to 3 GHz in order to ionize the atoms in most velocity classes.

3.5.3 Saturation broadening

Assuming an atom with two states $\mid 1\rangle$ and $\mid 2\rangle$ with resonance frequency $\nu_0 = (E_2 - E_1)/\hbar$ and a laser frequency ν_L with detuning $\delta = \nu_L - \nu_0$, the excited state population $\phi(\nu)$ in steady state condition is given as [57–59]:

$$\phi(\nu) = \frac{S_0/2}{1 + S_0 + 4\delta^2/\gamma^2} = \frac{S_0}{2(S_0+1)}.\frac{1}{1 + 4\delta^2/\gamma_s^2}. \tag{3.12}$$

Here γ is the spontaneous decay rate of state $\mid 2\rangle$ and $S_0 = I/I_{sat}$ is the resonant saturation parameter. I_{sat} is the saturation intensity

$$I_{sat} = \frac{\pi hc}{3\lambda^3\tau}, \tag{3.13}$$

where λ is the laser wavelength and τ the excited state lifetime. The profile of $\phi(\nu)$ is a Lorentzian function with full-width half-maximum (FWHM) of

$$\gamma_s = \gamma\sqrt{1 + S_0}, \tag{3.14}$$

which depends on the intensity of the laser. This effect is known as saturation broadening.

The saturation can be also observed in the correlation between the used laser intensity I and the resulting ionization rate r or extracted ion current. When applying a step-wise resonance ionization excitation, the correlation for any excitation step can be described as:

$$r(I) = r_{res}\frac{I/I_{sat}}{1 + I/I_{sat}} + \alpha I + r_0. \tag{3.15}$$

In this context, the saturation intensity I_{sat} represents the intensity which is needed to obtain half of the maximum ionization rate r_{res}. The linear term αI reflects a contribution from non-resonant ionization. This term vanishes, if the photon energy E_ν is smaller than the difference between the IP and any populated atomic state. There might be a constant background of r_0, caused by non-resonant ionization due to laser radiation of previous steps in the excitation ladder or surface ionization in the ion source.

The atomic response to a laser of fixed intensity is greater on resonance than off, but the response on resonance cannot grow as quickly with increased laser power as the response off resonance, because the on-resonance response is already more deeply saturated. This is illustrated graphically in Figure 3.3.

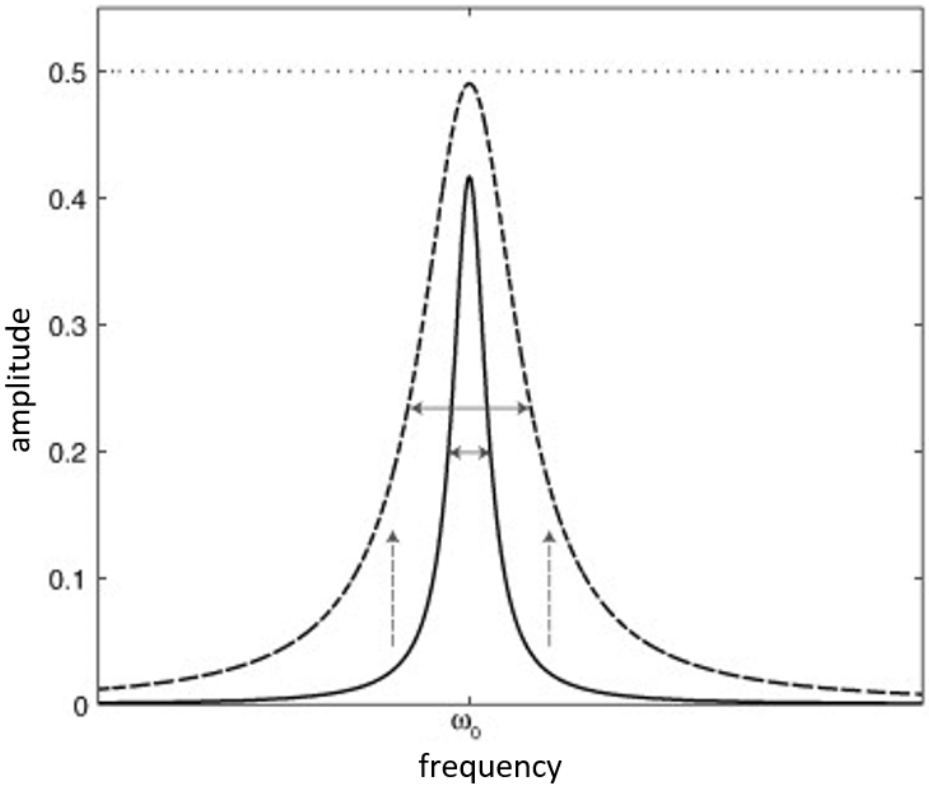

Figure 3.3: An atomic resonance excited by comparatively weak (solid curve) and strong (dashed curve) lasers. In this schematic illustration, the strong laser is ten times more intense than the weak one. On the wings of the resonance, the stronger laser excites nearly ten times as many of the atoms into the higher energy state as does the weaker laser (vertical arrows). However, on resonance, the stronger excitation is only about 20% greater than the weaker, because the excitation (i.e., the fraction of atoms in the excited state) approaches its saturation value of 0.5 (dotted line). The full width at half maximum in both cases is shown with horizontal arrows. Because the atomic excitation increases with laser power faster off resonance than it does on resonance, the resonance width necessarily increases with laser power. This is power broadening.

Part II

Solid state laser based resonance ionization laser ion source

4 | Ti:Sa laser systems at TRILIS

An overview of TRILIS and laser systems at TRIUMF can be found in A. Teigelhöfer's dissertation [60]. Due to a number of improvements to the system an update on its elements and specifications will be given here.

The main elements of TRILIS are tunable Ti:Sa lasers, pumped by high power frequency-doubled of Nd:YAG lasers (532 nm). In the following sections, specifications and operation of the laser systems are described in detail. A general change to the original design is the introduction of tunable external-cavity second harmonic generation as well as frequency mixing for third harmonic generation for automated scans in the blue (350-460 nm) and UV (250-310 nm) wavelength regions, respectively. Further additions such as self seeded grating-based Ti:Sa laser as well as a commercial BeamLock [1] system for beam pointing stabilization, during extended wavelength scans over blue and UV regions are discussed in this chapter.

4.1 Pump lasers

The pump laser Nd:YAG [2] as the main system for on-line beam delivery provides 50 W output power of second harmonic at 532 nm in *p*-polarization (light has an electric field polarized parallel to the plane of incidence) with a pulse repetition rate of 10 kHz. Its output power is divided using a combination of half-wave plates and polarizing beam-splitter cubes and directed to up to four

[1] BeamLock Aligna 4D, TEM Messtechnik GmbH, 30559 Hannover, Germany
[2] LEE laser, LDP-100 MQG, Orlando Florida (acquired by Coherent Laser Group 2018) products discontinued

Ti:Sa systems, yielding about $10 - 15$ W pumping power for each Ti:Sa after transport losses. By adjusting the delay between individual pump lasers using an external trigger, laser systems can be synchronized. Ti:Sa lasers pumped from a single pump laser are synchronized by adjusting the position of the Ti:Sa crystal within the resonator and the overall supplied pump power. At this repetition rate and power level the typical pulse length of the Nd:YAG is about 120 ns long and Ti:Sa lasers have a pulse width of 50 ns. The pump laser is running multimode and has a specified M^2 (laser beam quality which represents the degree of variation of a beam from an ideal Gaussian beam) value of about $10 - 20$. For non-resonant ionization a fixed frequency Nd:YVO_4 laser (YHP-40) provides a temporal pulse width of about 35 ns and an output power of 12 W for fundamental wavelength at 1064 nm or 6 W for the second harmonic at 532 nm and a $M^2 = 1.1$ at 10 kHz.

4.2 Characteristics of the Ti:Sa crystal as a laser gain medium

The active ion, Ti^{3+}, in the titanium-doped sapphire (Ti^{3+}:Al_2O_3) laser medium is embedded in a sapphire host in which it substitutes the Al^{3+} ion in $\approx 0.25\%$ of the lattice sites of the Al_2O_3 crystal [61].

Absorption and fluorescence spectroscopy of the Ti:Sa medium is shown in Figure 4.1. The absorption band in the blue-green range of the visible spectrum allows pumping with the 532 nm output of a frequency doubled solid-state Nd:YAG laser. The broad gain bandwidth of about 300 nm allows the construction of a widely tunable laser.

4.3 Frequency selection

In order to select and control a specific laser frequency from the broad gain bandwidth of the Ti:sapphire laser medium, frequency selective elements are integrated in the laser resonator.The most important frequency selective elements in TRILIS are described here.

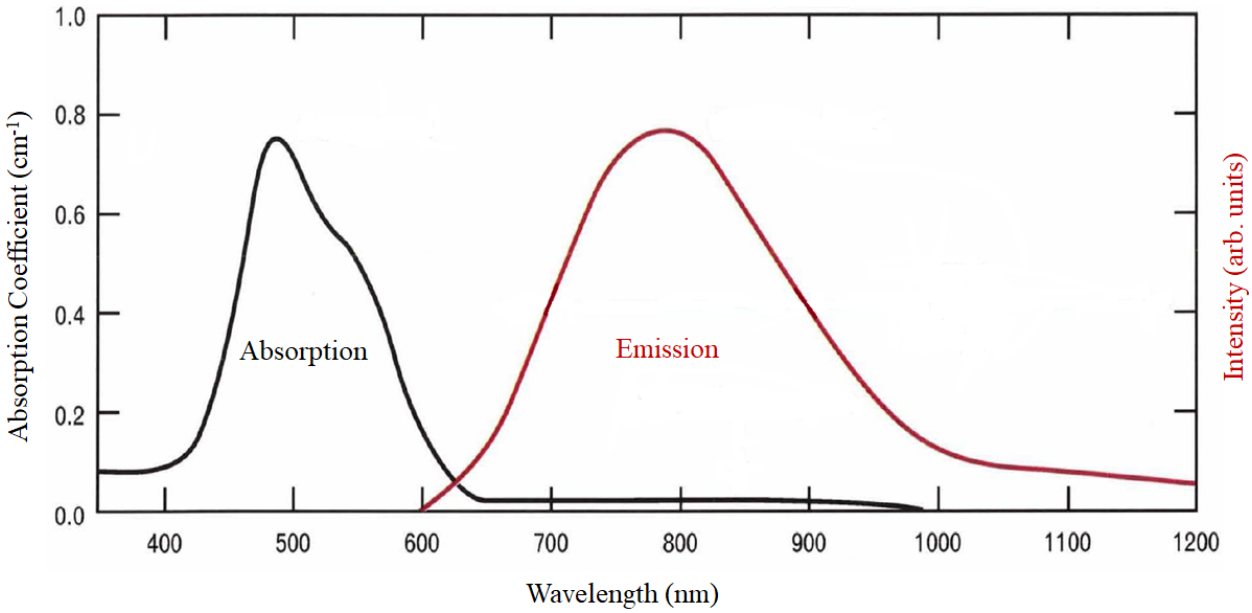

Figure 4.1: Absorption and fluorescence spectrum of Ti:Sa lasers pumped. Figure is reproduced from [62].

4.3.1 Birefringent filter-tuned (BRF) Ti:Sa laser

The resonator design of TRILIS Ti:Sa lasers, is based on a standing wave, Z-shaped cavity design [63, 64] which is optimized for operating conditions at on-line ISOL type, radioactive ion beam facilities (pulsed operation to make use of the high pulse peak power, and high repetition rate to avoid duty cycle loss). A schematic with resonator specifications is shown in Figure 4.2.

The cavity is formed using a plane high reflector (HR), an output coupler (OC) with 70 – 80 % reflectivity depending on the desired wavelength, and two curved mirrors M1 and M2 oriented at 36.2° with dichroic coatings of high reflection for the laser wavelength and an anti-reflection coating for the pump wavelength [65]. The pump lens focuses the beam on the back surface of the Ti:Sa crystal by a plano-convex lens inside a Z-shaped standing-wave cavity. To minimize losses in the p-polarized plane the two end crystal surfaces are cut and polished under Brewster's angle. The curved mirrors create a focus of the laser mode inside the central arm, at the location of the crystal and their orientation angle compensates for the astigmatism introduced by Brewster angle cut Ti:Sa crystal. This ensures the best spatial overlap with region of high population inversion in

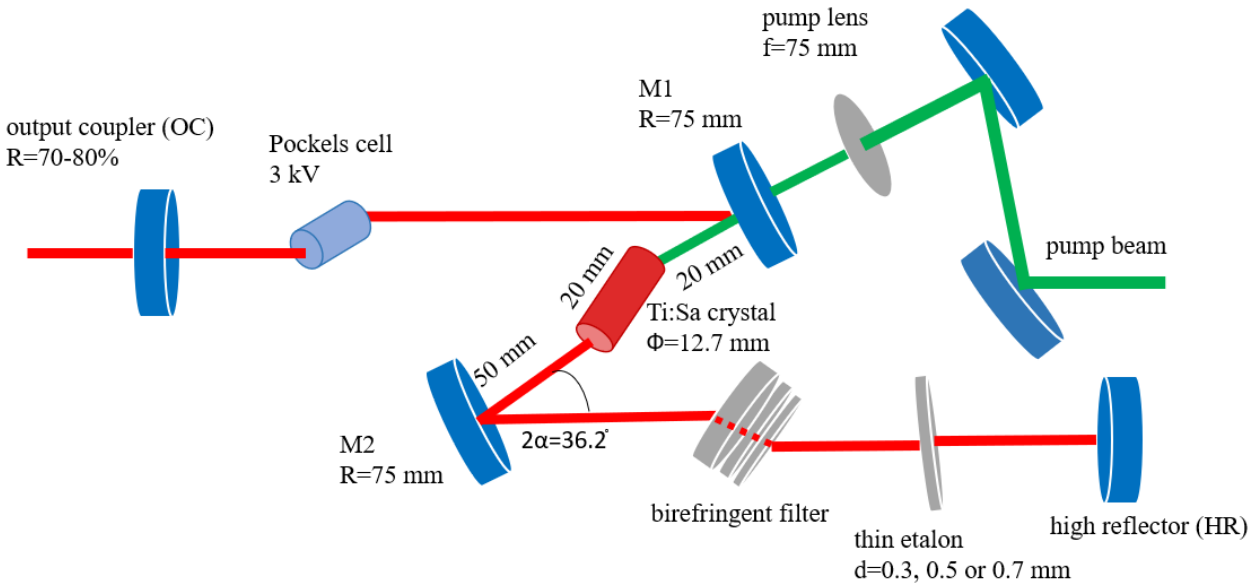

Figure 4.2: Schematic drawing of a standard birefringent filter-tuned Ti:Sa laser resonator with specifications.

the crystal, which is created by the pump beam. On the outer arms of the resonator, towards the HR mirror and the OC, the mode is almost collimated, ensuring a minimized divergence of the output beam. The focus is set to the far crystal surface to better match the pump mode with the resonator mode and also the laser can be pumped harder without damaging the crystal.

High laser intensities are required to saturate weak excitation steps and for efficient frequency conversion in nonlinear crystals needed to reach wavelengths in the blue and UV frequency region. The typical average power the TRILIS Ti:Sa lasers provide at 10 W pump power is between 1 W to 3 W at a pulse length of about 40 ns [66].

The accessible tuning range of this laser is 680 – 1000 nm with the peak output power at 780 nm. In order to reach the wavelength regions where the Ti:Sa crystal gain is low, cavity mirrors with different dielectric coatings are chosen. The BRF used in TRILIS lasers consist of four quartz plates, features a free spectral range (FSR) of 100 THz, and narrows the laser output frequency down to about 100 GHz [22]. The etalons used are 0.3, 0.5 or 0.7 mm thick plane-parallel fused silica substrates, coated with a reflectivity of 40% or uncoated. Fine wavelength selection is performed using a combination of BRF and thin etalon.

Birefringent filter

The BRF used in TRILIS is constructed from four birefringent crystals with different thickness ratios of 1:3:6:12 and 1:3:6:15 and a base thickness of 0.5 mm which uses the polarization-dependent phase shift in this material. Inside the birefringent crystal, an incident linear polarized beam of light with wavelength λ is split up into an ordinary and extraordinary beam. The polarization of both beams is perpendicular to each other. Due to the different refractive indices n_o and n_e of the axes of the crystal with thickness L, the transmitted beams feature a relative phase shift of $\delta = (2\pi/\lambda)(n_e - n_o)L$ which result in elliptical polarization of the final beam. This causes reflection and therefore losses for the s-polarized fraction at Brewster surfaces inside the resonator. For a phase of $\delta = 2m\pi$ the polarization is unchanged and no losses occur. Considering only the component of the transmitted beam which is polarized parallel to the initial p-polarized beam, the transmission function is given by [46]:

$$I(\lambda) = I_0 \, cos^2 \left(\pi \frac{(n_o - n_e)L}{\lambda} \right). \tag{4.1}$$

The free spectral range is given by

$$\Delta\nu_{FSR} = \frac{c}{\Delta nL}. \tag{4.2}$$

The free spectral range (FSR) is defined by the thinnest plate, and the linewidth by the thickness D of the thickest plate:

$$\delta\nu = \frac{c}{2^{N-1}} \Delta nD, \tag{4.3}$$

where N is the number of combining birefringent plates [67].

In order to increase the spectral selectivity, a BRF often consists of a set of birefringent plates with integer thickness ratio, like 1:3:6:12. The transmission maximum of the filter can be continuously tuned by rotating the crystal in such a way that the angle between the optical axis of the crystal and the propagation axis of the beam is changed, thus altering the extraordinary refractive index n_e. The thickest plate is crucial for the laser linewidth. In order to prevent the laser from running on two wavelengths simultaneously, a proper thickness combination must be chosen. Figure 4.3 represents the transmission curves of the TRILIS four plates birefringent filter with a thickness ratio of 1:3:6:12.

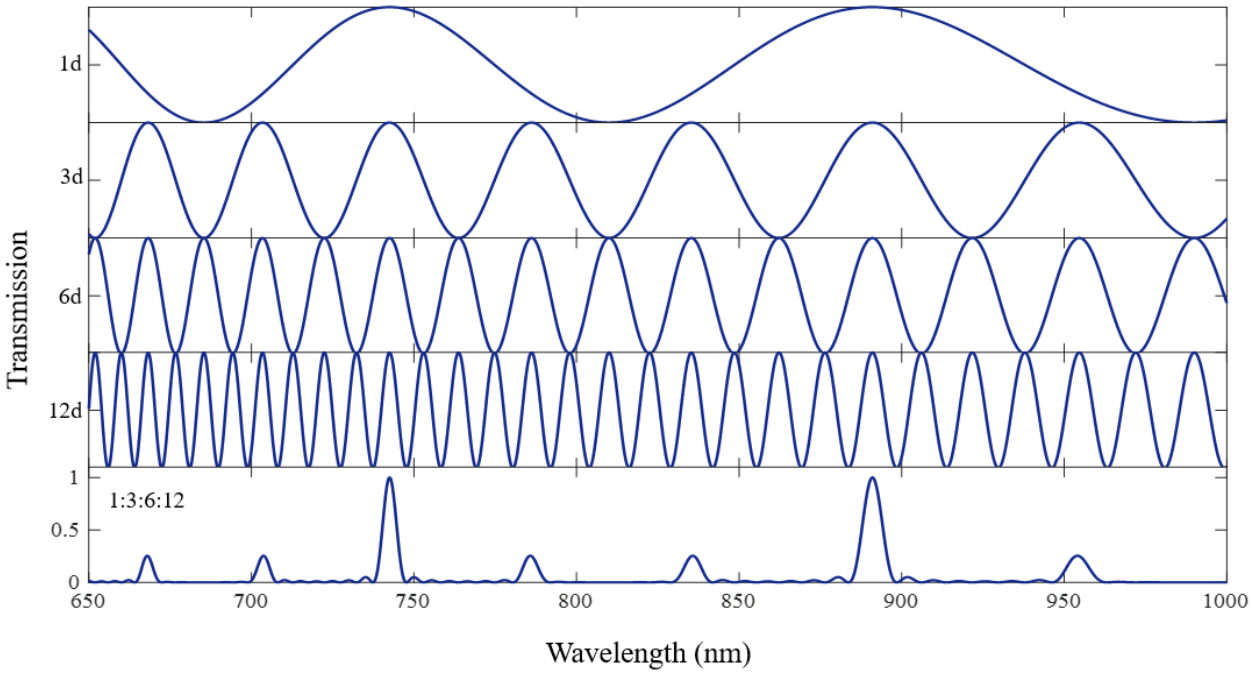

Figure 4.3: Transmission curves of the TRILIS four plate birefringent filter. The plates have a thickness ratio of 1:3:6:12. The free spectral range is defined by the thinnest plate, and the linewidth by the thickest. Other BRF 1:3:6:15 is available as well as the coherent 899-21 Ti:Sa laser BRF with 1:4:16.

Fabry-Perot etalon

The thin etalons used in this work are made from fused silica substrates, with a broad-band reflective coating of $R = 40\%$ for 680-1100 nm on both sides. The transmission formalism is the same as that of a laser resonator with the only difference that d has to be replaced with the optical path length

nd, where n is the refractive index of the etalon material [68]. The propagating beam is split up by multiple reflections inside the etalon, featuring a phase shift. The tuning of the etalon is performed by changing the angle θ with respect to the beam propagation direction which changes the optical path length inside the etalon. The free spectral range is given by $\Delta\nu_{FSR} = c/2nd$. Thus, the finesse F which is the ratio between the $\Delta\nu_{FSR}$ and the width of the transmission peaks is

$$F = \frac{\Delta\nu_{FSR}}{\delta\nu} = \frac{\pi\sqrt{R}}{1-R}. \tag{4.4}$$

For an etalon with d = 0.5 mm and a reflectivity of 40% one obtains $\Delta\nu_{FSR}$ = 200 GHz and $\delta\nu$ = 60 GHz. If one assumes 10 round trips in the cavity and the suppression of further modes below the lasing threshold of 0.6 due to losses, a laser linewidth of ≈ 10 GHz (at 800 nm) can be obtained (Figure 4.4).

4.3.2 Grating-tuned laser

For many elements there is a lack of tabulated spectroscopic data in the region of higher excited atomic states. Using a grating for wavelength selection allows for scanning over wide wavelength ranges as only the grating angle needs to be tuned, whereas in a BRF-tuned laser, both BRF and etalon need to be tuned together for extended continuous frequency scan. The development of grating-based lasers has been pursued at different facilities [69–71]. At the Oak Ridge National Laboratory a commercial system is in use [72]. The setup of the grating-based Ti:Sa laser uses a similar resonator geometry to that of the normal Z-shaped design described in Figure 4.2, while the HR is replaced by a gold coated blazed diffraction grating (26.7° [22], optimized for 500 nm, and a grating constant of 1800 grooves/mm). A photograph of grating-tuned Ti:Sa laser used in TRILIS is shown in Figure 4.5. Grating laser performance depends critically on the quality of the grating.

The grating-tuned Ti:Sa laser was deliberately designed for spectroscopy studies [69, 73]. It can provide continuous wavelength scans from 700 to 930 nm. The grating is used in the Littrow configuration [74] with the incident angle rotating from 39.0° to 58.7° corresponding to the

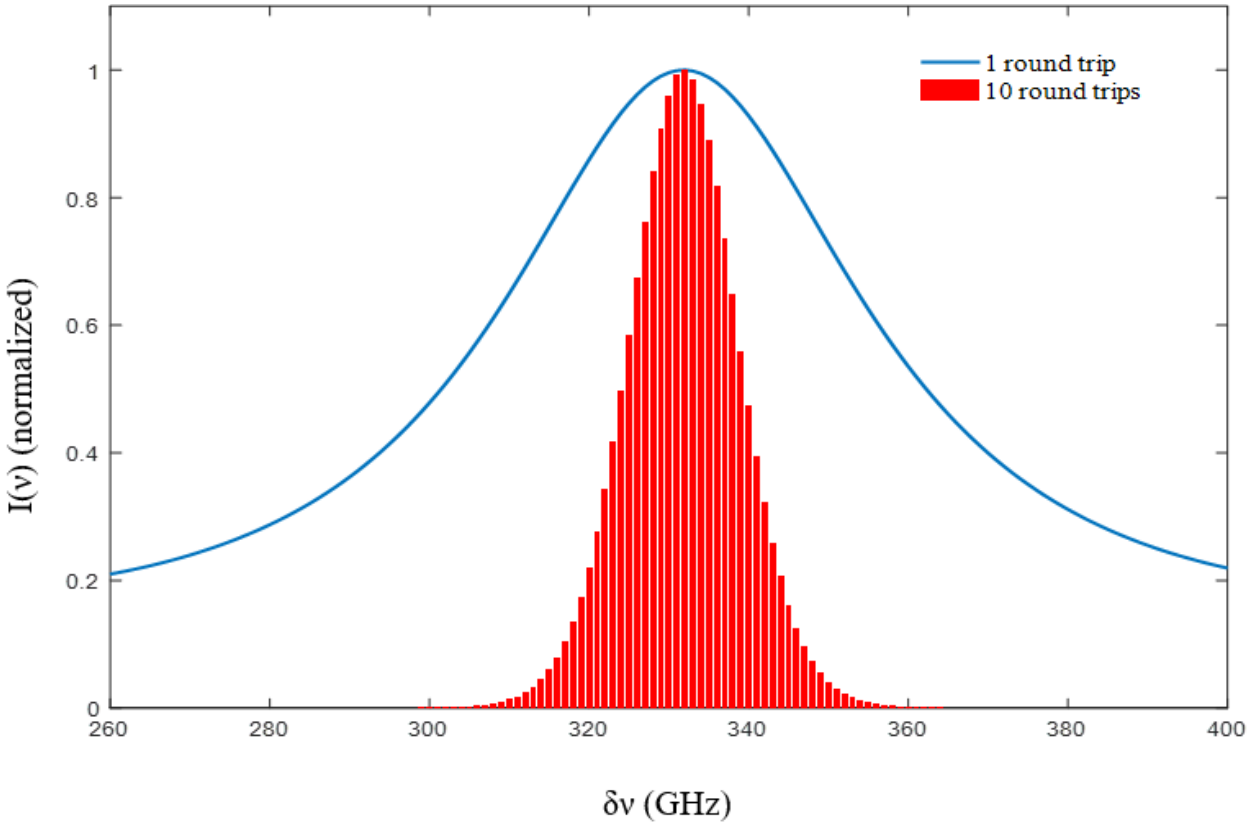

Figure 4.4: Transmission curve of the thin etalon (0.5 mm thickness) illustrated as blue curve for 1 round trip and red bars as resonator modes after 10 round trips in the resonator. A linewidth of ≈10 GHz is calculated after 10 round trips and assuming a laser threshold gain requirement of 0.6 (40% loss). The offset of each graph is ν_0 = 374.74 THz, corresponding to a wavelength of 800 nm.

wavelength range from 700 nm to 950 nm. Thus, by rotating the grating the required wavelength is directly diffracted back in to the resonator. As the frequency selection is accomplished using the grating, further frequency selective elements such as the birefringent filter or etalon are not required. This allows for a continuous frequency tuning of the laser by changing the incident angle of the grating. To achieve a desired bandwidth below ~ 10 GHz, a sufficient number of grooves on the grating have to be illuminated which is acquired by use of a prism beam expander. The high number of round-trips in the cavity narrows the linewidth and reduces it to a few GHz. The grating can be sensitive to high power densities [75]. Beam expansion is accomplished wit two anamorphic prism pairs. Prism beam expander is inserted into the cavity arm in front of the grating and expands the small mode diameter of the cavity from 10 to 17-fold depending on the prism orientation. With this beam expander, both power density on the grating as well as the laser

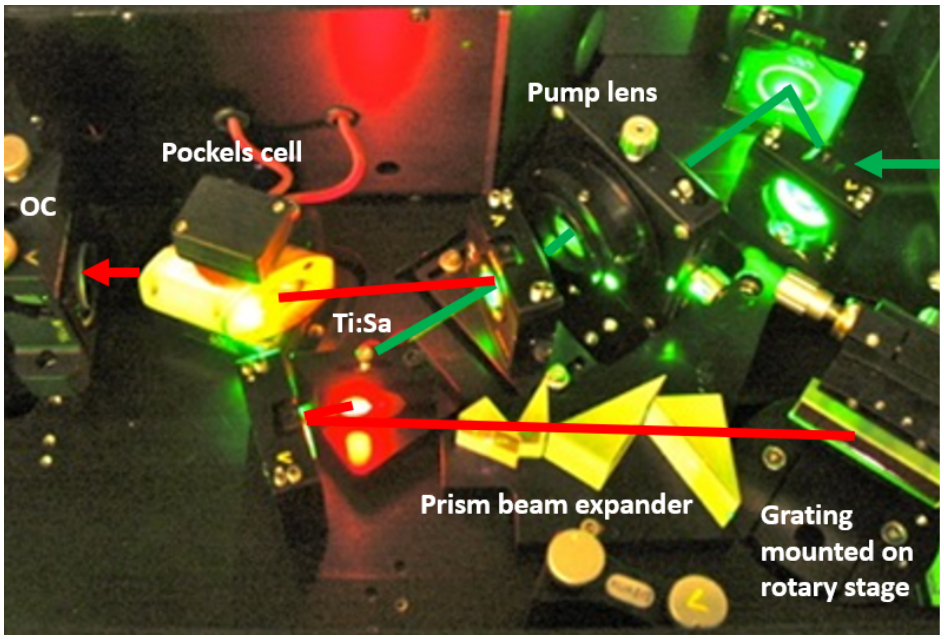

Figure 4.5: Grating-tuned Ti:Sa laser at TRIUMF. The Pockels cell in the cavity is to synchronize laser pulse timing.

linewidth are reduced. The grating itself is mounted on a computer-controlled encoded rotary stage with an angular resolution of 0.87 μrad which provides a tuning resolution of $\sim$ 300 MHz around the wavelength of 800 nm. Details of this grating laser are described in [69].

4.3.3 Self-seeded dual-cavity grating laser

A continuously tunable Ti:Sa laser self-seeded by an extended grating cavity was demonstrated and characterized in 2017 at TRILIS [73]. By inserting a partially reflecting mirror inside the cavity of a classic single-cavity grating laser, a coupled-cavity oscillator-amplifier is created. Most of the oscillating laser power confined inside the broadband power cavity which reduces the power incident onto the grating. This configuration also allows higher pump power (1.5 – 2 times increase), which is typically limited by the thermal deformation of the grating coating at high oscillation power. However, still in this configuration the grating laser pump power is limited to below 12 W. Increasing pump power beyond this will decrease the laser output power. The laser linewidth in the new configuration is 1.5 – 2 times higher, the same as or even lower than that of the classic grating laser depending on the operating wavelength and the reflectivity of the PR

mirror. The dual-cavity (D-cavity) system not only provides a continuously tunable laser source for 690 – 980 nm with the enhanced pulse peak power up to 5 kW and the linewidth of 0.3 – 8 GHz, but also an ideal source for tunable second-harmonic generation into 350 – 480 nm laser. It will be well suited to isotope separation and resonance laser ionization in-source spectroscopy. Decreasing the pump power also reduces the laser gain and leads to a further reduction of the linewidth of the laser.

Figure 4.6 presents a diagram of the D-cavity system and the graph in Figure 4.7 shows the tuning range of the Ti:Sa laser for the fundamental wavelength and the doubled frequency using a 48% partial reflector mirror in the cavity.

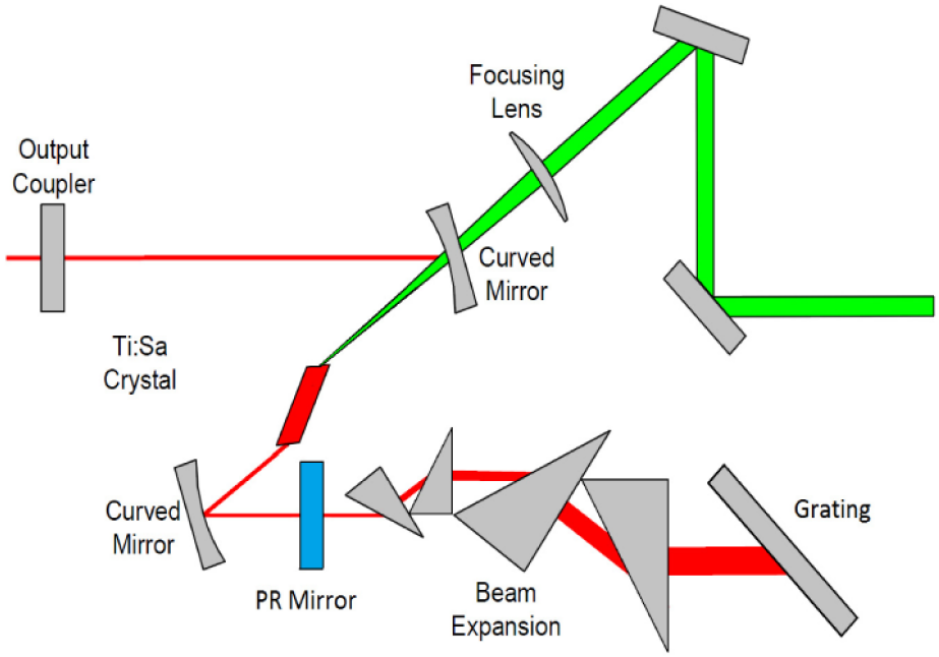

Figure 4.6: Schematic diagram of the Ti:Sa laser self-seeded by an extended grating cavity. Laser performance with different partially reflector (PR) mirror reflectivity was investigated in [73]. This configuration reduces the power incident onto the grating while allowing higher pump power which is typically limited by the thermal deformation of the grating coating.

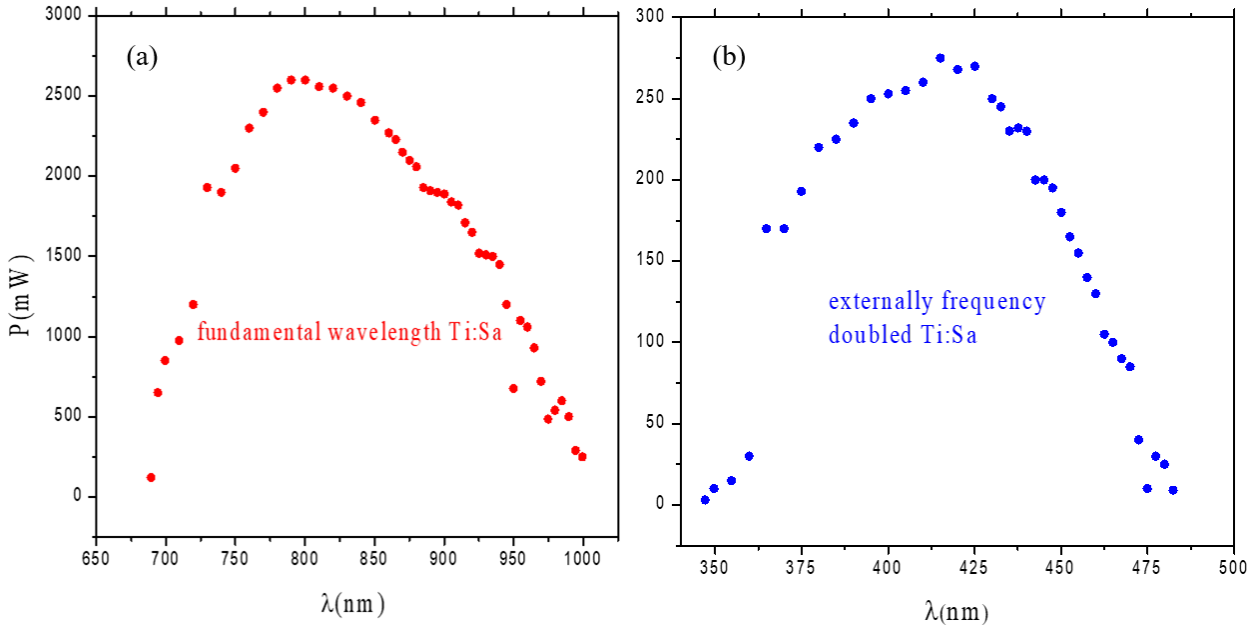

Figure 4.7: Graph of the dual-cavity Ti:Sa laser tuning range for a) fundamental and b) second harmonic wavelength. This configuration is an ideal source for extended tunable second-harmonic generation with the enhanced pulse peak power up to 5 kW.

4.4 Higher harmonic generation

Higher harmonic generation and frequency mixing in non-linear crystals is used to expand the accessible wavelength range of the laser system.This technique is described in variety of books [46,68]. This frequency conversion is realized by nonlinear polarization effects in optical nonlinear crystals. In the present work, phase matching is applied using β-barium-borate (BBO), which is known for its high damage threshold [46], bismuth-borate (BiBO) for its high conversion efficiency, and lithum-triborate (LBO) for its good beam profile due to small walk-off angle. The incident laser beam is typically focused by a f = 50 mm lens into the nonlinear crystal. The outgoing laser beam passes a cylindrical lens to optimize its beam shape. Due to the high intensities of the pulsed laser light, the process is quite efficient and reasonable powers can be obtained in second harmonic generation (SHG), third harmonic generation (THG) and forth harmonic generation (FHG). The easiest case of frequency conversion is frequency-doubling, where wavelengths between 345 – 495 nm (for the BRF laser) are reachable. By frequency-tripling, a combination of the doubled

and the fundamental light; and frequency-quadrupling, where the fundamental is doubled twice, the wavelength spectrum can be extended to 210 – 330 nm.

Another method for frequency-doubling is to place the crystal inside the laser cavity. Due to the high intra-cavity intensity, no focusing is necessary, which protects the crystal. For intra-cavity doubling, the output coupler can be replaced with a high reflector for the fundamental, which is also highly transparent for the frequency-doubled light. Since the crystal emits light in both directions in the resonator, the blue output power can be increased by placing a dichroic mirror behind the crystal. The advantages of intra-cavity doubling compared to external doubling are therefore high output powers, better beam profiles and longer crystal life times. Figure 4.8 shows a photograph of the intra-cavity doubling Ti:Sa laser at TRILIS.

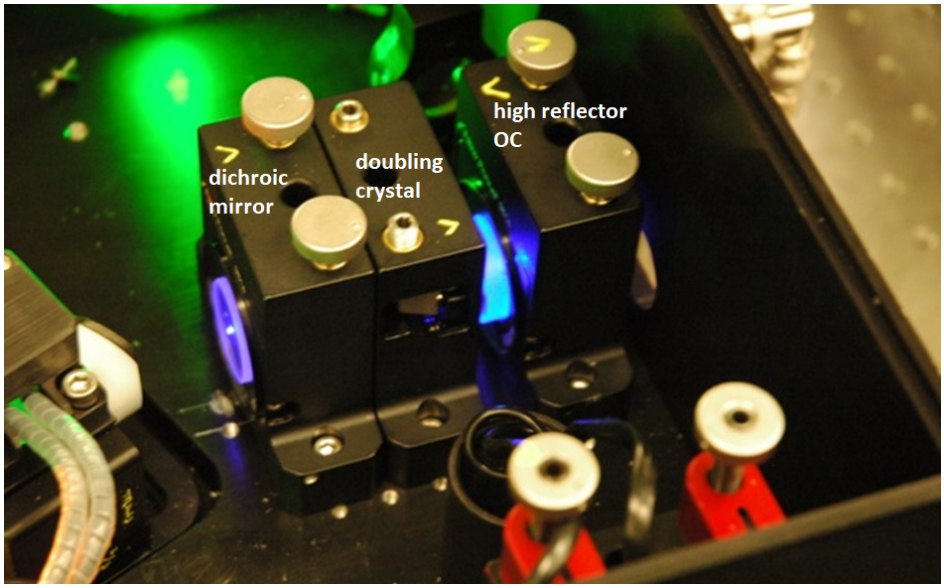

Figure 4.8: Linear arrangement of intra-cavity frequency doubled Ti:Sa laser using a dichroic mirror in the cavity. Dichro area vector must be exactly parallel to resonator beam for blue - blue beam overlap

The external cavity frequency doubling method is mainly used for automatic tuning and spectroscopy purposes which will be explained in the following section.

A recent development on intra-cavity doubling was performed in TRILIS using a 45° dichroic mirror in the cavity (Figure 4.9). The advantage of this method compared to the arrangement

shown in Figure 4.8 is that the etalon effect caused by the dichroic mirror in the cavity can be easily solved which makes the alignment easier and the tuning behavior smoother.

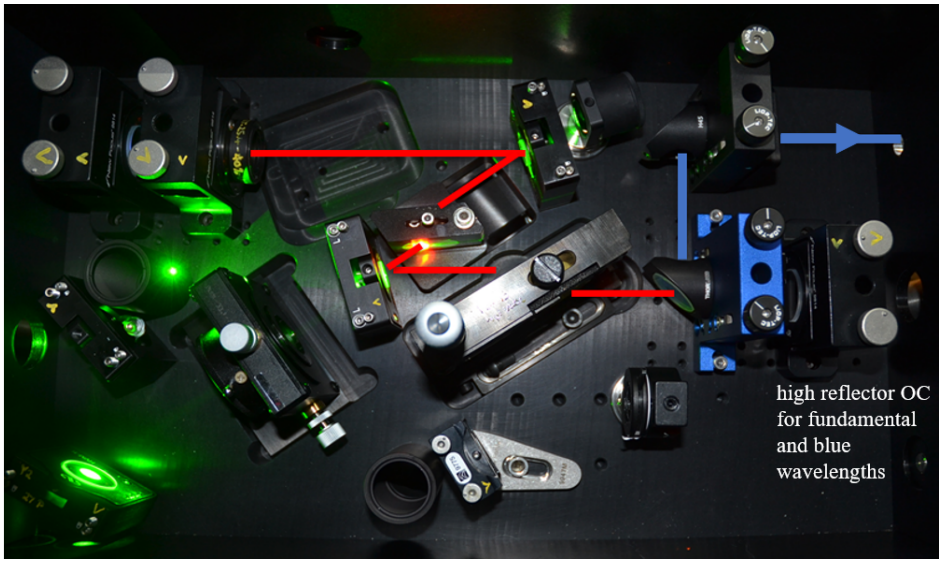

Figure 4.9: Intra-cavity frequency doubled Ti:Sa laser using a 45° dichroic mirror in the cavity.

4.4.1 Continuous, automated tuning of the Ti:Sa laser second harmonic frequency

The fundamental laser output from the grating laser is frequency doubled by a LBO crystal. To avoid the time consuming readjustments during hundreds-nanometer wide wavelength scans, the crystal was mounted on an automated rotary stage with an encoder. During scans, the crystal's optical axis was automatically rotated relative to the incident laser according to a grating-angle v.s. crystal angle calibration.

This automated system gave 80 – 90% second harmonic power that a manual adjustment could achieve. Due to the 8 mm length of the crystal and wide wavelength scans, the walk-off of the laser beam had to be compensated in order to provide proper spatial overlap of the laser beams in the ionization region. A commercial beam stabilization system [3] (more details in Section 4.6) was employed to compensate for the beam displacement caused by angle tuning of the doubling crystal.

[3]BeamLock Aligna 4D, TEM Messtechnik GmbH, 30559 Hannover, Germany

4.4.2 Automatic tuning of a THG Ti:Sa laser

For frequency tripled tuning, a BRF-tuned intra-cavity doubled Ti:Sa laser light was summed with the fundamental wavelength from a grating-tuned Ti:Sa laser. This allows for continuous wavelength scans covering up to 50 nm in the UV region. A layout of the Ti:Sa lasers in the off-line development laboratory and a schematic of the sum frequency generation setup is given in Figure 4.10.

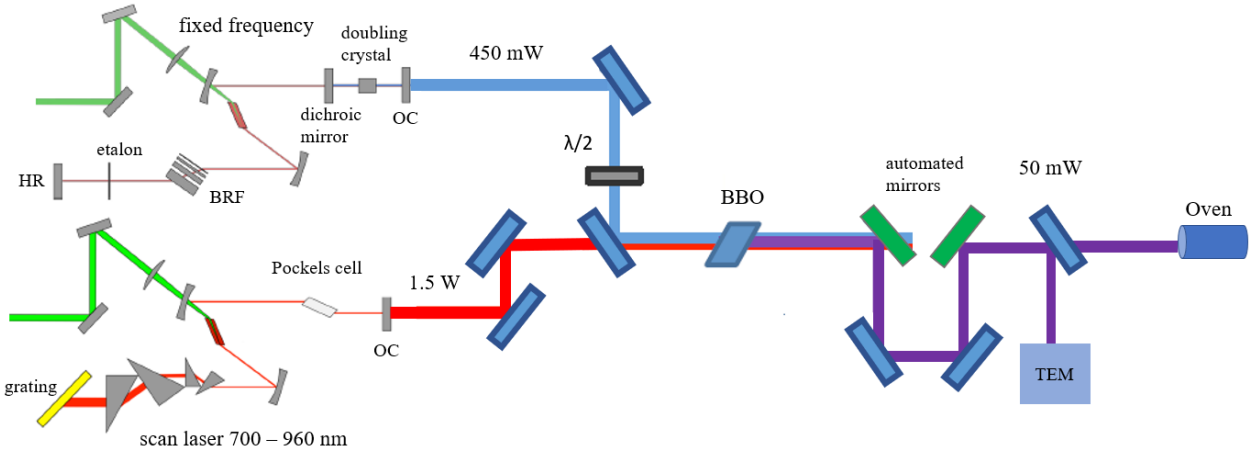

Figure 4.10: Sum frequency mixing allows for laser spectroscopy in the UV and extended ionization scheme development. The grating tuned Ti:Sa laser is equipped with a Pockels cell in the output arm to allow for pulse synchronization during the laser scan. Focusing lenses in the frequency mixing setup are omitted for clarity [16].

With this setup up to 50 mW of tripled (UV) light was available within a 50 nm overall continuous tuning range. Figure 4.11 represents a photograph of the frequency mixing for the radioactive astatine scheme development in the on-line laboratory in 2018.

4.5 Laser pulse synchronization

For resonant ionization the laser pulses have to reach the ionization region simultaneously. To this end, each laser can be equipped with a Pockels cell. The Pockels cell is based on the electro-optical effect, and consists of a nonlinear KDP crystal which converts linear polarized laser light to circular polarized under application of a high voltage (typically 1.5 kV to 6 kV). Due to the change

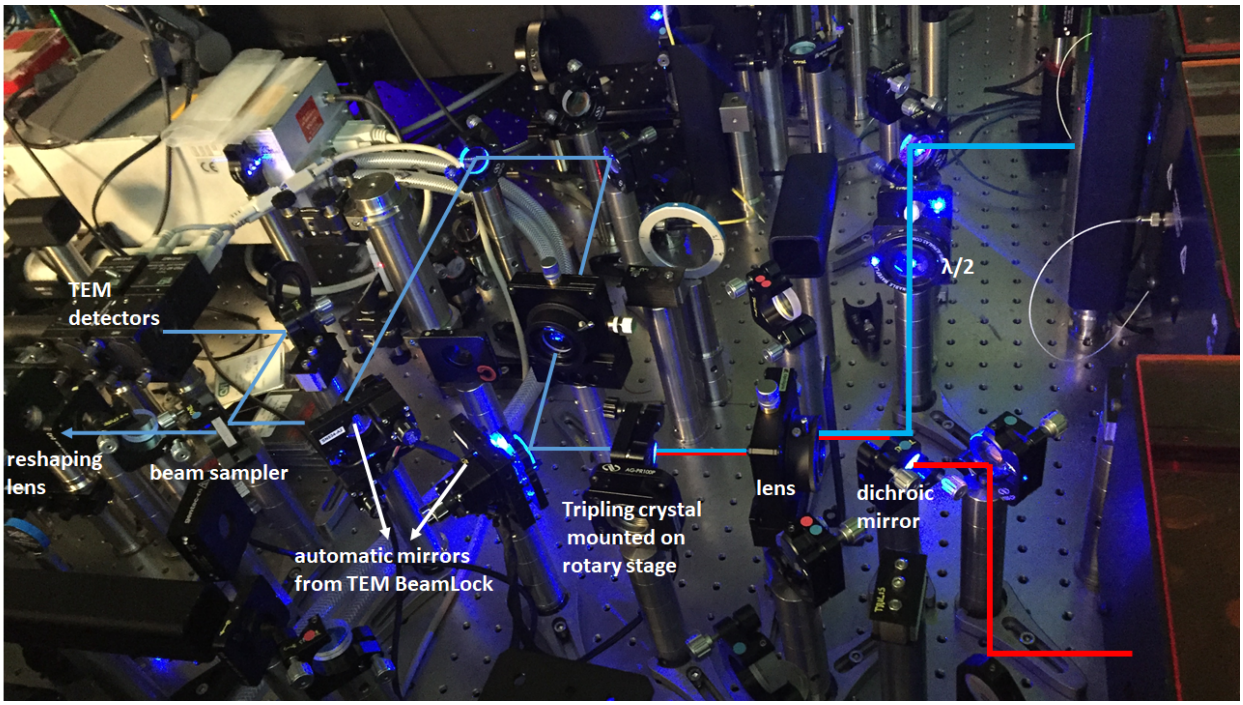

Figure 4.11: A photograph of frequency mixing for astatine experiment in 2018 to search for autoionizing states (on-line lab). As shown in the schematic of Figure 4.10 the grating-tuned Ti:Sa laser output and the output from a fixed frequency, intra-cavity frequency doubled Ti:Sa laser are overlapped in the tracked tripling BBO crystal.

of polarization, additional losses are introduced associated with the resonator which spoils the resonator Q-factor. By turning off the voltage, the crystal becomes transparent and the inversion can be accessed again [76]. If the time lag between two pulses is short, the synchronization can be realized passively by either adjusting the pump power, or changing the Ti:Sa crystal position in one of the resonators. The closer the focus is located to the front crystal surface, the earlier the laser starts lasing. Q-switching the Ti:Sa lasers can be avoided when operating multiple pump lasers that can be delayed with respect to each other.

4.6 Beam stabilization

Long term pointing as well as frequency stability is obtained passively by maintaining constant operating conditions for the Ti:Sa lasers, such as the Ti:Sa crystal cooling water and the laboratory

temperature. The observed frequency fluctuations are correlated to temperature fluctuations, which are kept below 0.2 °C and translate to long term frequency drifts within a 5 GHz band [16].

To actively compensate the walk-off of the laser beam resulting from rotation of nonlinear crystal's optical axis, a commercial TEM BeamLock 4*D* system was employed. Together, the control electronics, a combined angle and position detector and two active mirrors form a feedback loop, and suppresses thermal beam pointing drifts as well as fast pointing fluctuations. This locks the beam pointing to sub-micrometer precision. As shown in Figure 4.12, the laser beam steering is readjusted by two automated mirrors $A1$ and $A2$ (displacement and angle controls) after the doubling crystal, based on the images of laser pickup on two TEM position sensitive detectors (monitoring near-field and far-field respectively). To provide satisfactory precision in stabilizing the laser pointing over a long distance (about 5 m for off-line lab and 20 m for on-line operations), the distance of two TEM automated mirrors can be extended.

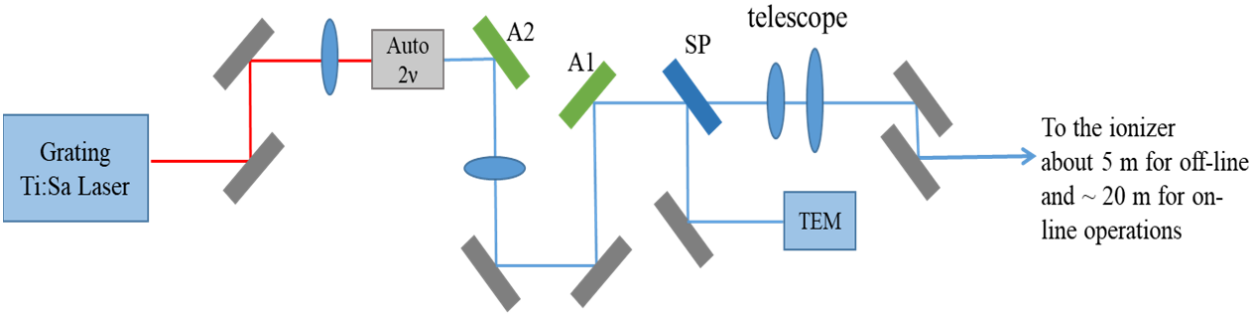

Figure 4.12: Diagram of the frequency doubled scanning Ti:Sa laser setup with following laser beam pointing stabilization setup. The system consists of TEM BeamLock with two automated mirrors $A1$ and $A2$ for beam pointing stabilization. SP: beam sampler, TEM: TEM BeamLock position sensitive detectors.

5 | Cr:Forsterite laser development

For operation at laser ion sources, a laser system shall cover a large tuning range in order to access resonances for as many elements as possible. The strongest transitions of the first excitation step for most elements are in the UV to blue region, while the second excitation step often lies in the VIS to NIR. Classical lasers with wide tuning ranges are dye lasers, which cover a wavelength range from the UV to NIR by switching between different dyes as a gain medium, different optic sets and different pump laser frequencies. Lasers were used and still are in use successfully at the first laser ion source in operation at ISOLDE CERN and Gatchina in Russia [19, 77]. However, these systems require maintenance and come with inherent fire and health hazards with respect to dye solutions. The lasers used at TRILIS are Ti:Sa lasers which are described in more detail in Chapter 4, cover the NIR region (680-1000 nm). Some shorter wavelengths from the UV to blue region (210-490 nm) can be reached by frequency conversion. The gap, in the visible spectrum (500-680 nm) was covered partly (584 to 672 nm) in this work with the frequency doubled light of a Cr:forsterite laser. External cavity frequency doubled light of a Cr:forsterite laser was first developed by S. Rothe using a TRILIS optics set and a Cr:forsterite crystal [78] at Mainz university. This system was applied to the spectroscopy of silicon (Si), scandium (Sc) and nickel (Ni). This work presents development of intra-cavity frequency doubled light of a Cr:forsterite laser at TRIUMF.

5.1 Characteristics of Cr:Forsterite crystal

Cr:forsterite (Cr^{+4}:Mg_2SiO_4) is a solid state laser material lasing in the range of 1150-1350 nm, which is just above the Ti:Sa tuning range and important for fiber communication applications. The second harmonic of Cr:forsterite partially fills the gap between the fundamental and second harmonic of Ti:Sa from 580-625 nm.

In the beginning it was thought that Cr^{3+} was responsible for the lasing action [79, 80]. However, spectroscopic analysis supported the theory that Cr^{4+} was the lasing ion and showed that the presence of Cr^{3+} in the host lattice actually decreased the efficiency of the laser due to two-photon absorption of the pump wavelength [81, 82]. Lasing action in the Cr^{4+}:forsterite gain material was first reported in 1988 [79, 81, 83]. In Cr^{4+} doped forsterite (Mg_2SiO_4) the lasing transition takes place between the electronic energy levels of the 3d electrons. The active laser ions are not shielded from the surrounding host lattice and, as such, strong electron-phonon coupling will take place and give rise to a broadly tunable output [84]. The SHG gain bandwidth of the output is a good alternative to Ti:Sa systems for shorter wavelength configurations. Furthermore, at room temperature Cr^{4+}:forsterite has an upper state lifetime of 2.7 μs. This upper-state lifetime is sensitive to temperature and by cooling to liquid nitrogen temperatures (77 K) the upper-state lifetime can be increased to 20 μs [85–88]. The thermal load from the pump beam inside the crystal can have a detrimental effect on this duration, because an increase of the crystal temperature causes a decrease in the upper-state lifetime. This necessitates a heat removal mechanism to keep the crystal at a constant low temperature.

Besides the necessity of heat removal mechanism to increase the life time of the excited states, it was also realized that the low thermal conductivity of the Cr:forsterite gain medium can be detrimental to optimal laser performance [89]. The high power laser pumping gives rise to the thermal lensing effect [90, 91] and thereby degrades the laser performance. This thermal effect also contributes to increasing the lasing threshold of Cr:forsterite [92–94]. A higher lasing threshold increases the

pump power requirement, resulting in a further increase in thermal effects. These issues are known from Ti:Sa laser design, but are more pronounced in Cr:forsterite laser.

Figure 5.1a shows the absorption spectrum of Cr:forsterite along the three symmetry axes of the crystal (a, b and c). The absorption maxima are slightly shifted from each other because of the crystal structure of forsterite.

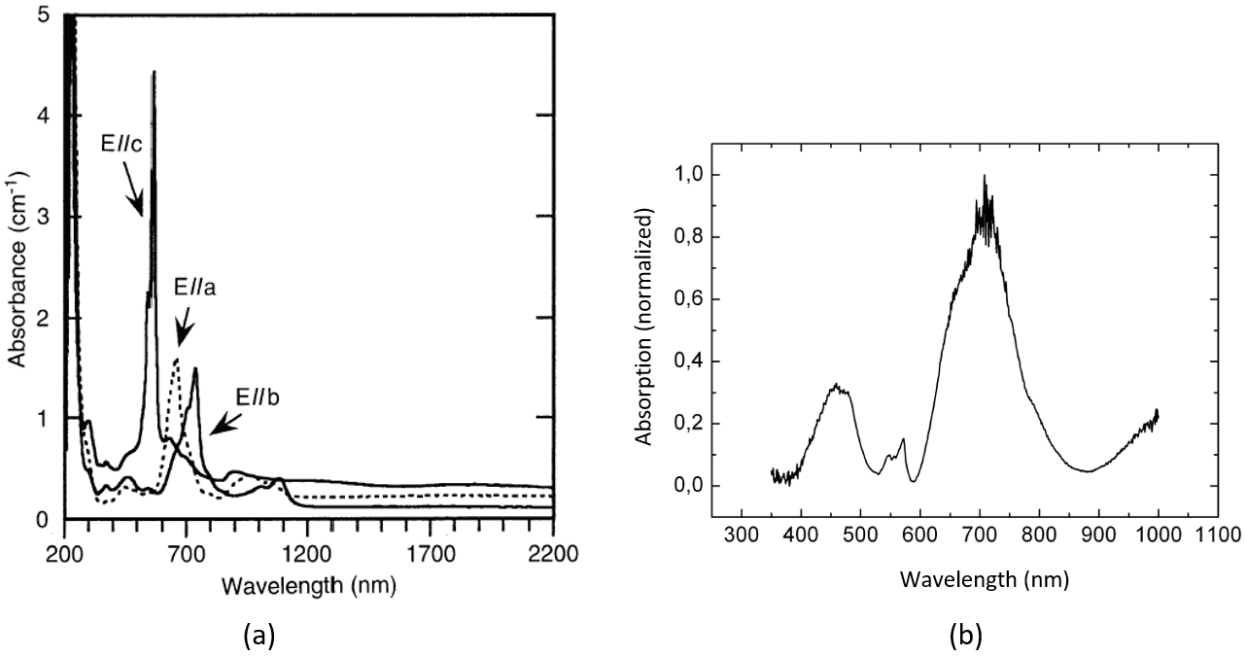

Figure 5.1: The absorption spectra of Cr:forsterite: (a) is a measurement along three axes, a, b, and c of the crystal, reproduced from [95]; (b) absorbance measurement of the crystal used for this work (b axis cut), reproduced from [78].

The crystal used in this work to construct the laser is cut along the b axis. Figure 5.1b presents the absorption spectrum recorded in the range of 350 nm to 1000 nm for the b axis cut. The maximum absorption is at 700 nm, which corresponds to the curve $E//b$ in Figure 5.1a. The absorption cross sections at wavelengths of 1064 nm and 532 nm are comparable, however significantly lower than that at 700 nm [96]. For the latter absorption band, Cr:forsterite laser can be pumped with a Ti:Sa laser [97]. The first Cr:forsterite laser was pumped at a wavelength of 532 nm [79]. Lasing using a Nd:YAG pump laser at a wavelength of 1064 nm was reported by [61]. The efficiency should be higher at this wavelength than that at 532 nm (frequency doubled Nd:YAG laser radiation),

because of the lower Stokes factor $S = \lambda_P/\lambda_L$, which is the ratio of pump wavelength λ_P to the laser wavelength λ_L. In anti-Stokes fluorescence the emitted wavelength is greater than the absorbed one. Since anti-Stokes fluorescence involves the emission of higher energy photons than those which were absorbed, the net anti-Stokes fluorescence can cause removal of energy from the material illuminated. Of course, it is essential that the quantum efficiency is high, and that nearly all anti-Stokes fluorescence light can leave the crystal without being re-absorbed.

5.1.1 Tunable solid state laser

Solid state lasers are categorized into two main classes depending upon the output spectral characteristics: rare-earth ion-doped solid state laser, and transition metal ion-doped solid state laser. In the former case, the electron-phonon coupling is reduced as a result of shielding between the $4f$ electron and the surrounding lattice by higher lying electrons, giving rise to a very weak interaction between ion and the surrounding lattice. The best member of this group is the Nd:YAG laser, where the optical amplification is obtained over a narrow spectral range and the emission wavelength does not vary significantly in different host media. In the second group of solid state lasers, also known as tunable solid state lasers, the host medium is doped with transition metal ions such as Ti^{3+}, Cr^{3+}, Cr^{4+} and so on. Lasing in this group happens as a result of transitions between the electronic levels of the $3d$ electrons. Because the laser active ion is not shielded from the surrounding lattice, strong electron-phonon coupling takes place which results in a broadly tunable output.

The total energy of the ion-lattice system is due to electron-phonon coupling which can be represented by so called "configuration coordinate" diagram (Figure 5.2).

Assuming that each ion has one vibrational mode and oscillates around the equilibrium point; in this case the eigenenergy can be treated as that of a harmonic oscillator ($h\nu_L(n + 1/2)$). Here ν_L is a classic frequency of ionic vibration mode and referred to as the phonon frequency. Using the Born-Oppenheimer approximation, the electronic and ionic states are treated independently in which case the total energy eigenvalue E_T is given by,

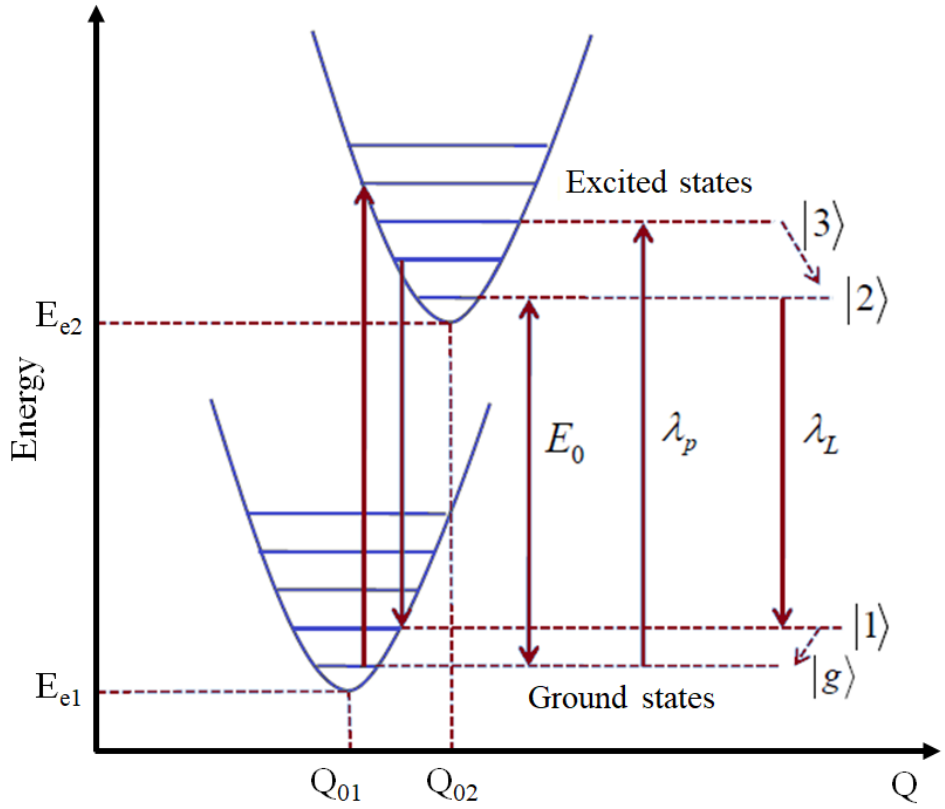

Figure 5.2: Configuration coordinate diagram showing the coupling between transition metal ion to vibrating lattice. Q represents distance between central active ion and the neighboring ion. This figure is reproduced from [84].

$$E_T = E_e + h\nu_L\left(n + \frac{1}{2}\right) \tag{5.1}$$

This shows that the total energy of the ion-lattice system is due to electron-phonon coupling. The lowest eigenenergy of the lattice-ion system is given by, $E_{el} + \frac{1}{2}h\nu_L$. When the system gets excited to higher electronic states with static electron eigenenergy E_{e2}, the coupling between ion-lattice also changes and equilibrium point Q_{01} shifts to Q_{02}. When the pump wavelength at λ_P excites the system from the ground state $|\, g\rangle$ to the excited vibronic states $|\, 3\rangle$, the system quickly relaxes/decays to the upper laser states $|\, 2\rangle$ by emitting a phonon, which is referred to as non-radiative decay. From the state $|\, 2\rangle$ the ion can make a transition to the $|\, 1\rangle$ states either by spontaneous emission or by stimulated emission [98]. Once the system is in the $|\, 1\rangle$ state, it undergoes rapid non-radiative decay to the ground state $|\, g\rangle$. Typically, non-radiative transitions occur much faster than radiative

transitions. Hence, ions excited to the $|\ 3\rangle$ states rapidly decay to $|\ 2\rangle$ and a fast decay from $|\ 1\rangle$ brings the ion back to the vibrational ground state $|\ g\rangle$. The inversion is reached when the population in the upper laser level $|\ 2\rangle$ is greater than the population of the lower laser level $|\ 1\rangle$. This can be achieved as the fluorescence lifetime ($\sim 3\ \mu s$ at room temperature) is longer than the lifetime of the lower laser level. So vibronic states behave with a very good approximation like a 4-level system and lasing can be obtained at reasonably low pumping levels. The lattice vibration consists of a large number of modes. Every mode has its own phonon frequency. The result of the large number of frequencies is to broaden absorption and emission bands. This effect is more pronounced at higher temperature since the upper vibronic level becomes populated to some degree which gives rise to the transition at different wavelengths.

Thermal conductivity of the crystal is an important parameter to determine the overall power performance of vibronic lasers such as Ti^{3+}:sapphire and a variety of chromium-doped laser. Figure 5.3 shows the wavelength tuning range of Cr:forsterite laser, Ti:Sa laser, the wavelength of the fixed frequency Nd:YAG laser and the combinations of the frequency conversions of these lasers.

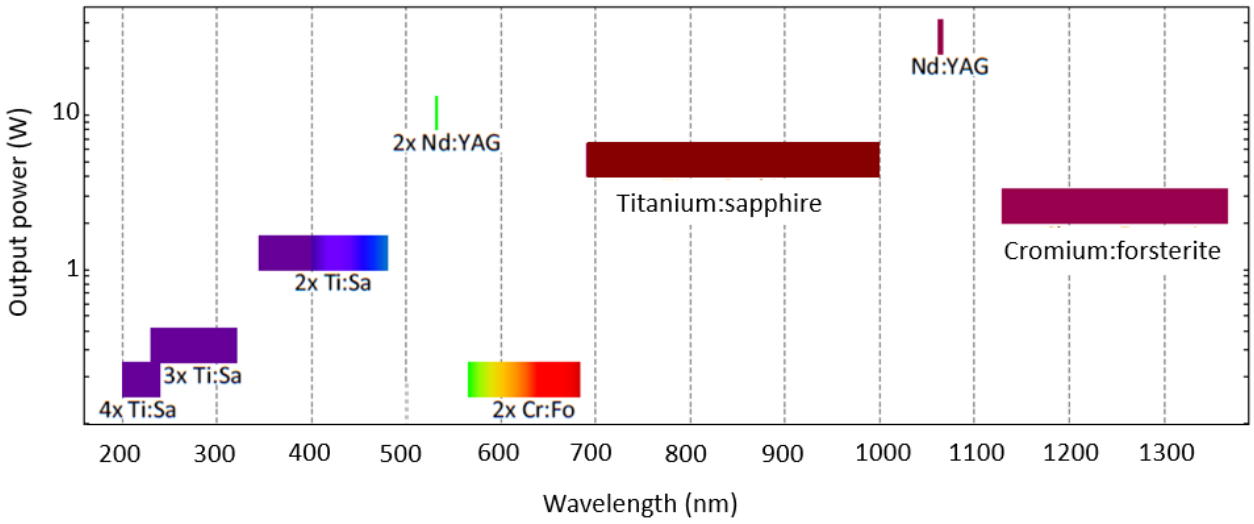

Figure 5.3: Tuning range of Ti:Sa, Cr:forsterite, and fixed Nd:YAG lasers, extrapolated by S. Rothe [78] and modified.

5.1.2 Absorption and fluorescence

The Cr:forsterite laser covers an important wavelength range in near-infrared spectral region from 1150 nm to 1350 nm, whereas its SHG can cover the visible region of spectrum, around 580 nm to 670 nm. Figure 5.4 shows the absorption and emission spectra of a Cr:forsterite crystal at room temperature ($25\,^{o}C$) [79].

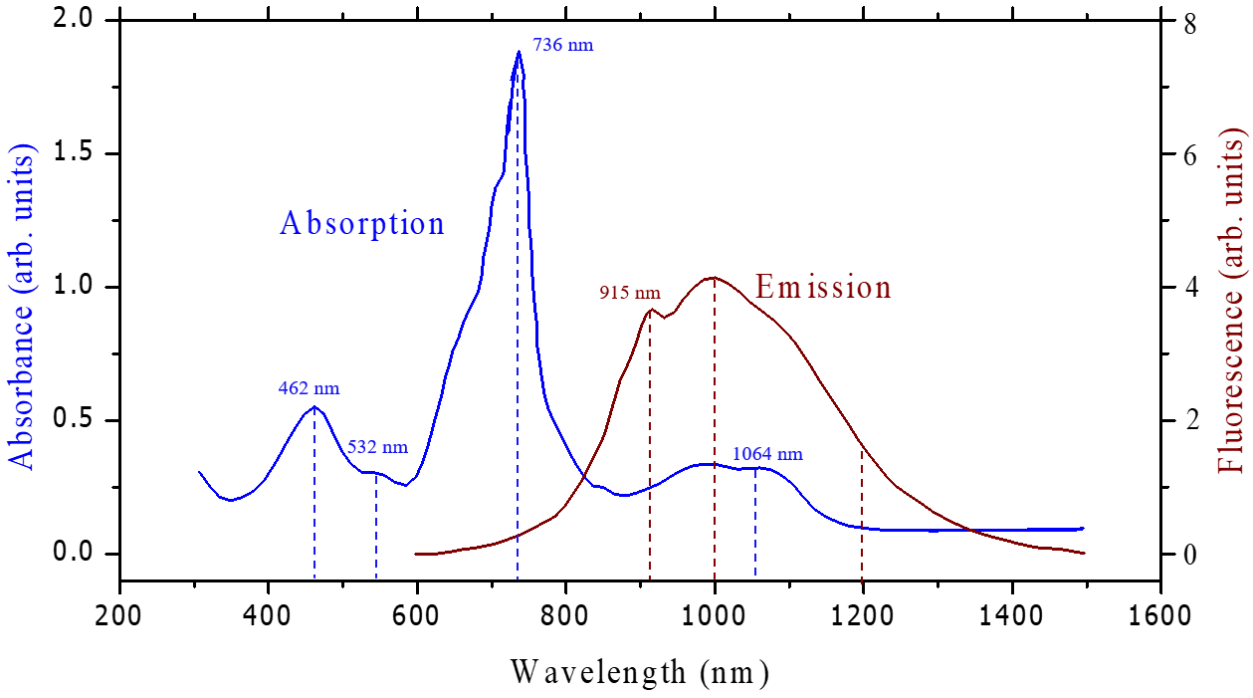

Figure 5.4: Absorption and fluorescence spectra of Cr:forsterite at room temperature, reproduced from [79].

There are two broad peaks in absorption spectra as shown in Figure 5.4, one at 780 nm and the other ranging between 900-1150 nm. This allows the crystal to be pumped optically by various commercially available lasers. Among them Nd:YAG laser at 1064 nm and ytterbium-doped fiber lasers at 1075 nm are the two mostly used.

5.1.3 Temperature dependent fluorescence lifetime

Cr:forsterite suffers most from the degradation of the lifetime of the pumping states and poor thermal conductivity [93]. These effects cause subsequent reductions in population inversion and

quantum efficiency of the laser crystal which thereby raise the lasing threshold and lower output efficiency. This is harmful especially for the gain media with low heat conductivity. Typically, various cooling methods are used to stabilize the crystal boundary temperature, however the heat load due to unused pump power (excited state absorption and non-radiative decay) can still lead to a considerable amount of local heating inside the crystal. Because of the temperature dependence of the refractive index, the heat load due to unused pump power can also cause a thermal lensing effect which can change the beam profile and power transmission inside the cavity [84]. But these problems can be minimized to some extent by choosing a crystal rod with reduced transverse dimensions [84]. The temperature dependent lifetime for Cr:forsterite and Ti:sapphire crystal reproduced from [93] is shown in Figure 5.5.

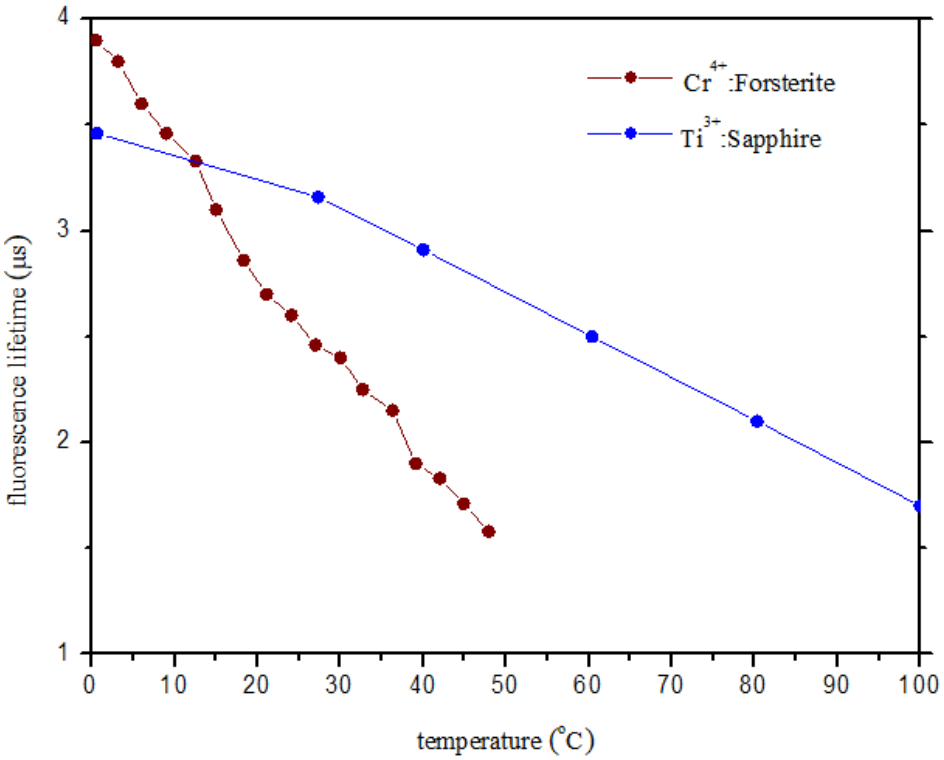

Figure 5.5: Temperature dependent lifetime data for Cr:forsterite and Ti:Sa gain media. Figure is reproduced from [93].

5.2 Cr:forsterite laser

The following sections will provide the information about the characteristics of the pump laser system, cooling system for Cr:forsterite crystal and the characteristics of the Cr:forsterite laser at TRILIS.

5.2.1 Pump laser features

The pump source for the Cr:forsterite laser is a pulsed Nd:YAG [1]. The laser is high power laser diode pumped and emits 1064 nm light in a spatial multi-transverse mode. The TEM_{00} mode can be achieved by placing a mode limiting aperture within the laser cavity. The laser is pulsed at 10 kHz. Figure 5.6 shows a structure of this laser. The individual elements are rail mounted. Due to linear structure of the laser, it is easy to adjust and the rail system allows for reconfiguration of the system. The standard cooling system utilizes an air cooled refrigerator. For TRILIS a water cooled refrigerator was chosen due to the limitations of the air handling system of the temperature stabilized laser laboratory. The water cooled refrigerator provides also quieter operating environment. Approximately 2 gallons of steam distilled water is used in the primary cooling circuit to the laser head. A temperature control valve maintains the temperature of the distilled water within $\sim 0.5\,^{o}C$ for optimum performance of the YAG crystal.

The laser at 1064 nm is randomly polarized. Since the Cr:forsterite crystal is cut at Brewster's angle, coupling with the unpolarized pump beam results in pump losses and consequently pulse fluctuation in the cavity. In order to achieve a well defined polarization, two Brewster windows (Brewster polarizer) were employed in the Nd:YAG LEE laser cavity in front of the OC. The intra-cavity Brewster plates allow for polarized laser output. Two plates were chosen to allow for beam displacement compensation. The main part of the laser light is *p*-polarized. At each Brewster surface, a fraction of the *s*-polarized light is reflected off, and the *p*-polarized beam is transmitted straight ahead. However, since the YAG laser has high gain and is pulsed, the actual

[1] LEE laser, LPD-100 MQG

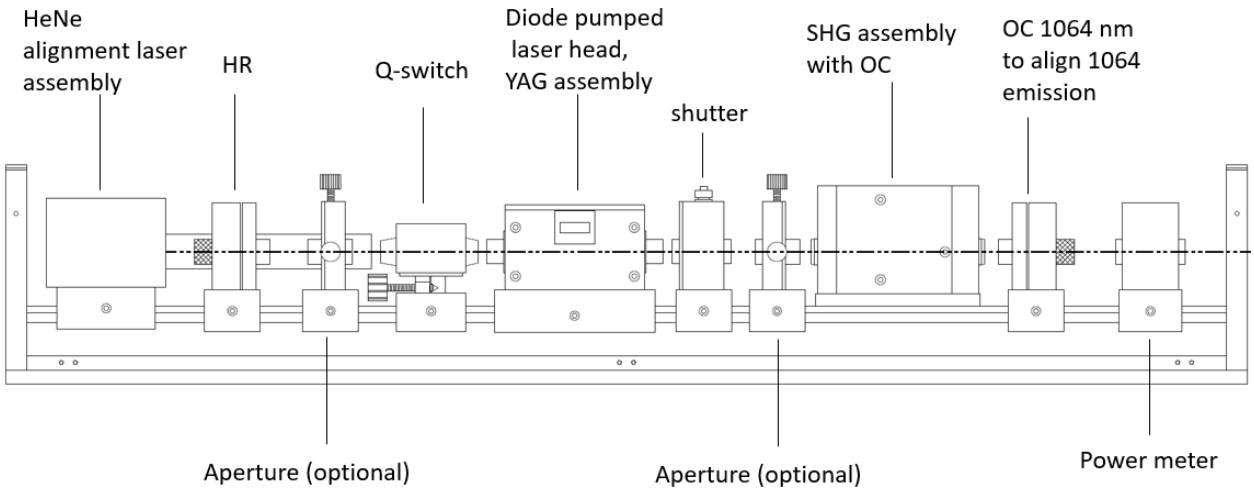

Figure 5.6: Construction of the Nd:YAG LEE laser 100MQG. The SHG assembly is replaced by the 1064 nm OC for 1064 nm operation. The drawing shows the side view of the laser resonator [99].

degree of polarization achieved is limited. Thus, a polarizing beam splitter cube (PBS) which splits p and s components of the laser beam and a $\lambda/2$-plate to adjust the power were placed at the exit of Nd:YAG laser. This allows to clean up the YAG-laser beam polarization, and for intensity adjustment without affecting the pump beam quality, which is a commonly encountered problem when adjusting the pump laser power via the diode current.

In Figure 5.7, the output power of Nd:YAG laser versus diode current is plotted.

A diode current of 14 A was employed for this work which results in 12.6 W pump power for Cr:forsterite laser.

5.2.2 Characteristics of the Cr:forsterite laser

The Cr:forsterite laser was constructed based on the existing laser resonator which was calculated and built for Ti:Sa lasers at TRILIS (more details in Chapter 4). The laser was pumped with the fundamental wavelength of Nd:YAG laser at 1064 nm. The schematic arrangement of the resonator as well as the beam path of the resonator mode (orange) and the pump beam (red) is shown in Figure 5.8. The focal length of the pump lens was chosen based on ABCD matrix calculations for

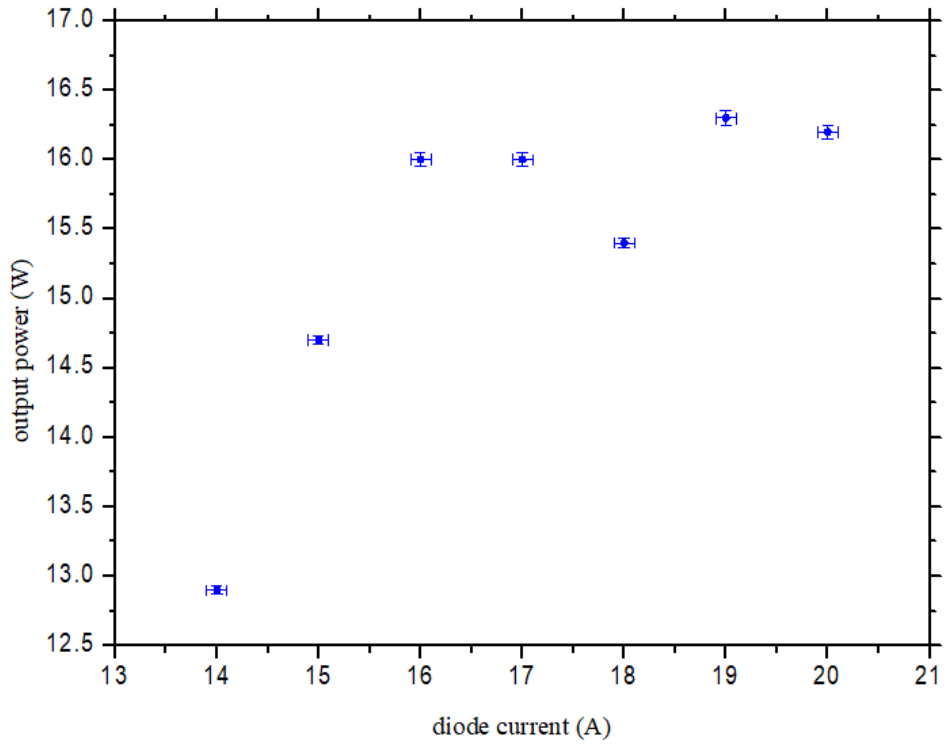

Figure 5.7: Performance of the Nd:YAG 1064 nm laser at 10 kHz pulse operation. The output power was measured after the PBS while the two Brewster plates were inserted in the LEE laser cavity.

a better overlap between resonator mode and pump beam. The focusing is behind the crystal to avoid possible damage from the high intensity pump beam.

For initial alignment of the resonator, a laser diode with emission at 1310 nm was chosen. The infrared radiation of the pump laser in the crystal can be detected with a commercial IR viewer.

5.2.3 Cooling system for Cr:forsterite crystal

To stabilize the laser, the crystal temperature plays an important role. To transfer the heat from the laser crystal to the water cooled crystal holder, it was wrapped with an indium foil and was clamped between two halves of a cylindrical copper plate. The whole package was inserted into the crystal holder. The bottom part of the crystal holder was replaced by a two stacks Peltier element [2]. The Peltier elements are connected in series and powered by a maximum of 2.9 A power supply.

[2]Lairdtech (MS series, 30×30 mm)

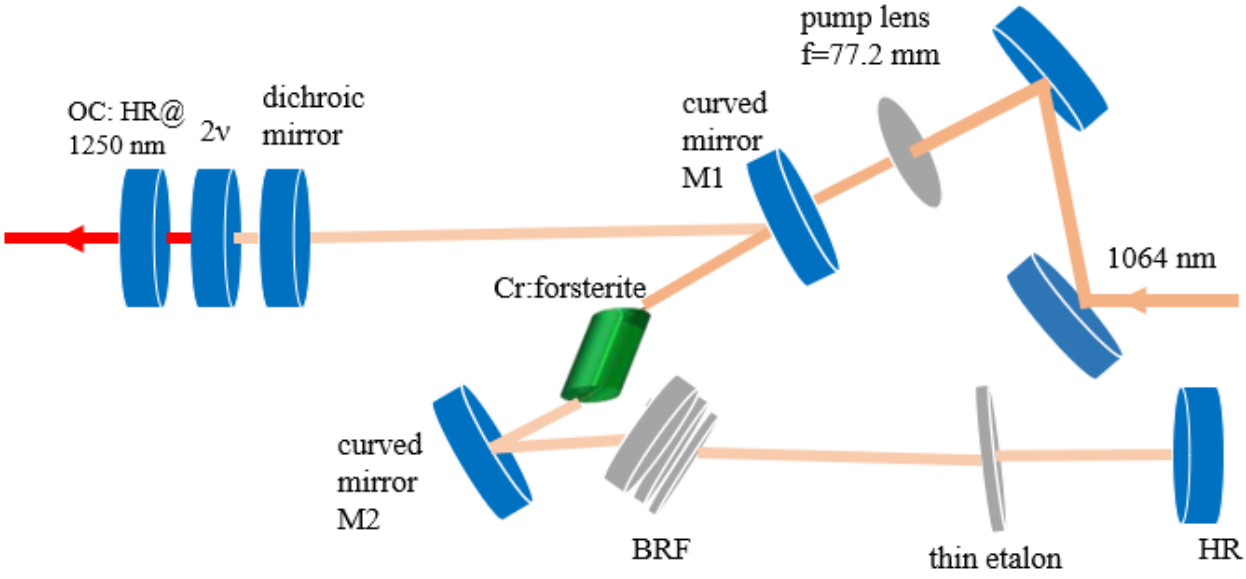

Figure 5.8: Schematic of Cr:forsterite laser resonator with intra-cavity frequency doubling. OC: output coupler, HR: high reflector, BRF: birefringent-filter tuned. The standard Ti:Sa laser optimized BRF are used for this development work.

Cooling water was supplied by a chiller. A simple housing made of aluminium with holes on the sides for the pump laser beam and the resonator mode as well as connections for dry air circulation [3], was placed on the crystal to avoid water condensation on the crystal.

5.3 Intra-cavity frequency doubled Cr:Forsterite laser

To avoid condensation on the surface of the crystal, for all the measurements in this work the cooling temperature of $15°C$ was chosen for the crystal (the optimum temperature is $5°C$).

The frequency doubled light of the Cr:forsterite laser is of particular interest for resonance ionization spectroscopy (i.e. for Si). For this purpose, a BiBO crystal was employed intra-cavity. To improve the performance of the laser and enhance the output power for doubled frequency laser, the output coupler was replaced by a high reflector mirror for fundamental wavelength and a dichroic mirror with high reflectivity for doubled frequency was placed in front of the doubling crystal. Figure 4.8 presents a photograph of this intra-cavity doubling system. The tuning range of the laser with

[3]PACU, THORLABS

two different etalons (0.5 mm and 0.2 mm) and without a dichroic mirror in the cavity is shown in Figure 5.9.

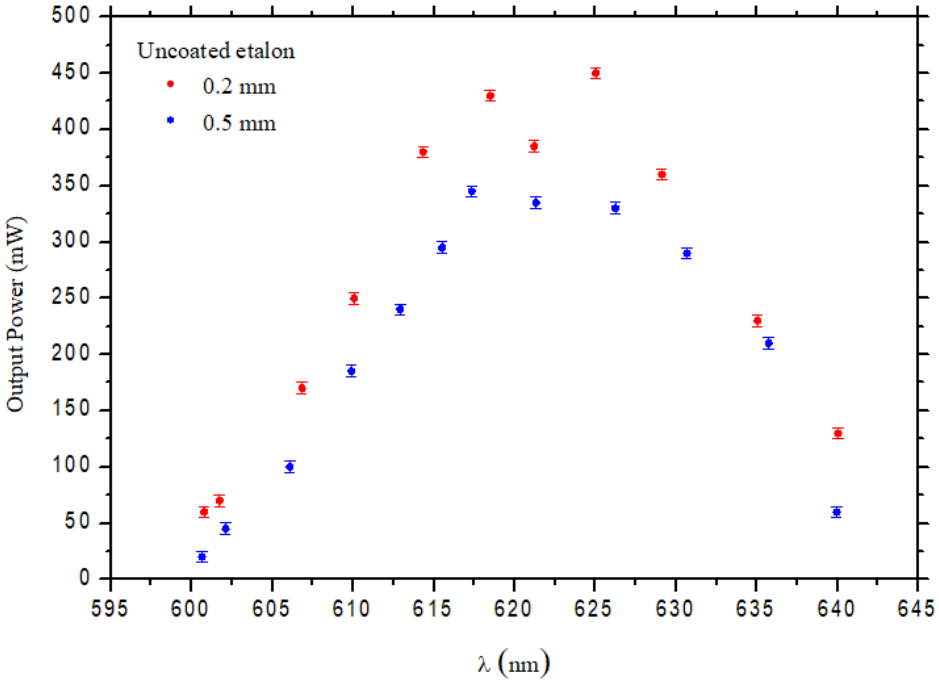

Figure 5.9: Tuning range of the intra-cavity frequency doubled Cr:forsterite laser without a dichroic mirror in the cavity. The measurements are performed for two etalons with different thickness of 0.2 mm and 0.5 mm. The pump power is 12.5 W and the temperature is 15 ^{o}C.

The linewidth of the laser for this cavity is $\sim$ 25 GHz.

5.4 Narrow-band Cr:Forsterite laser

The approach to reduce the laser linewidth in this work was to insert a second etalon with a thickness of $d = 1$ mm and 40 – 50% reflection for fundamental wavelength (1200 – 1500 nm) along with the uncoated 0.2 mm etalon into the Cr:forsterite cavity. This approach results in an additional linewidth reduction. Due to the lack of the space in the cavity, both etalons were mounted on the same holder. The relative alignment of both etalons has to be performed carefully to avoid multi-mode operation of the laser. To allow for manual mode cleaning, the mode structure of the laser was visualized in an ATOS LM007 wavemeter. The operation of this wavemeter is based on simultaneous detection of four Fizeau interferometer spectra. The four Fizeau-type interferometers

have different bases with free spectral range (FSR): 1000 cm^{-1}, 50 cm^{-1}, 2.5 cm^{-1}, and 0.1 cm^{-1} and the finesse F is 10.

All interferometers show a clean fringe pattern. The linewidth changes between $\delta\lambda$ = 200 – 700 MHz depend on the wavelength. The wavelength changes when the thin etalon is tilted and when the birefringent filter is tuned.

The maximum achieved power for the frequency doubled laser was 650 mW at $\lambda \sim 630$ nm and at a pump power of 12.5 W. The characteristics of the frequency doubled Cr:forsterite laser are shown in Figure 5.10.

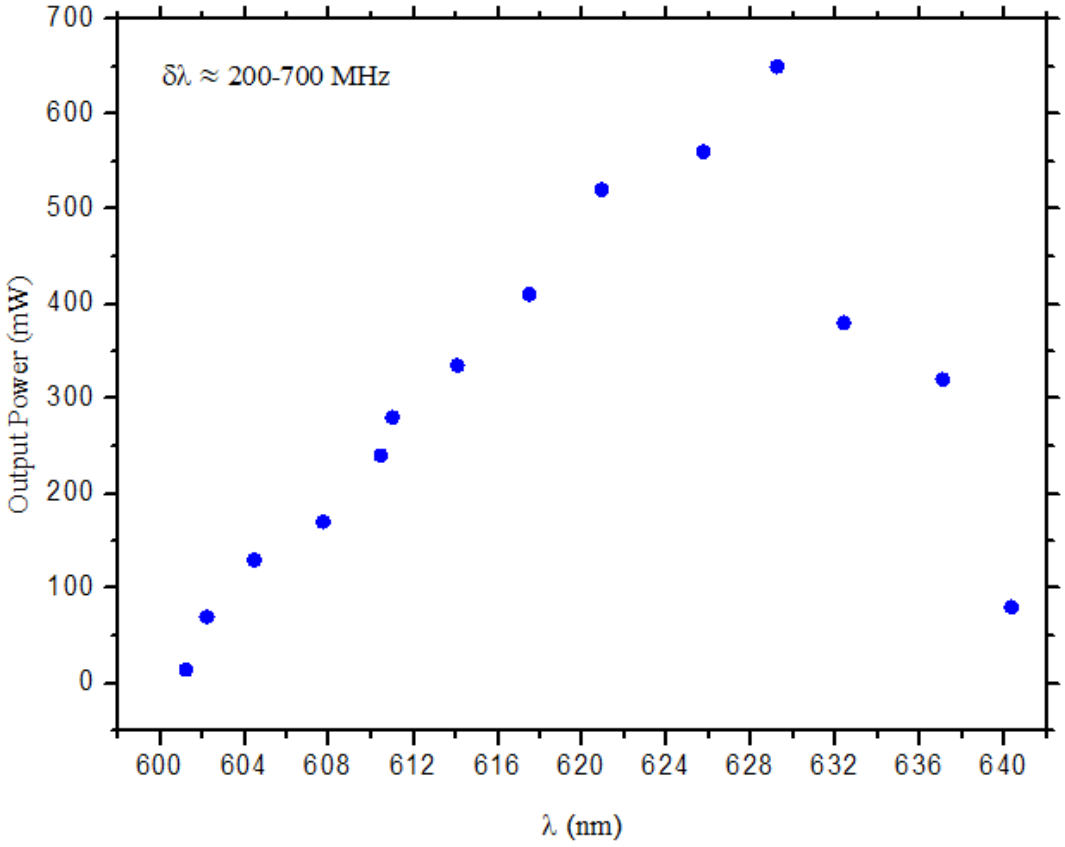

Figure 5.10: Tuning range of the intra-cavity frequency doubled Cr:forsterite laser with combination of a dichroic mirror, a birefringent filter, a thin uncoated etalon 0.2 mm, and a 1 mm etalon with 40 – 50% reflection. The measurements are performed with a pump power of 12.5 W and a crystal temperature of 15 ^{o}C.

5.5 Crystal temperature and laser output

The total performance and the stability of the Cr:forsterite laser significantly depend on the crystal's temperature. The performance of the laser for two different cooling temperatures of the crystal is shown in Figure 5.11.

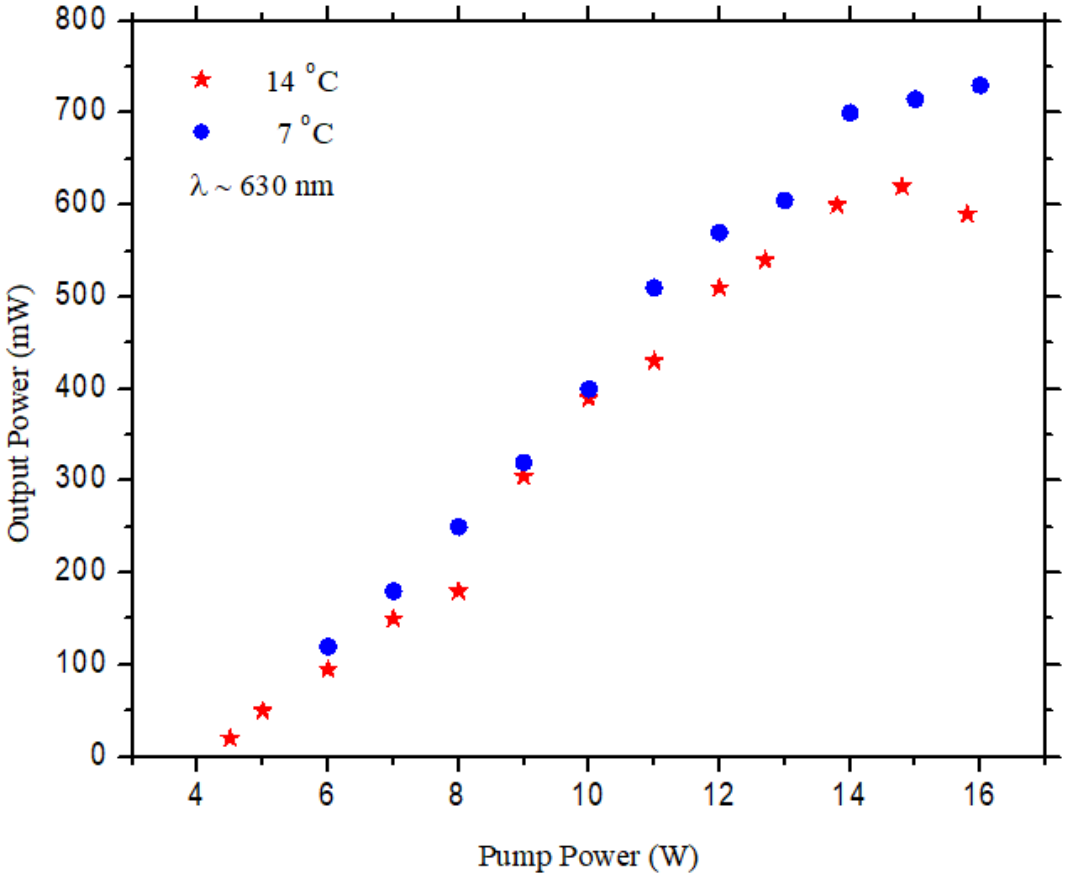

Figure 5.11: Performace of the Cr:forsterite laser for temperatures 7 and 14 °C at the peak wavelength $\lambda \sim 630$ nm.

To reach the optimal temperature of the crystal, a more powerful cooling unit is desired.

Part III

"Cold cavity" RILIS

6 | Ion guide laser ion source (IG-LIS)

Modern experiments at ISOL facilities like ISAC at TRIUMF depend critically on the purity of the delivered rare isotope beams. Therefore, highly selective ion sources are essential. The RIB delivered in ISOL facilities is composed of the mass separated beam of reaction products that effuse out of the target, make it in to the on-line ion source, be ionized and extracted. The mass separator magnet at ISAC was designed to accept an ion source emittance $\leq$ 30 πmm.mrad. As such the $m/\delta m \sim 2000$ with high throughput allows for some isobar separation up to $A/q \sim 30$. However, since ISAC RIB now are delivered up to $A/q \leq 240$ (mass to charge ratio), there is need for additional selectivity. Isobaric beam contamination often arises from surface ionization of elements with low ionization potential ($\leq$ 6 eV) on the hot target or transfer tube surfaces. The resulted background can be overwhelming when extracting exotic nuclides far from stability and produced at low rates. From a production point of view, the large background stems from the unfavorable abundance ratio for 'isotope of interest / background isobar'. The electronic structure of elements gives an avenue to use laser resonance ionization to provide element-selective ionization and enhance the yield of the isotope of interest. Although resonant laser ionization increases the yield of a desired element, delivered beams can still be overwhelmed by orders of magnitude higher surface ionized isobars. In these cases, the production of a sufficiently pure laser ionized beam requires a means of improving the RILIS selectivity or providing an electromagnetic isobar separator as planned for the ARIEL facility with $R \cong 20000$. This problem was tackled by developing a new type of ion source, the ion guide laser ion source (IG-LIS). This type of ion source as proposed by Blaum et al. [100] in the

form of the laser ion source trap (LIST) as a laser resonance ionization within a segmented radio frequency quadrupole (RFQ).

A first implementation of an IG-LIS (previously named RFQ-LIS) for off-line tests at ISAC was done in 2007 with a design [101, 102] for isobar suppression. Along the RFQ axis the electrodes are segmented into six sections. By applying DC potentials of $0 - 5$ V to the individual segments a potential gradient can be created inside the RFQ to assist longitudinal guidance and extraction of the ions. In 2013, a more robust redesigned IG-LIS was brought on-line. Through detailed thermal and ion optics simulation studies and off-line tests with stable isotopes [103, 104] a more robust and higher efficiency design had been developed. This ion guide laser ion source is presented in Figure 6.1. In a first on-line run with a silicon carbide (SiC) target, a suppression of surface-ionized sodium (Na) contaminants in the ion beam of up to six orders of magnitude was demonstrated [104].

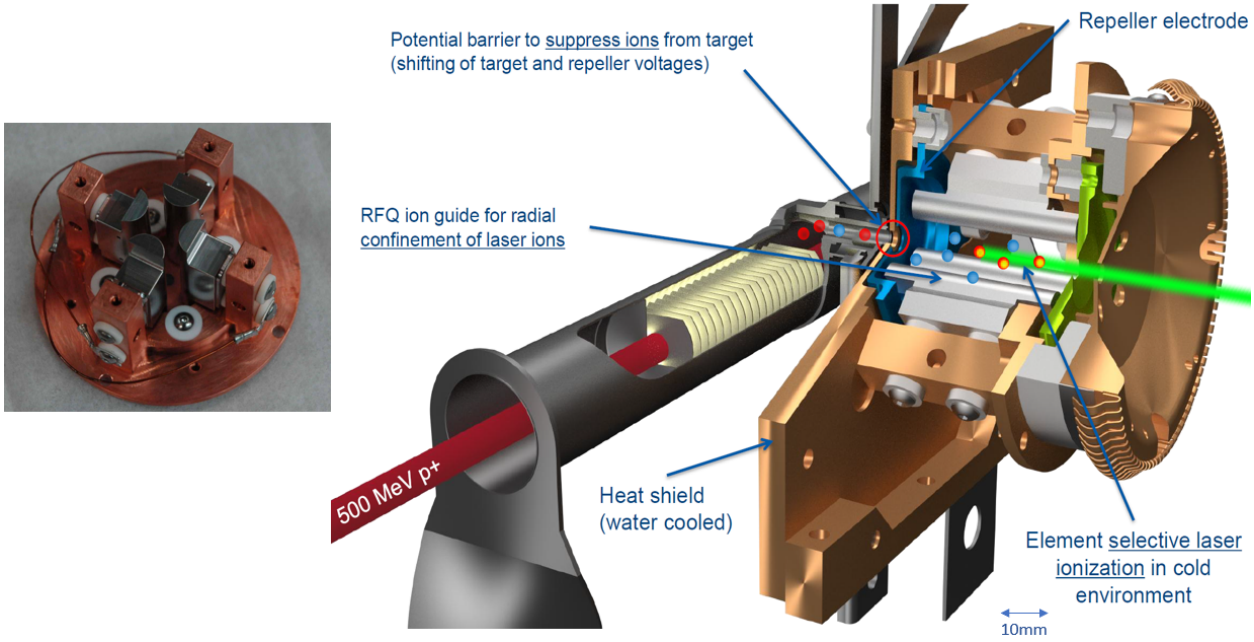

Figure 6.1: Technical realization of the IG-LIS at ISAC. Figure is from [103, 104]. It features from left to right: production target, heat shield, repeller electrode (blue), RFQ structure (gray), exit electrode (green), and extraction electrode. The inset photograph shows the RFQ electrodes attached to a monolithic copper mount [103]. The repeller electrode prevents surface ionized species from leaving the hot cavity target/transfer tube. Only neutral atoms are admitted to the "cold" ionization volume within the ion guide.

As part of this dissertation, operation and further improvements of this unique laser ion source were tested. An IG-LIS allowed key experiments on the exotic ISOL beams. The equivalent device, LIST, was developed at CERN ISOLDE [105–108] and the in-gas laser ionization and spectroscopy (IGLIS) technique was developed at KU Leuven [109]. A systematic study of the ion signal dependence on repetition rate and laser pulse energy was performed in offline tests in Leuven [110, 111].

A number of IG-LIS runs have been conducted successfully at ISAC. Isobar suppression of up to 10^6 has been achieved, however, IG-LIS operates at an intensity loss of $50\times - 100\times$ as compared to hot cavity RILIS which is still remarkable considering the achieved isobar suppression. The details about mechanical design and performance of the currently used on-line IG-LIS can be found in [103].

This chapter focuses on optimized operating parameters and design improvements for IG-LIS using SIMION [112] simulations for a more robust and higher efficiency on-line operation. The energy spread of ion guide is investigated for different operation parameters. Simulation results in this work were presented in PLATAN 2019 conference and will be published in *Hyperfine Interaction* journal [23]. The time of flight structure of extracted beams and gallium yield measurements for different on-line operating parameters used for experiments in 2017 are presented.

6.1 Linear radio frequency quadrupole structure

The linear quadrupole, originally developed for mass spectrometry by Paul and co-workers [113, 114], is widely used in many areas as a mass filter, an ion guide, or a linear ion trap. The history of the first 21 years of quadrupole devices has been given by Dawson [115]. His classic book describing theory and applications of quadrupoles, both two-dimensional and three-dimensional, was published more than 40 years ago. Since that time, there has been much progress in the development and use of quadrupoles in new ways. The book by March and Hughes [116], while mostly concerned with three-dimensional ion traps, contains much useful information about the

properties of ion motion in quadrupole fields that can be directly applied to two-dimensional linear quadrupoles.

The electric potential of the linear quadrupole, $\phi(x, y)$, is given by

$$\phi(x, y) = \left(\frac{x^2 - y^2}{r_0^2}\right)\phi_0 \tag{6.1}$$

where x and y are Cartesian coordinates. This potential is produced by four parallel electrodes with hyperbolic shapes, as shown in Figure 6.2. The point $(x, y) = (0, 0)$ is the center of the quadrupole. The parameter r_0, called the field radius, is the distance from the center to an electrode. Balanced potentials are normally applied between the x and y electrodes, that is, a potential $+\phi_0$ (radio-frequency field, RF) is applied to the two electrodes in the x direction and a potential $-\phi_0$ is applied to the two electrodes in the y direction. In this case the potential at the center of the quadrupole is 0. The electrodes have the same frequency while each set of electrodes have different phase.

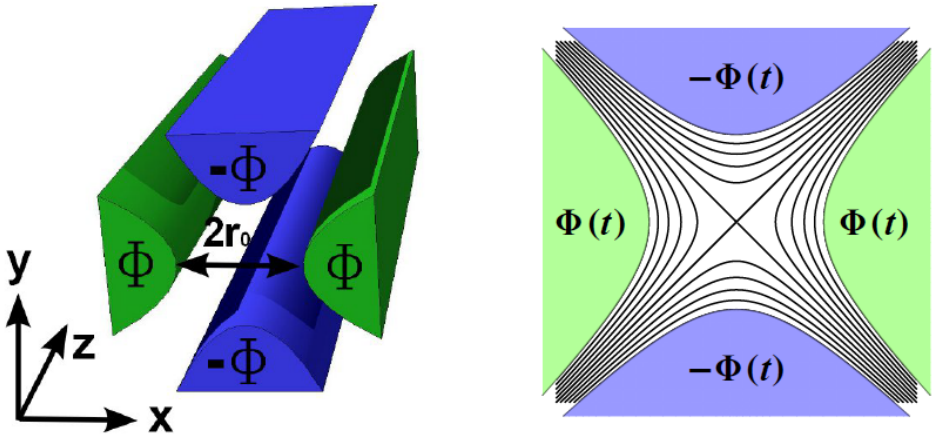

Figure 6.2: The quadrupole electrodes with applied potentials, showing equipotential lines (right). Reproduced from [117].

If unbalanced voltages are applied to the x and y rods a quadrupole potential is still formed, but there is an axis potential. Suppose the magnitude of the voltage applied to the x rods is ϕ_{0x} and to the y rods -ϕ_{0y}. The potential can be written

$$\phi(x,y) = \left(\frac{\phi_{0x} + \phi_{0y}}{2}\right)\left(\frac{x^2 - y^2}{r_0^2}\right) + \left(\frac{\phi_{0x} - \phi_{0y}}{2}\right) \tag{6.2}$$

where $((\phi_{0x} - \phi_{0y})/2)$ is the axis potential. This "float" potential simply sets the center line potential of the guide, and this allows the ion kinetic energy in the guide to be set.

The ideal RF source for ion guide/trap operation depends on the desired operating regime. For high resolution mass selection, as in conventional quadrupole mass spectrometers, a combination of high RF amplitude and dc difference potential creates conditions, where only ions in a narrow mass/charge (m/q) ratio range have stable trajectories. The stability is normally described in terms of two dimensionless parameters [115]:

$$a = \frac{8eV_{dc}}{mr_0^2\omega^2} \quad \text{and} \quad q = \frac{4eV_{RF}}{mr_0^2\omega^2}, \tag{6.3}$$

where V_{dc} and V_{RF} are the dc difference voltage and RF amplitudes, m is the ion mass, r_0 is the field radius, and ω is the RF frequency. By varying the RF:dc ratio, it is possible to adjust the range of masses transmitted (the interval q_{min} to q_{max}). For optimal operation q is set to 0.7060, and a is set in the range from 0.232 to 0.237 [115]. Clearly, for mass-selective operation the RF frequency and RF and dc difference voltages are all quite critical. The region of stability and ion trajectories are shown in Figure 6.3.

6.1.1 $\mathbf{r}_{rod}/\mathbf{r}_0$ ratio

While hyperbolic electrodes can produce the best approximation to a quadrupole field (aside from construction errors and the finite truncation of the electrodes), round rods are often used because they are easier to manufacture and mount to high precision.

In Cartesian coordinates, a two-dimensional potential can be expanded in multipoles $\phi_N(x,y)$ as

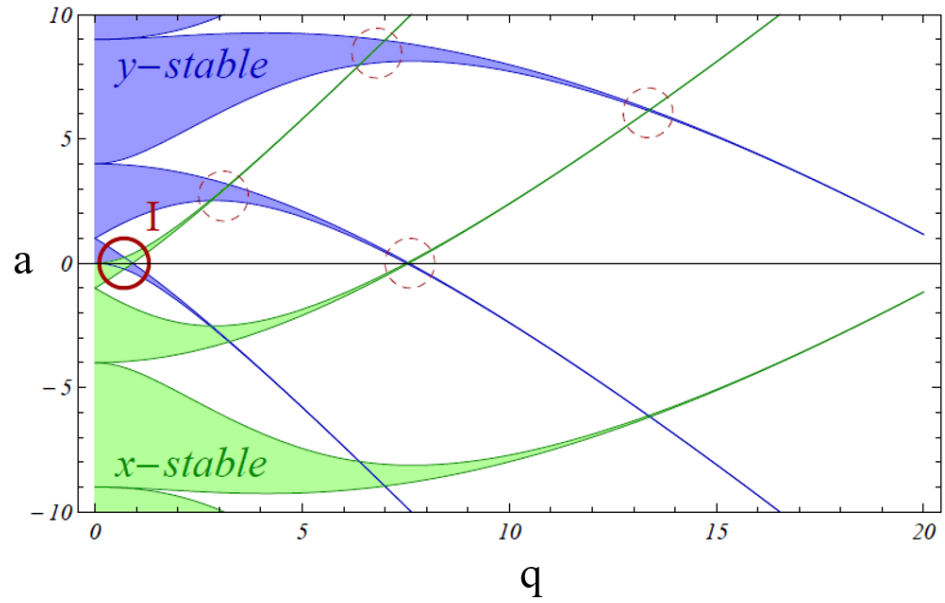

Figure 6.3: Regions of stability for the x and y motions in a linear quadrupole [117]. Circles guide to regions where simultaneous stability in both, x and y is given. Usually only the first region of stability (I) is used for practical reasons. Reproduced from [117].

$$\phi(x,y) = \sum_{N=0}^{+\infty} A_N \phi_N(x,y) \tag{6.4}$$

where A_N is the dimensionless amplitude of the two-dimensional multipole $\phi_N(x,y)$.

If the quadrupole electrodes have fourfold rotational symmetry, the symmetry of the potential requires that the amplitudes of higher multipoles are 0 except A_2, A_6, A_{10}, A_{14}, ... [118]. Several authors have discussed the ratio of rod radius r_{rod} to field radius r_0 that is optimum for a mass filter. With round rods, additional higher order multipole forms are added to the potential Equation (6.4). A ratio $r_{rod}/r_0 = 1.10$ was proposed to minimize losses from nonlinear resonances [119]. Gibson and Taylor [120] used trajectory calculations to simulate peak shapes for quadrupoles with hyperbolic and round rods with a ratio $r_{rod}/r_0 = 1.148$ and found that the round rods produced tails on the mass peaks, especially on the low mass side. They subsequently investigated the effects of the ratio r_{rod}/r_0 on the performance of a quadrupole and proposed that a ratio 1.12 to 1.13 would give the highest resolution and transmission [121].

The A_6 and A_{10} terms have similar magnitudes but opposite signs and compensate for each other. The A_6 term shifts the pass band to low mass. The A_{10} term shifts the pass band to high mass. When both are present with the correct amplitude, the pass band corresponds to that of an ideal field. Thus, a ratio r_{rod}/r_0 that makes $A_6 = 0$ does not produce the best mass filter. A ratio $r_{rod}/r_0 \approx 1.128$ is preferred [122].

6.1.2 RF ion guides

If a quadrupole is operated in RF-only mode, that is, with only RF between the rods, the Mathieu parameter a = 0, ions of a broad range of m/q values will lie on the $a = 0$ axis and have stable trajectories in the quadrupole. The quadrupole can be used as an "ion guide" to transport ions from a source to an analyzer. This provides the widest range of q-values for stable transmission possible, from $q_{min} = 0$ to $q_{max,sine} = 0.908$ [115]. The quadrupole thus acts as a high-pass mass filter, providing transversal confinement and therefore high transmission for all ions with masses

$$m > \frac{4eV_{RF}}{0.908\omega^2 r_0^2}. \tag{6.5}$$

Safe operating conditions require lower q values (< 0.3 for a quadrupole), and this is typically achieved by using higher RF frequencies, and/or lower RF amplitudes [123]. Under these conditions, the RF and dc voltages are not so critical, and a simple RF circuit can be used.

6.1.3 Ion guide driven by square wave RF

Richards et al. [124] in 1973 showed that a quadrupole mass filter can also be operated with a periodic rectangular waveform, like that shown in Figure 6.4. They considered the case where $|V_1| = |V_2|$. The claimed advantages are that more precise control of the waveform may be possible and, during the periods of constant voltage, the solutions to the equation of motion can be obtained analytically.

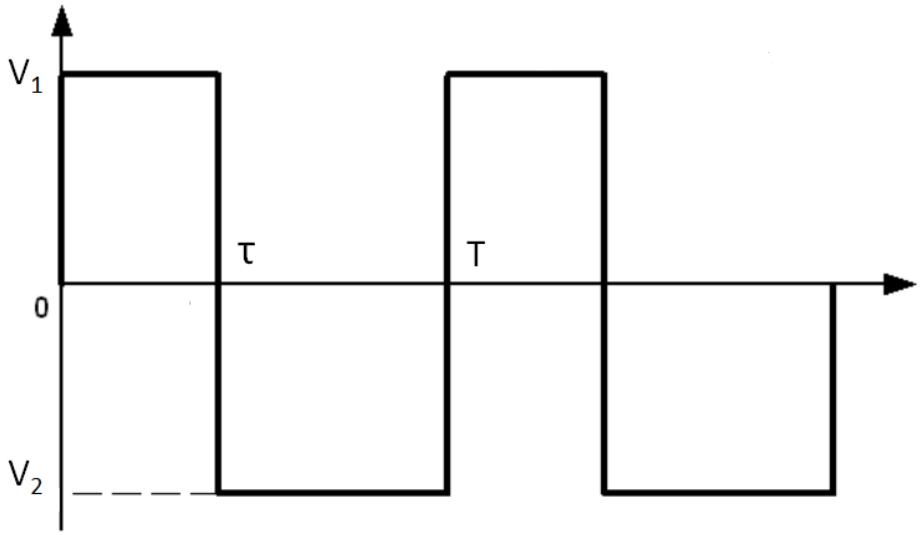

Figure 6.4: A rectangular waveform for use with a quadrupole mass filter. In general, $V_1 \neq V_2$ and the ratio τ/T can be adjusted.

If the ratio τ/T is set to 0.390, the stability region shrinks to a small region on the q axis and so mass analysis is possible with no DC component to the waveform [124]. The stability diagrams for a variety of rectangular waveforms are described in [125].

In particular, the maximum value q_{max} for stable transmission in the ion-guide mode without a dc potential V_{dc} drops from $q_{max,sine} = 0.908$ to $q_{max,square} = 0.713$ [126] and the tip of the first region of stability shifts to smaller values of q as well (Figure 6.5). Thus, overall lower amplitudes of the RF potential are needed to affect ions comparable to the sine mode. Consequently, the much faster transition between opposite amplitudes for the square wave and therefore higher energy transfer to the ions per cycle is given.

The developed quadrupole in 2013 at ISAC, was aimed to guide ions and therefore uses an square wave driven RF-only mode. It was operated with a square wave potential since the equipment for digital signals was already available and allowed simple adjustment of the driving frequency and duty cycle. With a field radius of $r_0 = 5$ mm, a frequency range of $1 - 3$ MHz and RF-amplitudes up to 100 V, singly charged ions with masses from 2 to 200^+ amu can be transmitted.

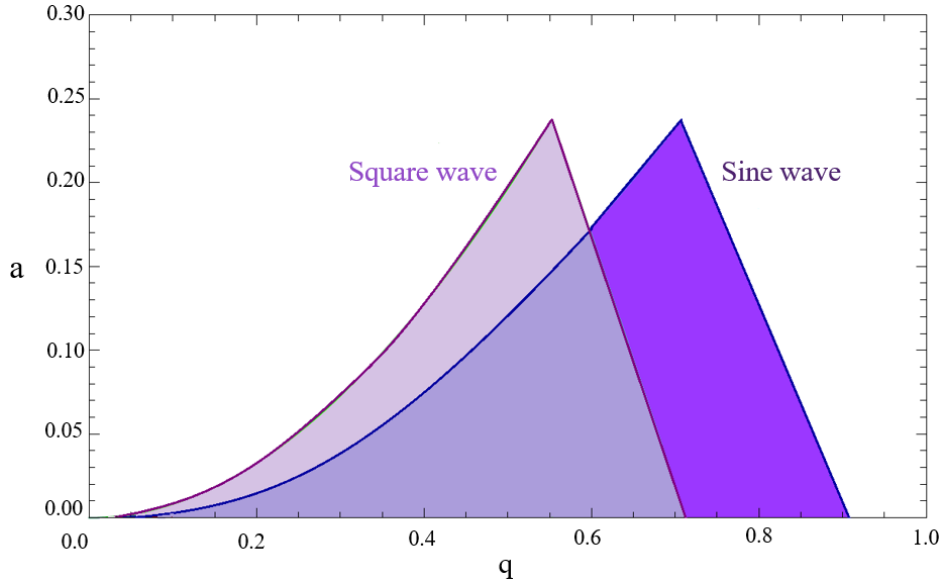

Figure 6.5: Comparison of the first stability region for quadrupole in square wave mode and in sine wave mode. Similar in shape, however, the square wave region is shrunken to lower values of q [126]. The sine wave driven RFQ is typically driven as a resonant ("tank") circuit configuration, whereas the square wave driven RFQ is typically driven directly from a switched DC supply.

6.2 IG-LIS concept

If the laser ionization process takes place outside of the hot cavity, it is possible to repel the surface ions effusing from the target with an electrostatic electrode and to only extract nuclides ionized by resonant laser ionization within a cold environment behind this electrode (Figure 6.6). This presents some technical challenges such as obtaining a geometrical overlap of the expanding atom beam from the hot cavity with RILIS beams. The best overlap is achieved with the laser beams directed towards the ionizer cavity. Whilst this is also the optimal geometry for creating laser ions inside the cavity, the laser ions generated inside the hot cavity will be rejected along with the repelled surface ions. Since the laser ionization efficiency inside the cavity is typically $< 10\%$, this loss factor is not the primary concern for this technique. Greater challenges are designing the laser interaction region itself and producing a device that is suitable for on-line operation in a hostile radiation and high-temperature environment.

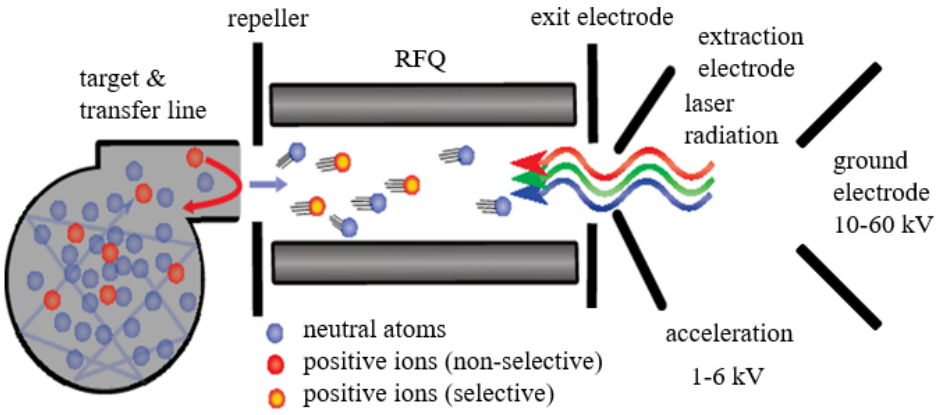

Figure 6.6: Concept of the IG-LIS. Ions released from the target are efficiently suppressed by electrostatic potentials, while neutral atoms can enter the interaction region behind the repeller electrode. The ions created by element selective resonant laser ionization in this cold environment are guided toward the high voltage extraction field by a linear RFQ. The picture is reproduced from [103].

The design is based on some key requirements for the laser interaction region. For optimal laser-atom beam overlap, the laser interaction region should be as close to the cavity as possible. The ions must be confined along the axis of the RFQ using a transverse potential and guided towards the extraction field using a longitudinal potential. Furthermore, the device should be easily switchable to a transmission mode, whereby ions originating from the hot cavity are transmitted. The divergence of the atomic beam translates into an emittance of the ions produced by resonant laser ionization that may exceed the acceptance of the extraction optics and thus would produce high losses. In order to keep the energy spread of the extracted ions low, laser ionization should take place in a longitudinally field-free region. To compensate for these two effects, the ionization volume is surrounded by a radio frequency driven linear quadrupole and terminated by another electrode similar to the repeller, called exit electrode. The exit electrode serves to shield the extraction field and can be used to manipulate the transmission through the quadrupole by shifting the electrodes potential.

Intended on-line application of the IG-LIS imposes a number of requirements and constraints to its design as any ion source has to be accommodated inside the existing ISAC target unit. The technical requirements and constraints are explained in details in [103, 104].

6.3 IG-LIS simulations

To develop a next generation IG-LIS, a better physical understanding of the IG-LIS prototype, ion optics, and its limiting factors are possible through simulations. The charged particle trajectory simulations of IG-LIS were carried out in SIMION 8, a software developed for step by step simulations of charged particle trajectories in static electric and magnetic fields [112]. All electrode geometries used for the simulations in this work were created using so-called geometry files (GEM files). The source code (written in Lua) for an implementation of a square wave driven RFQ and GEM files are part of H. Heggen's master thesis and can be found in [103].

Except for a graphical representation of ion trajectories inside the electrode model, SIMION does not provide any tools to analyze the results of a simulation. Therefore, the external program [1] records the situation of the simulated particle at the start, at the time of ionization (if ionization occurs) and after the final time step (when the particle hits an electrode or leaves the simulation volume) for every simulated trajectory. The statistical evaluation of a set of simulated particles with initial conditions [$\vec{V}$, $\vec{X}$, t, ...] is performed afterwards using a Mathematica notebook that reads the recorded data and determines characteristic parameters such as the transmission efficiencies of ions created by laser ionization and of ions created inside the source. The Mathematica source code used for the evaluation can be found in [103].

6.3.1 Assumptions

In order to faithfully represent reality in simulations, they must represent the correct physics, as well as a correct set of physical input parameters. The source code was taken from [103] and adapted as necessary for the simulations in this work that is exploring new ion guide configurations and operating modes of IG-LIS as encountered experimentally from optimization in on-line operation. Some of these operating modes were associated with ground faults encountered during on-line experiments.

[1] Lua

The grid resolution for the electrode models in SIMION was set to 0.1 mm. Particles are created as neutral atoms, uniformly distributed over the 3 mm diameter cross section of the transfer tube (red electrode in Figure 6.7), 0.5 mm from the end of the tube facing the repeller (green electrode).

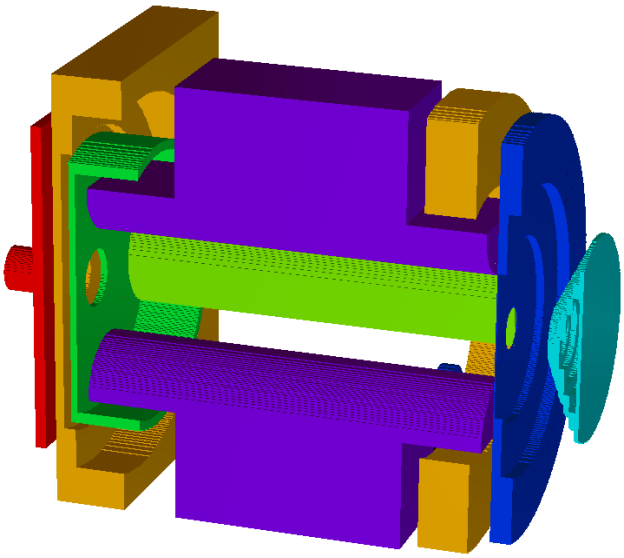

Figure 6.7: Electrode models used for simulations. Different colors mark electrodes of different potential: Source/transfer tube (red), heat shield (yellow), repeller (green), quadrupole electrodes (purple and light green), exit electrode (blue) and extraction electrode (cyan).

Each particle is assigned an initial direction vector and an initial velocity. The direction vectors are randomly chosen from the set of vectors uniformly distributed within a cone with 36° opening angle, representing the effusion of an atomic beam from the tube. The kinetic energies are created randomly according to a Maxwell-Boltzmann distribution at 2000 K. To simulate the behavior of the laser ion source, ionization happens every 100 μs for each particle, equivalent to the 10 kHz repetition rate of the laser system. Any neutrals entering the laser volume (a cylindrical volume with radius $r_L = 1.75$ mm around RFQ axis, equivalent to laser beam radius) is considered to be laser ionized. To make the program run time efficient, the laser ionization efficiency was set as 100%.

The final position and velocity vectors are recorded together with the total time of flight and a marker indicating if the particle was ionized.

By simulating one particle at a time, the simulations do not take any space charge effects into account which can appear for higher beam intensities. Ion-ion interaction can cause an additional defocusing force in the beam and therefore influence the performance of the ion guide.

6.3.2 Limitations of the simulation environment

The simulation environment does not allow to simulate the effusion of particles through the transfer tube and therefore the loss of particles due to laser or surface ionization inside the transfer tube is neglected. The laser ionization efficiency is assumed to be equal to unity in order to record more ions per simulation and obtain better statistics. Space charge effects are not taken into account in simulations which might be important for higher beam intensities. The repulsion of the ions among each other can cause an additional defocussing force in the beam and thus influence the performance of the quadrupole. Additionally, space charge effects might affect the potential gradients between source and quadrupole and could therefore also have an impact on the suppression characteristics of the RFQ - LIS. The same holds true for charge effects caused by continuous vapor deposition on the repeller or the quadrupole electrodes. Another effect that is not taken into account in the simulations are electrons that can be emitted from the hot surfaces inside the source. For the most intuitive operating mode, where the source has a negative potential compared to the repeller in order to suppress positive surface ions, free electrons from the source are accelerated towards the repeller. On the one hand, this can effectively shield positive ions traveling with the electrons from the repelling potential and therefore give rise to contamination. On the other hand, contamination may be created by non-selective electron impact ionization of neutral atoms behind the repeller due to the produced electron beam. Although the behavior of electrons in the setup can be simulated, the actual amount of free electrons in the source and their resulting impact is difficult to estimate. Besides the aforementioned neglected effects, the simulations represent an ideal environment regarding the mechanical configuration of the quadrupole. The simulated performance does not include any effects caused by field distortions resulting from misalignment of the RFQ electrodes.

6.3.3 Potential array calculations along the beam axis

At ISAC, the ion source has to withstand the harsh environment close to an on-line RIB production target and for typical production periods of up to five weeks. The temperature of the production target reaches 2300 °C and a heat deposition of about 4 kW for low power targets and up to 15-20 kW for high power targets is possible. Therefore, to provide an efficient cooling a 6 mm thick heat shield is directly mounted on the water cooled target unit and is fixed on high voltage (HV) common potential. The diameter of the aperture in heat shield is 3.56 mm which is slightly larger than the inner diameter of the transfer tube, 3 mm.

The repeller electrode which is located 1.4 mm behind the heat shield has a large aperture of 5 mm diameter to avoid heating due to direct exposure to the heat radiation from the target and material deposition. The RFQ electrodes are 35 mm long and are mounted on a single piece copper bracket. The electrodes are electrically insulated from the copper mount by ceramic washers. This mount also holds an electrically insulated exit electrode with an aperture of 3.5 mm diameter. There are two different operation modes for IG-LIS: transmission mode, and suppression mode. Figure 6.8 presents both operation modes. Positive source potential in the transmission mode helps to extract more ions from the source towards the RFQ and extraction electrode.

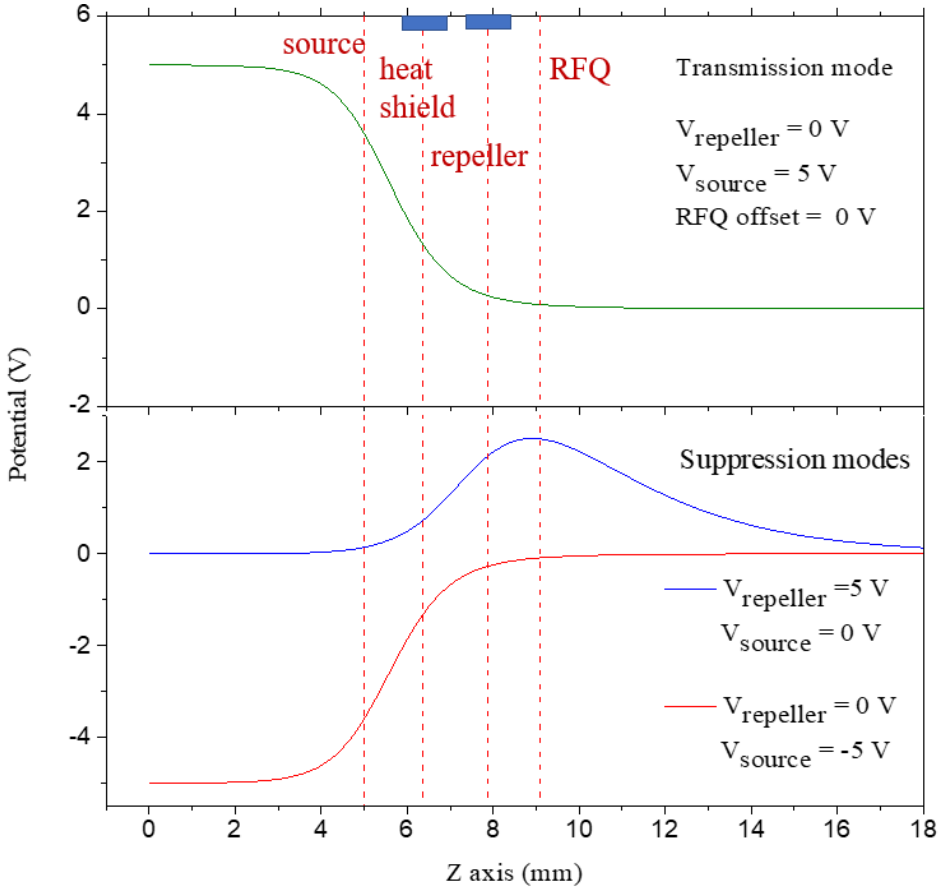

Figure 6.8: Potential array along the z-axis in IG-LIS for two operation modes: transmission and suppression mode. Vertical red dash lines represent the locations for source, heat shield, repeller electrode, and beginning of the 35mm long RFQ. $V_{repeller}$: potential on the repeller, V_{source}: potential on the source, RFQ-offset: dc potential offset of RFQ. The region from which ions can be extracted is larger in transmission mode and allows for an improved ion extraction from the source. The efficiency of the IG-LIS in transmission mode comes close to that achieved by the standard surface ion source - RILIS configuration. Source bias operation in suppression mode (red curve) compared to repeller operation (blue curve), covers a larger extraction region and has lower potential difference along the axis of cold ionization volume and therefore is now the preferred IG-LIS operation mode. Blue rectangles on the top axis represent the thickness of the electrode.

By applying a voltage higher than the source bias to the repeller electrode, mainly neutral atoms will be able to enter the ionization region where they can be ionized by resonant laser light while surface ionized species are repelled. For online operation, the capability to switch between the suppression and transmission modes is advantageous, since the high ion transmission of the latter provides intensive beams for beam tuning.

Potential arrays along the z-axis in IG-LIS for the two operation modes with the standard on-line operation parameters are shown in Figure 6.9.

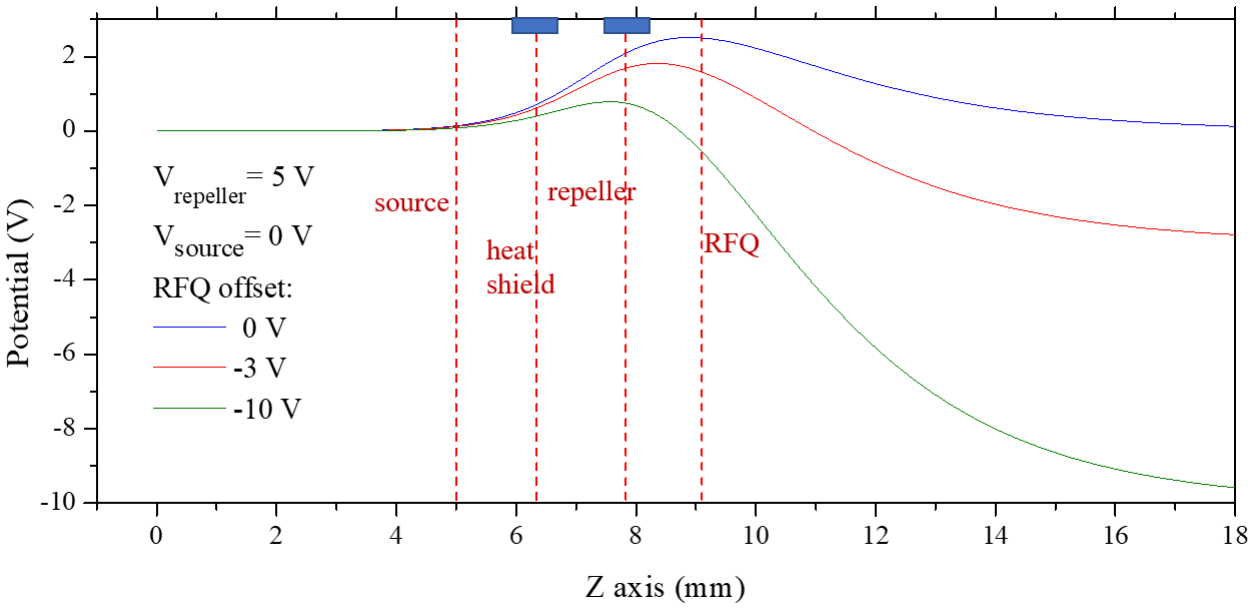

Figure 6.9: Potential array along the z-axis in IG-LIS. Red dash lines represent the locations of source exit, heat shield, repeller electrode, and start of the RFQ. $V_{repeller}$: potential on the repeller, V_{source}: potential on the source, RFQ-offset: dc potential offset of RFQ. Shifting down the potential on offset with respect to the repeller helps to extract more ions. Blue rectangles on the top axis represent the thickness of the electrode.

The RFQ-offset potential in Figure 6.9 helps to increase the kinetic energy of ions towards the RFQ and extraction electrode and consequently enhances the transmission efficiency (larger extraction region). However, the effect of this potential difference along the axis on the overall energy spread of the ions must be considered. The mass separator's mass resolution of $m/\delta m \sim 2000$ has such an effect that ions with an energy spread above ~ 10 eV will not be able to pass through the mass separator. Therefore the energy spread of ions extracted from the IG-LIS must be considered.

6.3.4 Energy spread

For on-line IG-LIS operation, the energy spread of the extracted beam should be below 10 eV in order to provide efficient transmission through the downstream mass separator. The resultant

simulation studies presented in this section are particularly useful for establishing high resolution, high throughput mass separator tuning parameters for radioactive isotope beams from IG-LIS.

Simulation results for the kinetic energy of the extracted beam as a function of RFQ-offset potential in IG-LIS for transmission and suppression mode are presented in Figure 6.10 and Figure 6.11, respectively.

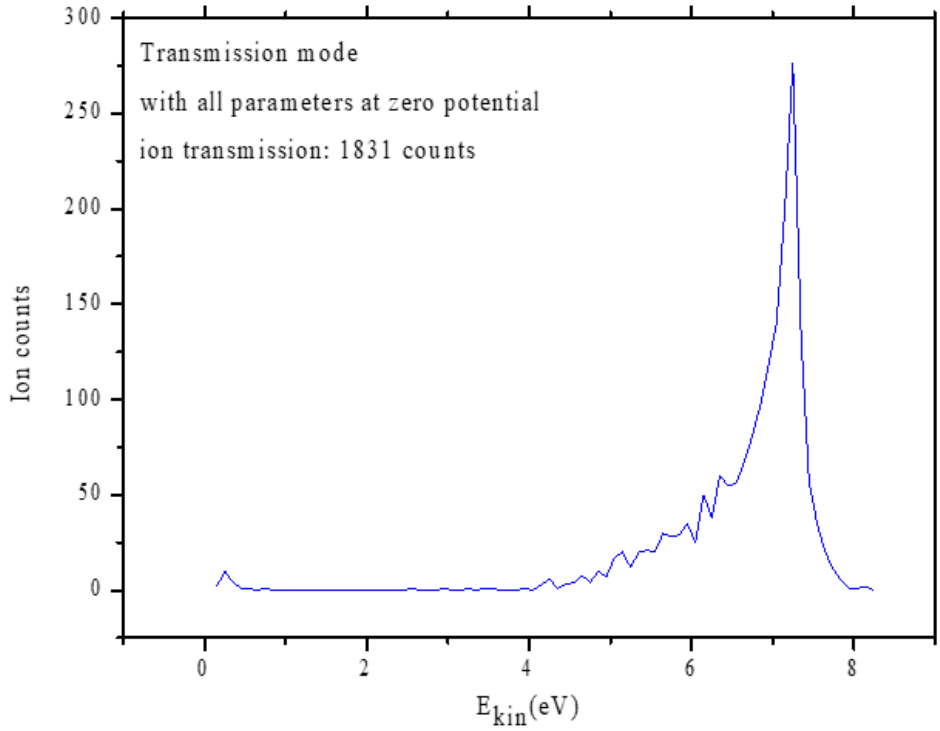

Figure 6.10: Kinetic energy of extracted ions in transmission mode with potentials on source, repeller, and RFQ-offset all set to zero volt. Simulation is performed for mass 200 amu.

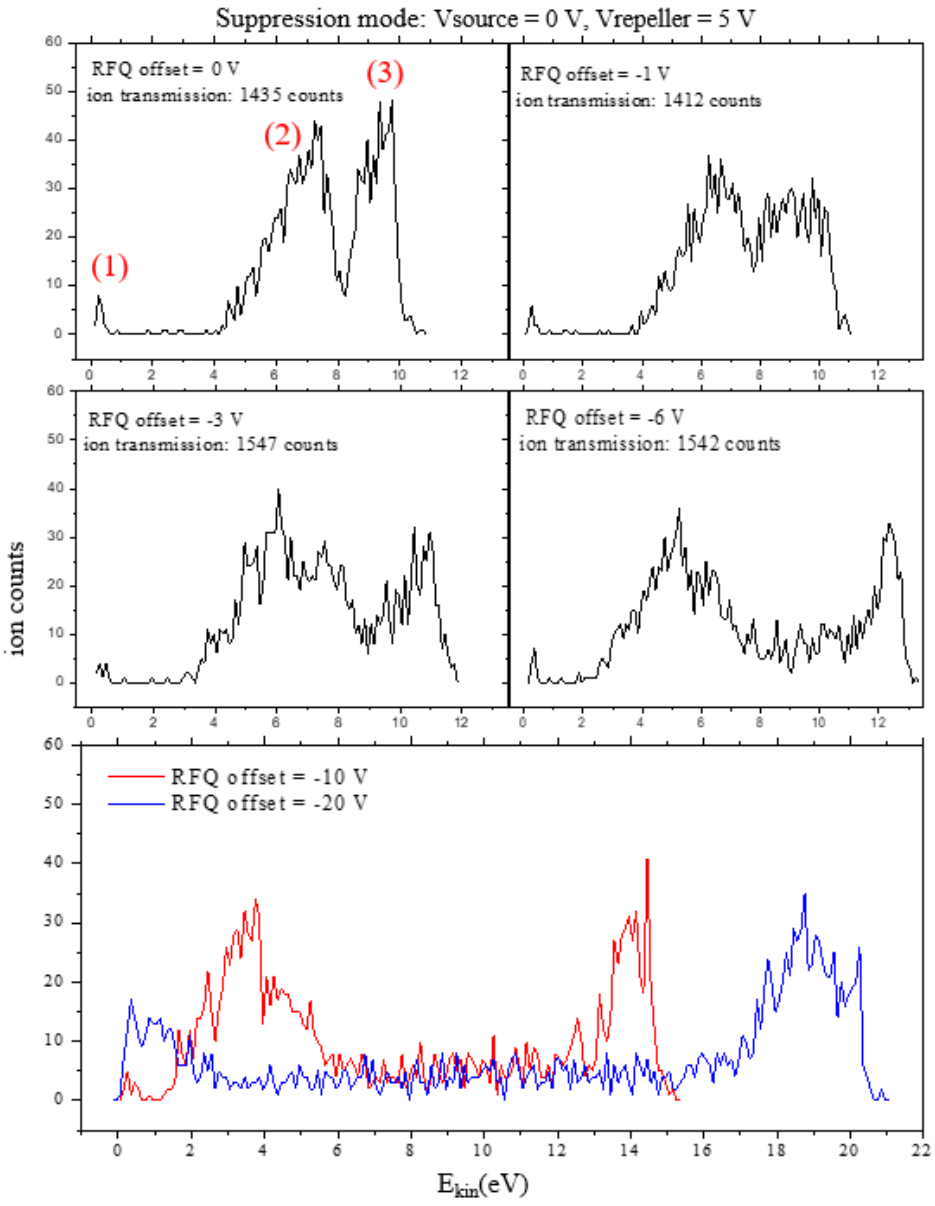

Figure 6.11: Kinetic energy of extracted ions in suppression mode. Simulations are performed for mass 200 amu. The three peaks in the graphs result from created ions right after repeller (last peak (3) in higher energy region), along quadrupole (the middle (2) peak), and at the end of quadrupole (first peak (1) spanned from 0 eV to less than 1 eV). Increasing the potential difference between RFQ-offset and repeller, moves the last two peaks away from each other till the middle peak overlaps with the first peak.

In suppression mode (Figure 6.9), enhancement of the beam transmission is reasonable by shifting down the RFQ-offset to some extent, since lowering the RFQ-offset with respect to the source causes a guiding electric field within the ionization region between the repeller and RFQ and therefore

more efficiently extract ions towards the extraction electrode. However, shifting the RFQ-offset results in a larger potential difference in the extraction region and consequently higher energy spread.

Figure 6.12 presents the effect of RFQ-offset on ion transmission and energy spread in suppression mode. This effect saturates at RFQ-offset = -3 V after which there is no further increase in transmission.

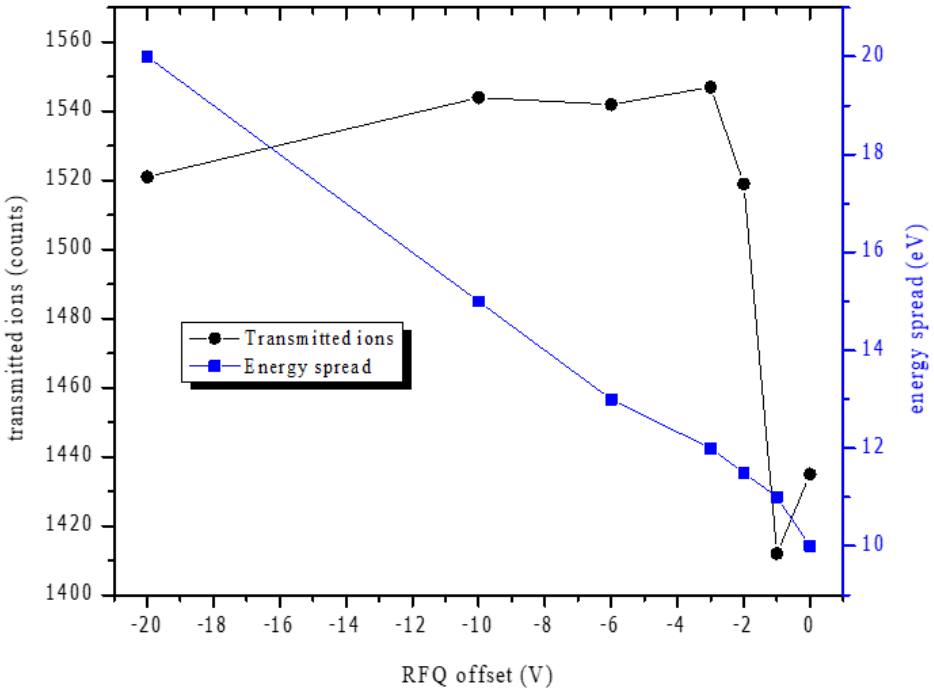

Figure 6.12: Effect of RFQ-offset on extracted ion's energy spread and transmission efficiency in suppression mode. Transmission efficiency saturates at RFQ-offset = -3 V, whilst providing minimal energy spread.

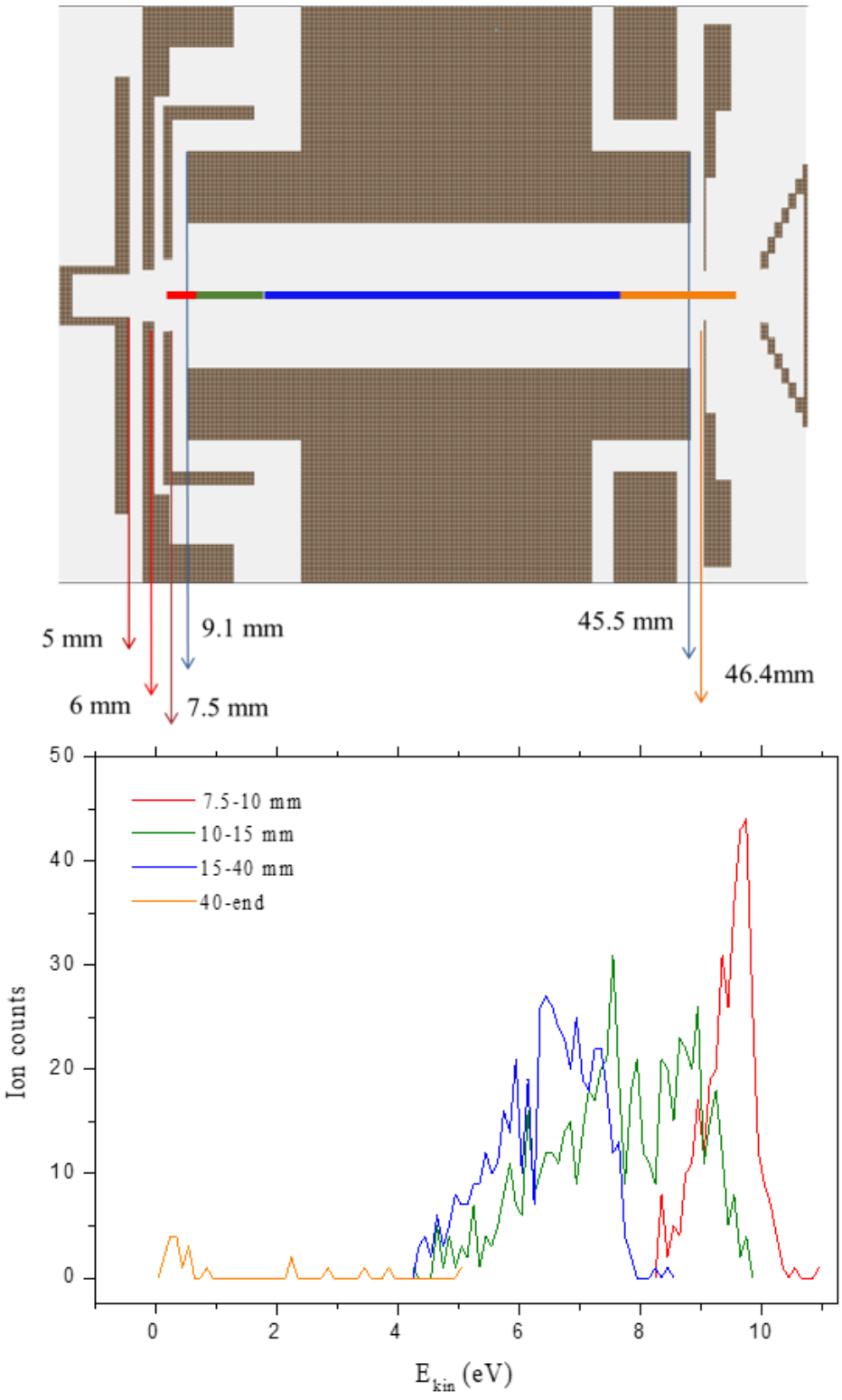

Figure 6.13: Kinetic energy of extracted ions, created in different parts of quadrupole. Neutrals are flown at the entrance of the source (z = 4.5 mm). Simulation is performed with suppression mode settings for mass 200 amu. V_{source} = 0 V, $V_{repeller}$ = 5 V, RFQ-offset = 0 V.

Alongside the understanding of the general RFQ performance, the simulation results presented in Figure 6.13 represent extracted ions resulting from ions created in different parts of quadrupole. Ions with lower kinetic energy are those created at the end of quadrupole, whereas those with highest energy are guided from the source.

For efficient beam transport at ISAC, the energy spread should not be higher than a few eV and the emittance should be in the range of few ten mm mrad. This effect will be even more pronounced for high resolution beam transport at ISAC. For that reason, simulation studies in the following sections will provide some alternative solutions to overcome energy spread issues and optimize the operating parameters of IG-LIS towards a more robust and higher efficiency system for on-line operation.

6.4 IG-LIS on-line measurements

The time profile structure was obtained during a radioactive gallium beam experiment in 2017 to test various operation parameters of IG-LIS. In this test, the effect of RFQ-offset potential (Figure 6.14) and RF-phase (φ), the entry phase angle of ions in RFQ (Figure 6.15) on transmission efficiency of ions, were observed.

Shifting the dc-offset potential down with respect to the repeller electrode results in enlarging the extraction region and correspondingly pushing more ions from the source towards the extraction electrode. However, the transmission efficiency drops at offset -4 V, since the energy spread at this potential gradient was increased and the magnet mass separator at ISAC can accept ions only with a few eV energy spread.

Improper RF-phase ϕ can deflect the ions entering to the RFQ and cause losses in transmission efficiency due to hitting ions to the rods. This effect can be observed from the measurements in Figure 6.15.

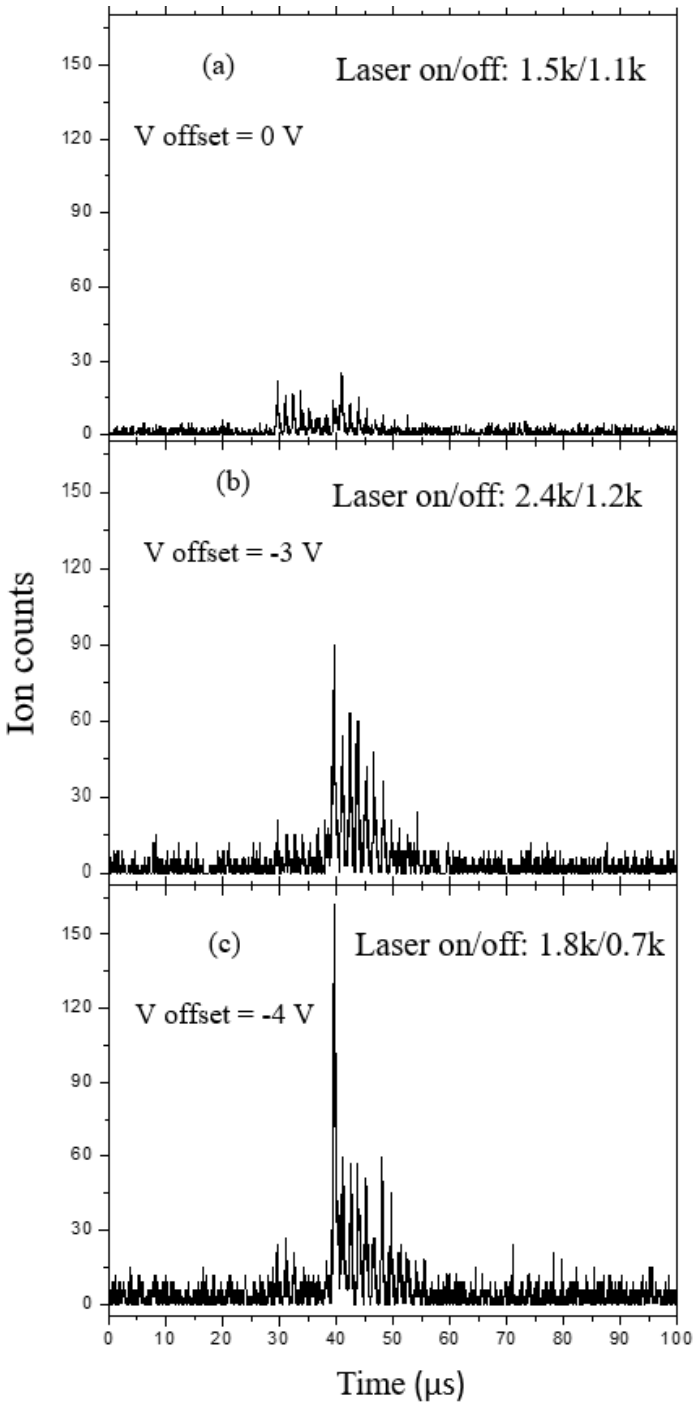

Figure 6.14: Effect of RFQ-offset potential on time profile structure of extracted ions. Three cases of RFQ-offset (a): 0 V, (b): -3 V, and (c): -4 V are the measurement results from IG-LIS for gallium in 2017. Shifting the RFQ-offset potential down with respect to the repeller electrode results in pushing more ions from source to extraction electrode. Due to a few eV acceptance of magnetic mass separator in ISAC, the transmission efficiency drops in offset -4 V while from simulations in Figure 6.12 one can see the enhancement of transmission efficiency and energy spread with lower RFQ-offset potential. Laser on/off: ion counts from CEM for laser on and laser off.

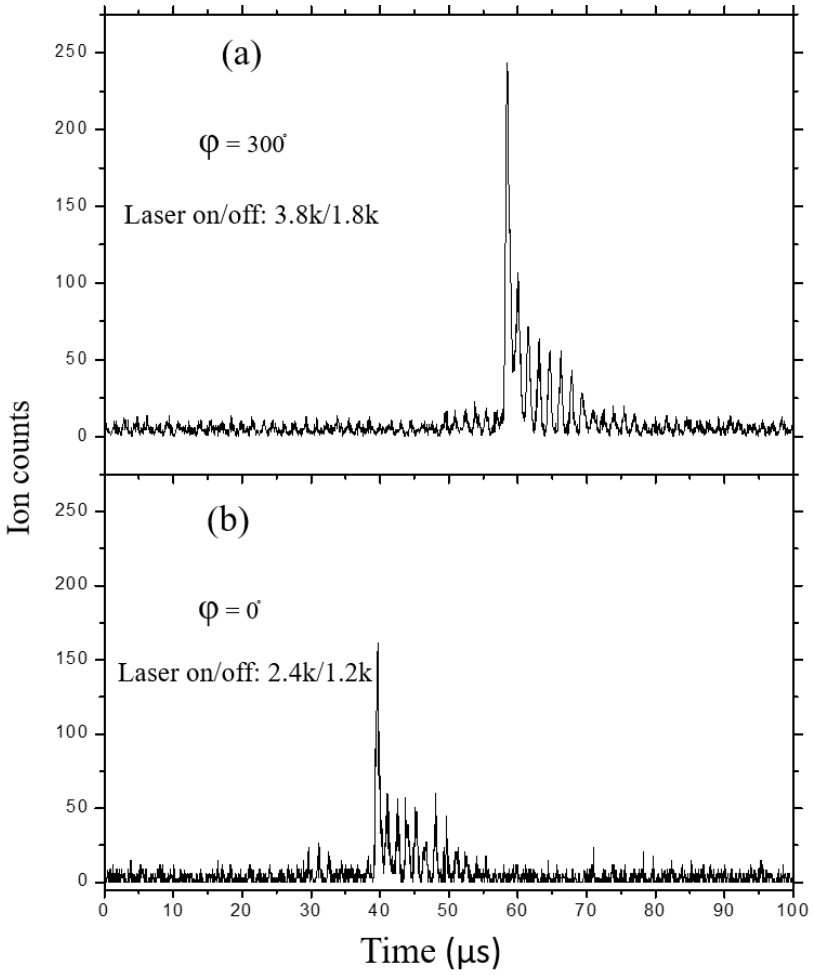

Figure 6.15: Effect of RF-phase (the entry phase angle of ion in RFQ) on transmission efficiency of ions. Two cases of (a): $\varphi = 300^o$, and (b): $\varphi = 0^o$ are the measurement results from IG-LIS for gallium in 2017. Laser on/off: ion counts from CEM for laser on and laser off.

6.5 Possible improvements

Simulation studies in this section provide possible improvements of energy spread and overall efficiency in the ion guide.

6.5.1 Effect of the laser parameters on the ion guide efficiency

Calculations in Figure 6.16 show the effect of the laser repetition rate on the transmission efficiency of extracted laser ionized species.

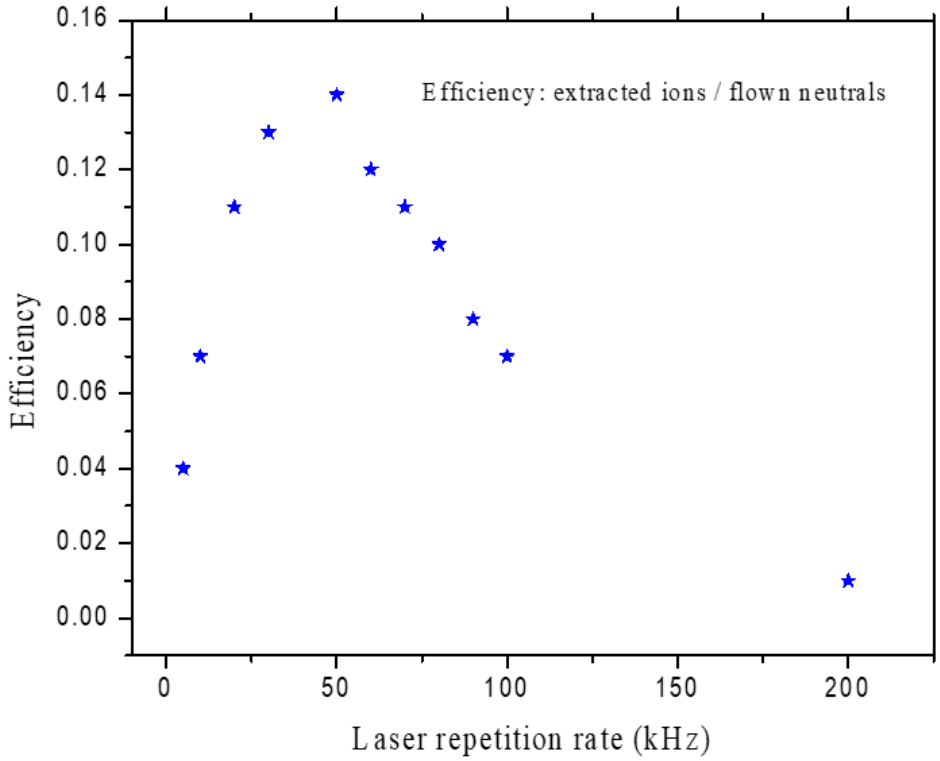

Figure 6.16: Calculated laser repetition rate effect on the extracted laser ionized species. Transmission efficiency reaches to an optimum point at repetition rate of 50 kHz. However, one should note that whether this maximum point is exactly at 50 kHz or not depends on the ionization efficiency of the laser scheme which is considered to be 100% for simulations in this work. An overall efficiency improvement of IG-LIS by a factor of 3× could be achieved with a laser repetition of 50 kHz.

An increased laser repetition rate helps to ionize more of the neutral atoms right after passing the repeller electrode, resulting in higher efficiency. Calculations are based on suppression mode operation and mass 200 amu.

The effect of the laser repetition rate on the energy spread is shown in Figure 6.17. Higher laser repetition rate results in ionizing more neutrals effusing into the ionization volume freely. With increasing duty cycle eventually the low energy tail in Figure 6.17 (red curve) can be suppressed and most of the ions are extracted with the same energy.

At repetition rates higher than 50 kHz in suppression mode, most of the neutral atoms are laser ionized before they pass the repeller and IG-LIS efficiency is reduced. Thus most of the laser ionized species will be rejected by repeller electrode and the efficiency drops down.

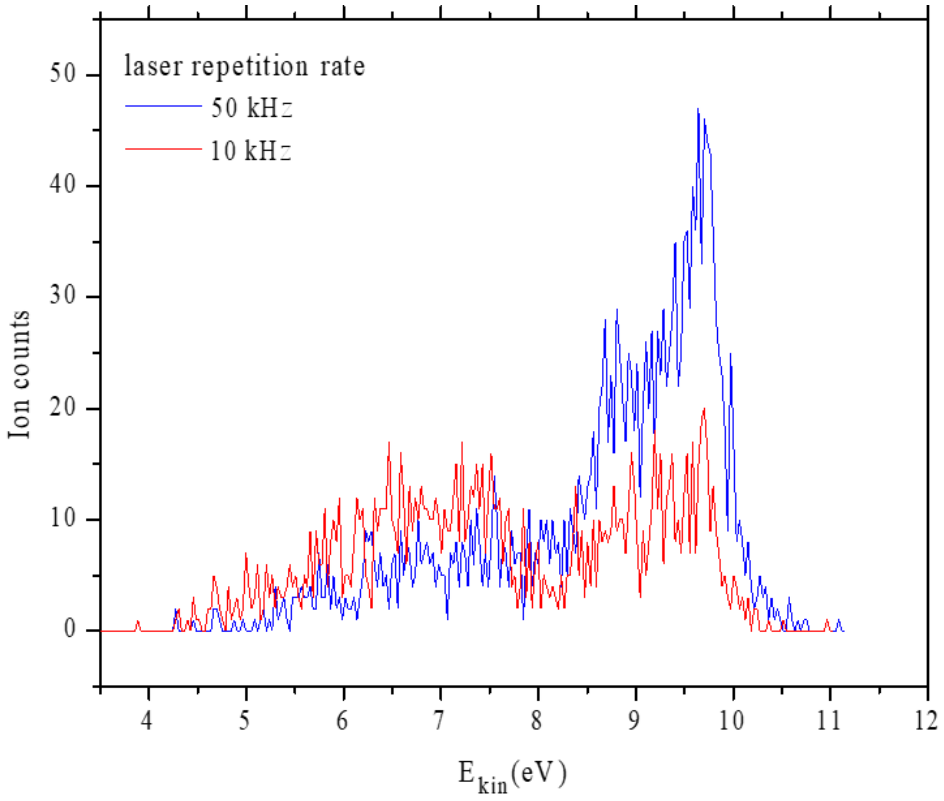

Figure 6.17: Effect of laser repetition rate on energy spread of the extracted laser ionized beam. Higher repetition rate to some extent increases the laser ions at suppression mode while the energy spread of the extracted beam reducing. Simulation is performed for mass 200 amu.

In order to verify this frequency dependence one would like to have constant laser pulse energy and be able to vary the pump laser repetition from 10 – 50 kHz. The available TRILIS pump laser [2] can only be switched at up to 20 kHz repetition rate. A 5 fold increase in repetition rate would also require the equivalent increase in pump power from currently a ~10 W/Ti:Sa laser to effectively 50 W/Ti:Sa laser. The optimized operating conditions at on-line ISOL type facilities are based on pulsed laser operation to make use of the high pulse peak power at repetition rates exceeding 10 kHz. In the standard hot cavity RILIS, atoms are confined in the approximately 40 mm long, 3 mm diameter transfer tube that acts as a quasi hot cavity, with a substantial residence time for atoms. This leads to ion yields of the hot cavity RILIS being optimal at ~ 10 kHz laser repetition rate.

[2] LEE LDP- 100MQG

6.5.2 Octupole ion guide

In an octupole RF guide concentration of the field near the field radius is more pronounced. The pseudopotential for the octupole field reads

$$U(r) = \frac{4eV_{RF}^2}{m\omega^2 r_0^2}\left(\frac{r^6}{r_0^6}\right). \tag{6.6}$$

The octupole field is usually approximated using eight cylindrical rods. The pseudopotential of Equation (6.6) (with the same mass to charge ratio and the same field amplitude and frequency) is four times larger at the octupole field radius of $r = r_0$ compared with the quadrupole ion guide of the same field radius and driving RF. Thus an octupole RF ion guide can transport a range of masses four times larger than the quadrupole ion guide of the same field radius and field parameters. Due to concentration of the field close to the field radius the amplitude of particle motion in an octupole guide is larger than in the quadrupole with similar field parameters. From the study of octupole potential distributions for several geometries, each with different rod to field radius ratios an optimum value of $r_{rod}/r_0 = 0.355$ was derived [127].

Unlike in a quadrupole field, octupole RF ion guides have no well-defined stability parameters relating the particle mass to charge ratio with the field parameters [123]. In fact, the x and y motions are coupled and cannot be considered independently. This means that stability of particle motion in octupole guides depends not only on the particle mass but also on the kinetic energy, which is especially noticeable at low mass to charge ratios. However, this will not be an issue for an ion guide operation at ISAC, since the ions have an initial energy of less than 1 eV.

Study of energy spread in octupole ion guide

The kinetic energies of ions are modulated much more strongly by the quadrupole RF field than higher multipoles RF field. The ion beam from the ion source has an intrinsic energy, position, and angular spread (phase space in mm.mrad or emittance), any defect in the primary beam would affect

beam resolution significantly, due to compression and distortion by the multi-keV axial acceleration and focusing abberations prior to inserting into the magnet mass separator system. The kinetic energy of extracted ions, resulting from ions created in different parts of octupole is simulated in Figure 6.18.

Ions with lower kinetic energy are those where created at the end of octupole, while those with highest energy are guided from the source. In all these simulations for octupole and quadrupole ion guide the field radius is the same (r_0 = 5 mm) and the radius of the poles in octupoles is considered based on the optimum ratio of r_{rod}/r_0 = 0.355 (r_{rod} = 1.78 mm). Simulations for both geometries were based on optimized operational parameters of RF ion guide (V_{RF} = 20 V (peak to peak), f = 0.7 MHz for octupole and V_{RF} = 35 V, f = 0.7 MHz for quadrupole at mass 200 amu).

Comparing kinetic energy of ions created and guided in an octupole (Figure 6.18) with the ones created and guided through a quadrupole (Figure 6.13), one can see that most of the ions created in an octupole (blue and green graphs) experience comparable kinetic energies.

The transverse kinetic energy of an ion propagating inside a linear RF ion guide does not stay constant. It varies rapidly following the ion's rapid micro-motion and the slower macro-motion in the RF field in the radial plane. For higher order multipoles, the RF field in the center is much weaker, and the micro-motion is less pronounced near the axis. To understand this behavior better, the DC-equipotential lines for both quadrupole and octupole is shown in Figure 6.19.

For a better acceptance and resolution at mass separator magnet (ISAC at TRIUMF) with $\delta E \sim 1$ eV, more ions can be extracted from an octupole ion guide.

Octupole versus quadrupole ion guide

The results from simulation studies shown in Figure 6.20(a) indicates that the energy spread from ionization within a quadrupole ion guide configuration only allows to extract a maximum 28% of ions at the magnet mass separator with an energy acceptance of ~ 1 eV. Upgrading to an octupole ion guide, Figure 6.20(b), would increase the efficiency to 50% with the same 1 eV energy spread.

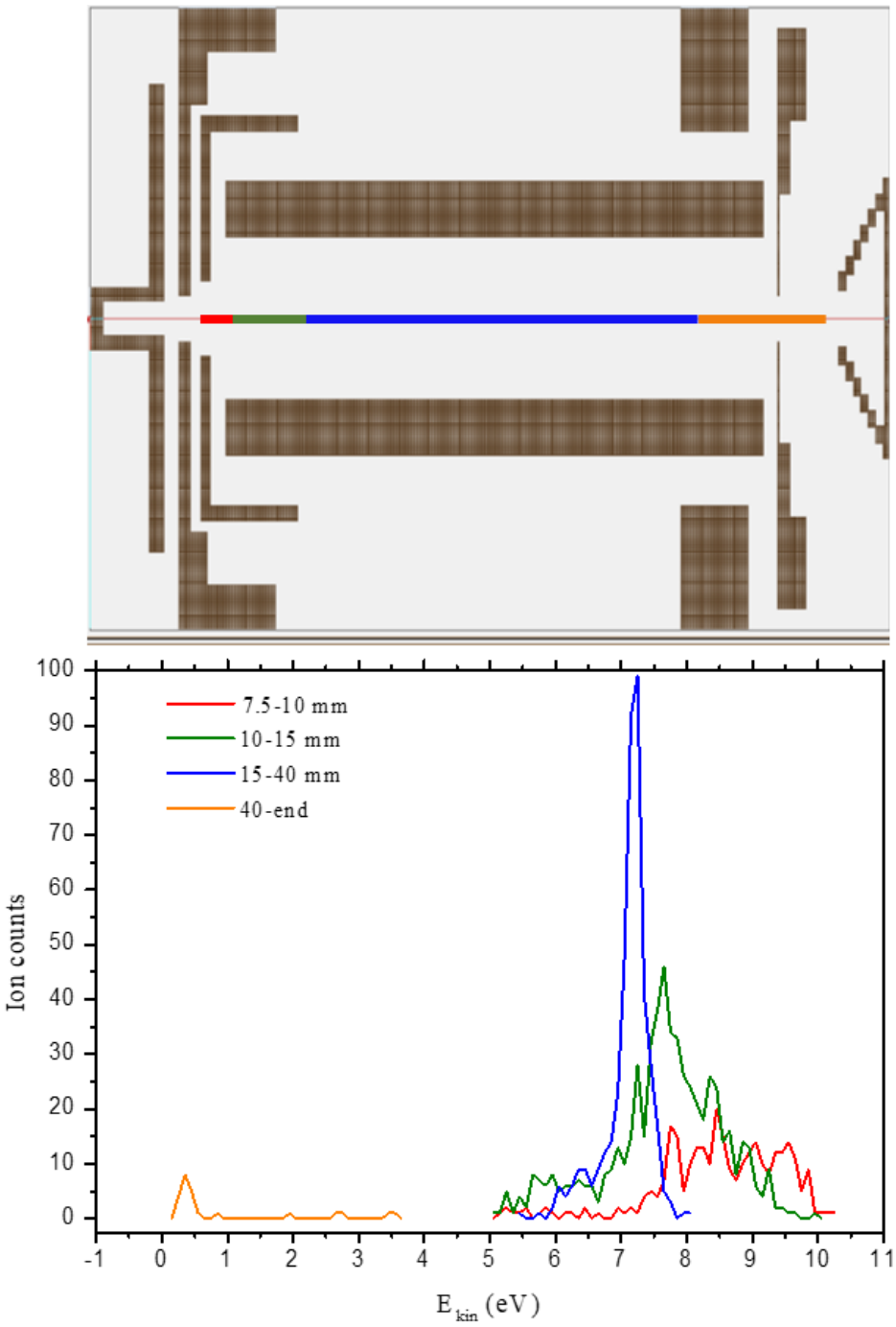

Figure 6.18: Kinetic energy of extracted ions, created in different parts of the octupole. Simulations are for suppression mode ($V_{repeller}$ = 5 V, V_{source} = 0 V , and RFQ-offset = 0 V) and mass 200 amu.

An alternative method to suppress surface ions is to bias the source instead of applying a potential on the repeller electrode. Utilizing a source bias setup results in a reduced ion energy spread over

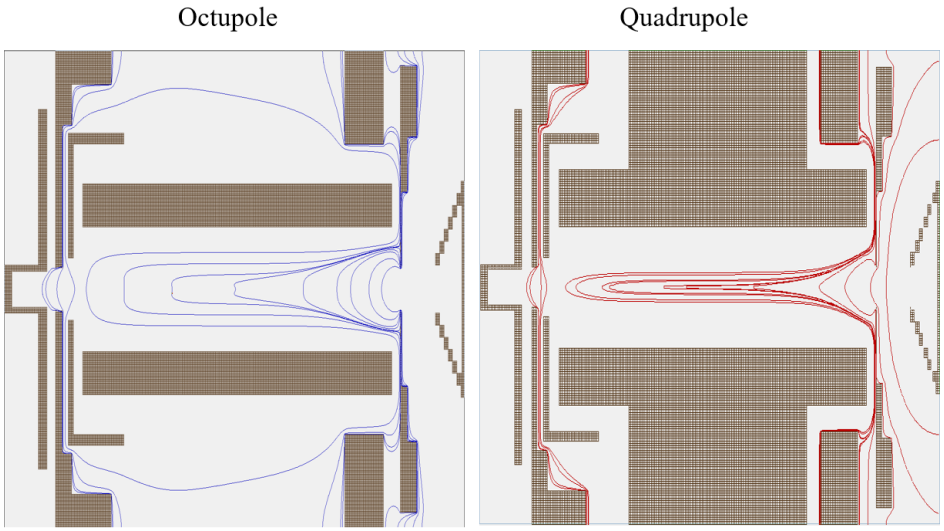

Figure 6.19: The equi-potential lines for octupole and quadrupole. For higher multipoles, the RF field in the center is much weaker compared to that of the equivalent quadrupole and the micro-motion is less obvious near the axis.

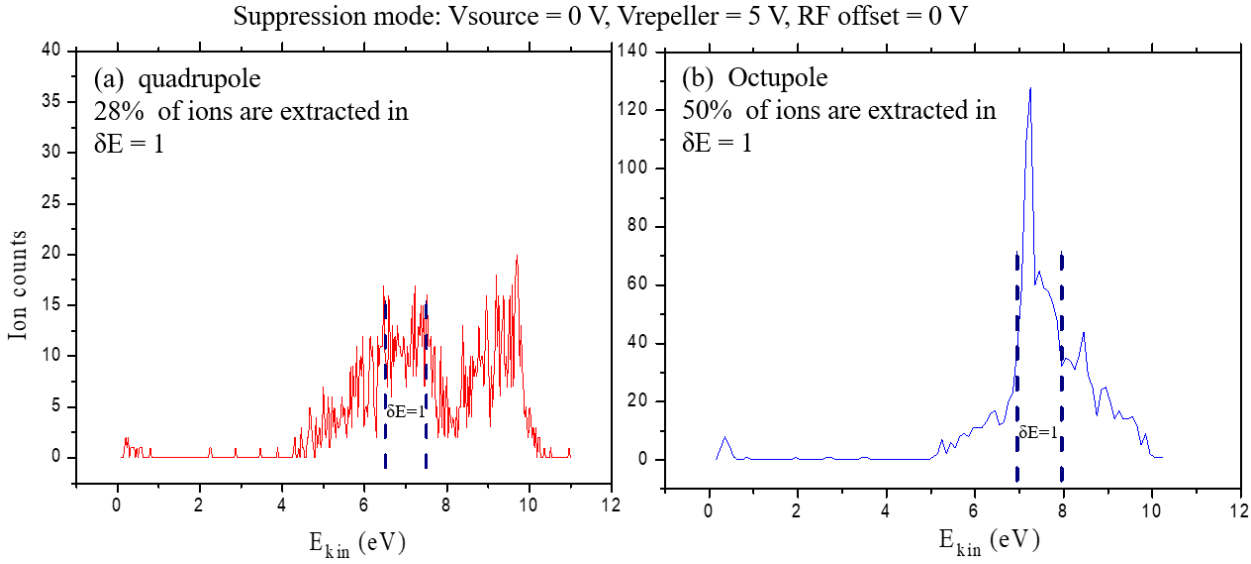

Figure 6.20: Simulation studies for kinetic energy of extracted ions in suppression mode from (a) a quadrupole ion guide and (b) an octupole ion guide. Dashed lines represent the δE = 1 eV region for extracted ions from an ion guide. Due to the weaker RF field at the center of an octupole, more of the ions are extracted in the same energy regions. Simulations are performed for mass 200 amu.

1 eV compared to suppression by means of the repeller electrode for both quardupole and octupole ion guides (Figure 6.21). It allows for a more efficient collection of ions at the mass separator.

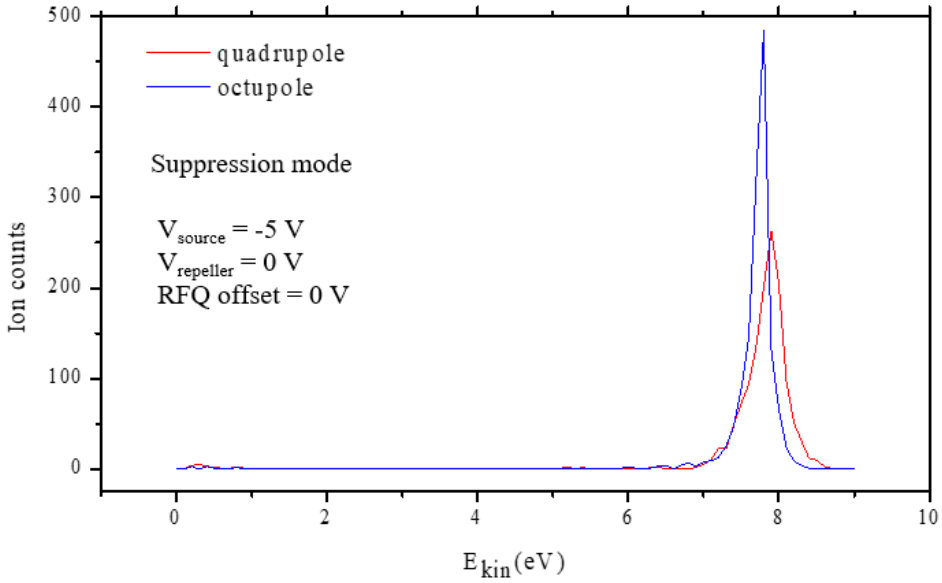

Figure 6.21: Simulation studies for kinetic energy of extracted ions in suppression mode with source bias setup from a quadrupole ion guide (red curve) and an octupole ion guide (blue curve). The peak point in blue curve shows the extraction of most of the ions in the same energy region in an octupole ion guide. Simulations are performed for mass 200 amu.

6.6 Conclusion

Operating the IG-LIS (repeller potential, source-offset, RFQ-offset, RF-amplitude and frequency) with proper settings is critical in order to optimize the system performance. Low energy spread becomes important when coupling IG-LIS to the future CANREB (Canadian rare isotope facility with electron beam ion source) isobar separator or when providing beams for collinear fast beam laser spectroscopy, or when injecting beams into ion traps. In suppression mode, operating IG-LIS with source biased in a lower potential can significantly decrease the energy spread compared to the operation mode using a repeller. Modifying the IG-LIS quadrupole ion guide to an octupole results in a net reduction of energy spread. Increasing laser repetition rate from 10 kHz to 50 kHz can enhance the IG-LIS efficiency while significantly reducing the energy spread of extracted laser ions.

Part IV

Laser resonance ionization spectroscopy of lanthanides

7 | Laser spectroscopy of thulium

In this chapter the results of the laser spectroscopy on thulium (Tm) are presented. The first section summarizes the properties of Tm and the motivation for the development of Tm ion beams at ISAC. The stages that were required to identify an efficient multi-step RIS scheme for Tm are described in the second section followed by an overview of the experimental setup. A combined analysis of the convergence limits resulting from odd parity Rydberg series and AI Rydberg series yielded a consistent value for the IP of Tm which is one order of magnitude more accurate than the previous record. The result of this spectroscopy is aimed to be submitted in *Spectrochimica. Acta. B.* journal [24]. The last section provides the yield measurement results for radioactive isotopes of thulium at ISAC in 2018, with the Tm ionization scheme developed as part of this thesis.

7.1 Properties and history of thulium

Due to the influences of $4f$ shell electrons in rare-earth elements, the configuration interaction of the atomic states becomes more complex than in other elements. Neutral thulium is one relatively simple case because of its nearly closed $4f$ shell with the ground state configuration of $4f^{13}6s^2$. At high-lying energy levels, the structure begins to exhibit a complex character resulting from excitation of an electron from the $4f$ into the $5d$ shell, or the excitation of a $6s$ electron into the $6p$ shell. The resulting overlapping configurations of even parity, $4f^{12}5d6s^2$ and $4f^{13}6s6p$, are heavily mixed and form a dense complex structure of lines.

In 1971, Camus [128] observed the absorption spectrum of thulium vapor in the region from 200 to 275 nm. He determined the value for the ionization energy by fitting the $4f^{13}(^2F^o_{7/2})6s(7/2,1/2)^o_3np_{3/2}$ series ($17 \leq n \leq 48$). In 1973, J. Sugar *et al*. [129] started spectroscopic studies of Tm resulting in more complete energy level tables of the Tm atom including mainly bound low-lying atomic states energies listed in [128]. In 1980's the range of investigated Tm atomic states was expanded towards states with higher as well as lower values of the principal quantum number [130–132]. Optimal three-step ionization scheme to an autoionization state was developed by Atakhodzhaev and Fedoseev in 1985 [133]. Even parity Rydberg states (RS) and AI Tm states were investigated by Vidolova-Angelova in 1987 [131]. These investigations of three-step excitation schemes used state of the art dye laser systems. The investigated excitation schemes were 597.2 nm + 646.2 nm + λ_3 $\rightarrow$ RS and 563.3 nm + 617.0 nm + λ_3 $\rightarrow$ AI. These laser schemes unfortunately are not suitable for Ti:Sa laser based RILIS systems as all the steps are outside the tuning range of Ti:Sa lasers. Therefore, laser resonance ionization spectroscopy of thulium using Ti:Sa lasers at TRIUMF's off-line laser ion source test stand was performed. The subject of our two-step laser ionization investigation are the odd parity Rydberg states and AI Rydberg states located in an energy range in the vicinity of the first and the second (49879.8 cm^{-1} and 50116.8 cm^{-1}) ionization limits [128]. Blue-blue laser excitation schemes are very attractive, due to the simply setup and high conversion efficiency of interactivity frequency-doubling of Ti:Sa lasers [16]. Due to the very narrow spacing of these ionization limits, the density of states are extremely high. Converging to different ionization limits, a multitude of AI Rydberg series mix to each other. Different two-step resonant ionization schemes have been investigated by means of resonant ionization spectroscopy. The spectroscopic results are presented and evaluated. The measurements resulted in new atomic data for Tm, including new Rydberg and autoionizing Rydberg series and a more precise value of the first and second ionization limit for Tm. The ionization efficiencies via the strongest one of the AI transitions from two different schemes were compared, and an optimal Ti:Sa laser based resonance ionization scheme suitable for the delivery of radioactive Tm beams was identified and used for RIB delivery.

7.2 Ionization scheme development for thulium

The development of an efficient ionization scheme for thulium in the wavelength regime of solid state laser systems (Ti:Sa) was triggered by the experiment proposal S1756 [134]. In this proposal mass measurement of N = 82 lanthanide isotopes around Z = 70 (lutetium, ytterbium, and thulium) was proposed in order to study the evolution of neutron-deficient shell closure along the rare-earth elements.

For laser ionization scheme development and ion source tests, an off-line test stand was built in parallel to the on-line laser ion source operation, in order to service nuclear physics experiments [135], and various elements have been studied using RIS at LIS STAND [50, 136–139].

Ground state transitions

Two-step resonant ionization schemes for Tm with Ti:Sa laser based RILIS were investigated. Three different transitions of 371.897 nm, 409.533 nm, and 297.408 nm from the $4f^{13}(^2F^o)6s^2$ (J = 7/2) ground state to the first excited states of $4f^{12}(^3H_5)5d_{5/2}6s^2$ (J = 9/2), $4f^{13}(^2F^o_{7/2})6s6p(^1P^o_1)$ (J = 5/2), and $4f^{12}(^3F_2)5d_{5/2}6s^2$ (J = 7/2), respectively, were used [1]. Spectroscopic investigation was necessary to identify efficient atomic transitions for resonant ionization in the second step:

A: $4f^{13}(^2F^o)6s^2 \xrightarrow{409.533\,nm} 4f^{13}(^2F^o_{7/2})6s6p(^1P^o_1) \xrightarrow{blue\ scan} ?$

B: $4f^{13}(^2F^o)6s^2 \xrightarrow{371.897\,nm} 4f^{12}(^3H_5)5d_{5/2}6s^2 \xrightarrow{blue\ scan} ?$

C: $4f^{13}(^2F^o)6s^2 \xrightarrow{297.408\,nm} 4f^{12}(^3F_2)5d_{5/2}6s^2 \xrightarrow{blue\ scan} ?$

Intermediate level energies in these schemes have been taken from the NIST database [26]. A schematic diagram of the two-step excitation schemes investigated for Tm is shown in Figure 7.1.

[1] all the wavelengths recorded in this thesis are vacuum wavelengths

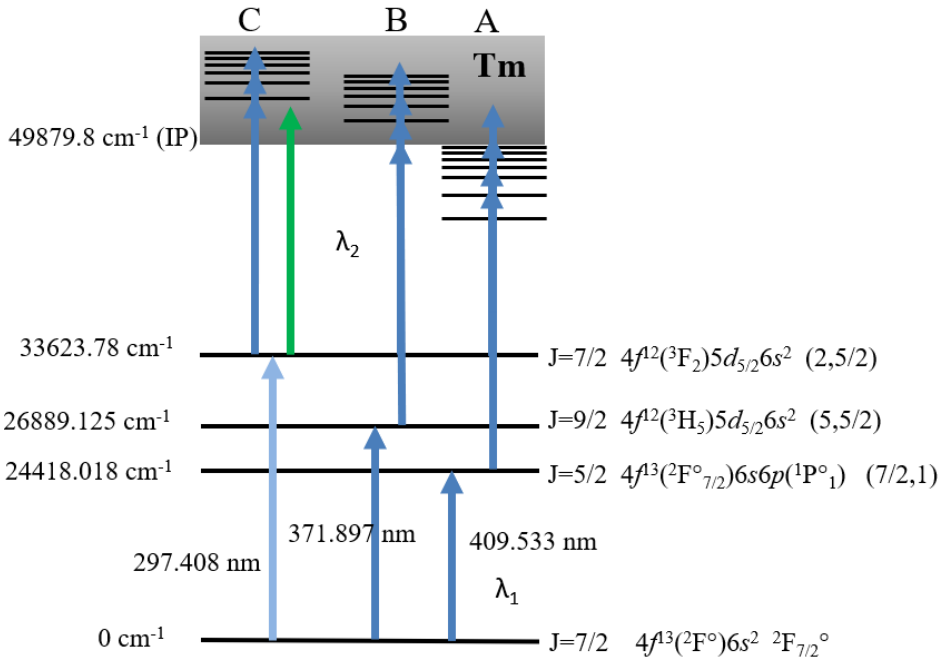

Figure 7.1: Schematic diagram of the two-step excitation schemes investigated for Tm, showing the Rydberg and AI resonances excited via different intermediate levels. Green arrow shows the non-resonant ionization which was applied to compare the ionization efficiency to new found resonant ionization schemes.

7.3 Experimental setup

Resonant ionization of Tm at TRIUMF's off-line laser ion source test stand has been obtained using multiple Ti:Sa lasers simultaneously pumped by a 30 W power, 10 kHz repetition rate, and 160 ns pulse width frequency doubled Nd:YAG laser. The experimental setup is shown in Figure 8.2. Two Ti:Sa lasers were employed in this experiment, one external cavity frequency doubled grating-tuned and one intra-cavity frequency doubled birefringent-filter-tuned (BRF-tuned). During scans, the phase matching conditions for frequency doubling of the grating-tuned laser were auto-tracked. The laser walk-off generated in the frequency doubling process was corrected by employing a commercial TEM Beam-Lock system. A typical scan speed was ~ 5 GHz/s. The TRILIS Ti:Sa lasers have typically output powers of 1-2.5 W in fundamental wavelengths (690-990 nm) with linewidth in the range of 1-10 GHz dependent on the pump power and wavelength. The grating-

tuned laser power was operated with self-seeding using a partial reflecting mirror (48% reflectivity) inside the cavity to enhance output power and avoid grating damage at high pump powers [69, 73].

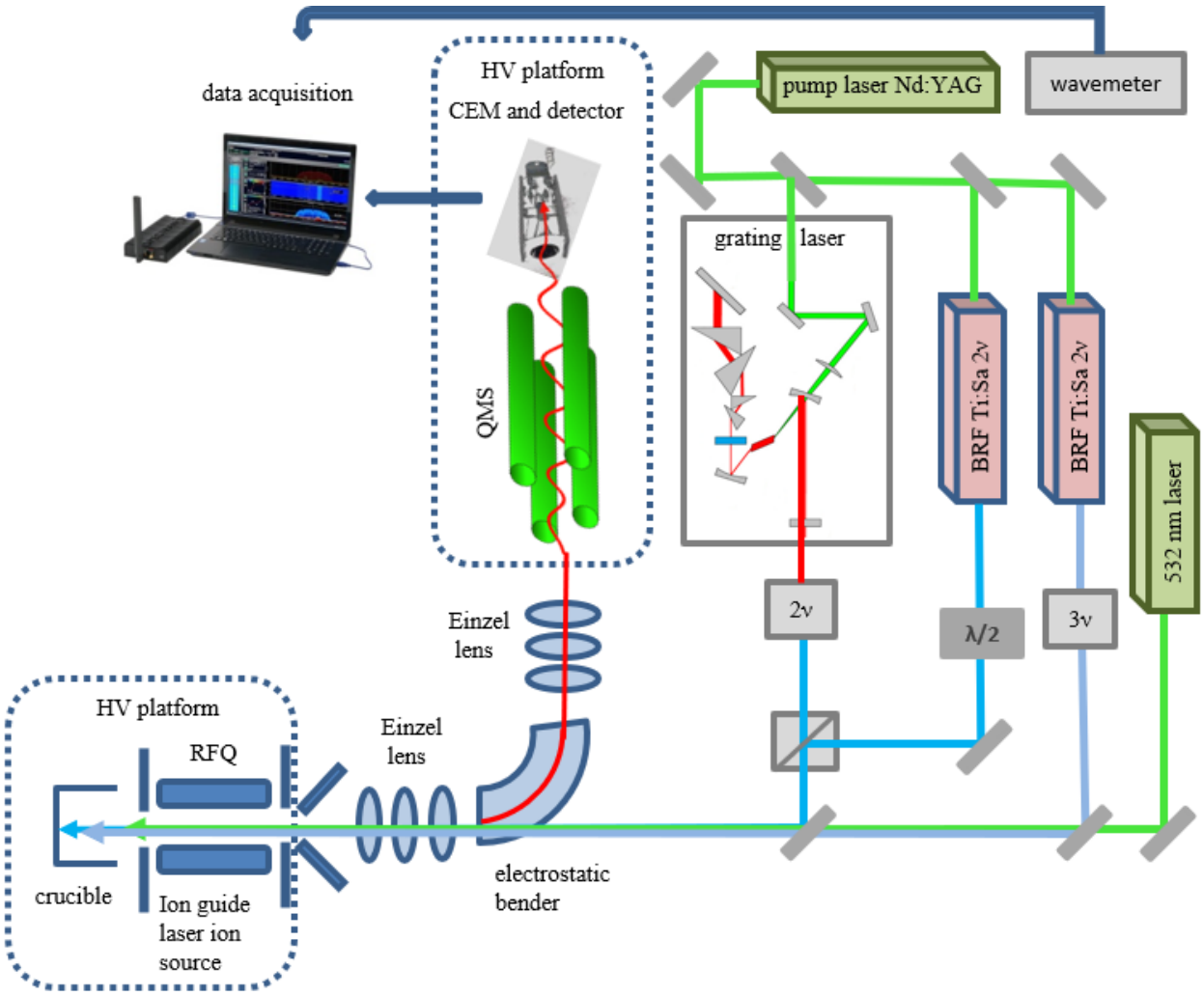

Figure 7.2: Schematic experimental setup for thulium laser ionization spectroscopy at TRIUMF's off-line laser ion source test stand.

For the first excitation step light, a BRF-tuned laser was frequency doubled via a nonlinear BBO crystal and the Rydberg or autoionization spectrum was observed via the variation of the ionization signal with the second excitation step laser frequency which is tuned automatically. Spatial overlap of two laser beams was achieved by polarization beam splitters. After being expanded 3-4 times by two telescopes, the light from both Ti:Sa lasers can be focused into the 3 mm diameter ionizer tube located in the vacuum system about 5 m away. To visualize the images of the two lasers inside the ionizer, a CCD camera is installed to observe the low power reflexes from the uncoated fused

silica window at the entrance to the vacuum chamber. The timing of laser pulses is monitored on a 4-channel oscilloscope [2] by detecting the laser pulse signals via fiber-coupled fast photodiodes [3]. To temporally synchronize laser pulses, the grating-tuned Ti:Sa laser was Q-switched by an intra-cavity Pockels cell. The Pockels cells of the Ti:Sa lasers are externally triggered. The trigger signals are delayed [4], according to the varying build up time of the Ti:Sa laser pulses, to provide the most efficient temporal overlap of the two pulses. In the initial setup, both spatial and temporal overlapping of the lasers were carefully adjusted by maximizing the ion signal for each ionization scheme. Temporal overlap of the two laser pulses was adjusted manually.

To investigate non-resonant ionization schemes, a 10 kHz repetition rate frequency doubled Nd:YVO_4 [5] laser is employed with an optical output of ~6 W and ~30 ns pulse length.

In the vacuum chamber at a residual pressure of below $\sim 10^{-6}$ Torr, an atomic beam is produced by thermal evaporation of 50 μg Tm which was loaded as a standard solution (1 g/l) [6] on a Ti foil, dried and then inserted into the crucible. The vaporized Tm atoms after interaction with laser radiation are resonantly excited to an autoionization state. The generated Tm ions are guided through an ion guide laser ion source (IG-LIS) [103, 104] and then extracted and accelerated to 10 keV. After electrical focusing and deceleration, they are mass analyzed in a quadrupole mass spectrometer and detected by an electron multiplier. A detailed description of the LIS STAND is given in [135].

7.4 Spectroscopy results

By scanning second laser wavelength, a series of odd parity high-lying Rydberg levels converging to the IP $4f^{13}(^2F^o_{7/2})6s_{1/2}(7/2,1/2)^o_4$ (49879.8 cm^{-1} [128]) from scheme A as well as a series of odd parity AI states converging to the second ionization limit $4f^{13}(^2F^o_{7/2})6s_{1/2}(7/2,1/2)^o_3$ from scheme B were observed. The AI resonances resulting from scheme C are significantly weaker

[2] Tektronic DPO3014
[3] Thorlabs DET10
[4] BNC 575
[5] Spectra Physics Navigator II-532-8
[6] Alfa Aesar spectra pure ($1 \mu g/\mu l$)

than the ones from schemes A and B which might be due to the lower transition probability of first excitation step (FES) in scheme C.

7.4.1 Odd-parity Rydberg states via scheme A

The FES (409.418 nm) in scheme A with transition probability of $A_{ki} = 9.8 \times 10^7\ s^{-1}$ was chosen to search for resonant Rydberg levels.

The second step excitation laser frequency in the case of this scheme was provided by a grating-tuned Ti:Sa laser which allowed to record the spectrum in the range 49418 - 52429 cm^{-1}. This range in the Tm spectrum covers a number of high lying Rydberg levels below the IP as well as AI levels. Most of the lines are assigned to be odd-parity Rydberg series converging to the IP of thulium. Several measurements with different speed, scan direction and target temperature were carried out over the same region of wavelengths to obtain the Rydberg series. The resonance centroids are determined by fitting the resonance lines with Gaussian profile. The statistical error is estimated to be 0.15 cm^{-1} by scanning the same resonance multiple time in different days.

In particular, the non-Coulombic properties of the Rydberg states are non vanishing even at large values of principal quantum number n of the Rydberg electron. One of the basic methods of multichannel quantum defect theory (MQDT) [34, 140, 141] is to construct the Fano-Lu plots [39], which can be extended to the potentials with general non-Coulomb asymptotes by considering only the law linking the energies and asymptotic phases to the quantum numbers. This provides an efficient method for the analysis of atomic or molecular spectra close to dissociation limit.

By plotting the observed states in a Fano-Lu plot, a Rydberg series was distinguished converging to the IP. The possible configuration is $4f^{13}(^2F^o_{7/2})6s_{1/2}(7/2, 1/2)^o_4\ ns_{1/2}$, $nd_{3/2}$, or $nd_{5/2}$.

The convergence limit of the Rydberg series is extracted by fitting their energy levels to the Rydberg-Ritz formula (Section 2.4)

$$E_n = E_{limit} - \frac{R_{Tm}}{(n - \delta(n))^2} \tag{7.1}$$

$$\delta(n) = \delta_0 + \frac{a}{(n - \delta_0)^2}, \tag{7.2}$$

where E_n is the energy of the Rydberg level with principal quantum number n, E_{limit} is the convergence limit, $R_{Tm} = 109736.959\,\mathrm{cm}^{-1}$, is the mass-reduced Rydberg constant for ^{169}Tm, $\delta(n)$ is the quantum defect given by the Ritz expansion to the second order, δ_0 is the asymptotic limiting quantum defect, and a is a constant.

Figure 7.3 presents the Rydberg-Ritz fit for the Rydberg series converging to the IP of Tm atom and the corresponding residuals between the experimental data and the fitted values. The Rydberg-Ritz fit for the observed levels gives the convergence limit $E_{limit} = 49880.53(4)\,\mathrm{cm}^{-1}$.

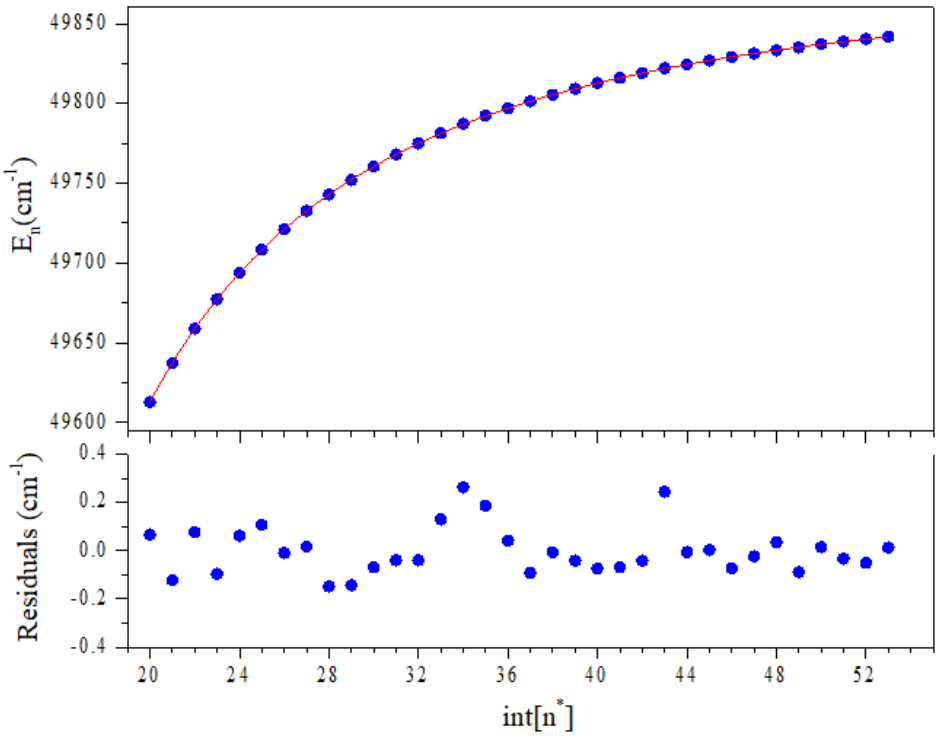

Figure 7.3: Rydberg-Ritz fit for odd parity Rydberg series converging to IP of Tm I. Fitting residuals are shown in the bottom subplot. The x-axis int[n^*] is the integer part of the effective quantum number n^*.

Accurate measurements reveals an energy dependence of the quantum defects, which is conveniently parameterized with a modified Rydberg-Ritz expression (Eq. 7.2).

7.4.2 Odd-parity AI Rydberg states via scheme B

In scheme B (Section 7.2), the strongest transition from the ground state to $4f^{12}(^3H_5)5d_{5/2}6s^2$ (J = 9/2) 26889.125 cm^{-1} with A_{ki} = 1.44 × 10^8 s^{-1}, was chosen from NIST database [26]. Starting from this intermediate state, the second excitation step was scanned across the accessible second harmonic wavelength range of 440 nm - 365 nm, using the Ti:Sa grating-tuned laser to obtain AI Rydberg series converging to the excited core state of $4f^{13}(^2F^o_{7/2})6s_{1/2}(7/2,1/2)^o_3$ which is located at ~ 237 cm^{-1} above the IP [142]. The recorded spectrum covers the energy range of 49620 to 54200 cm^{-1}. AI Rydberg states of Tm is presented in Figure 7.4 as part of this spectrum.

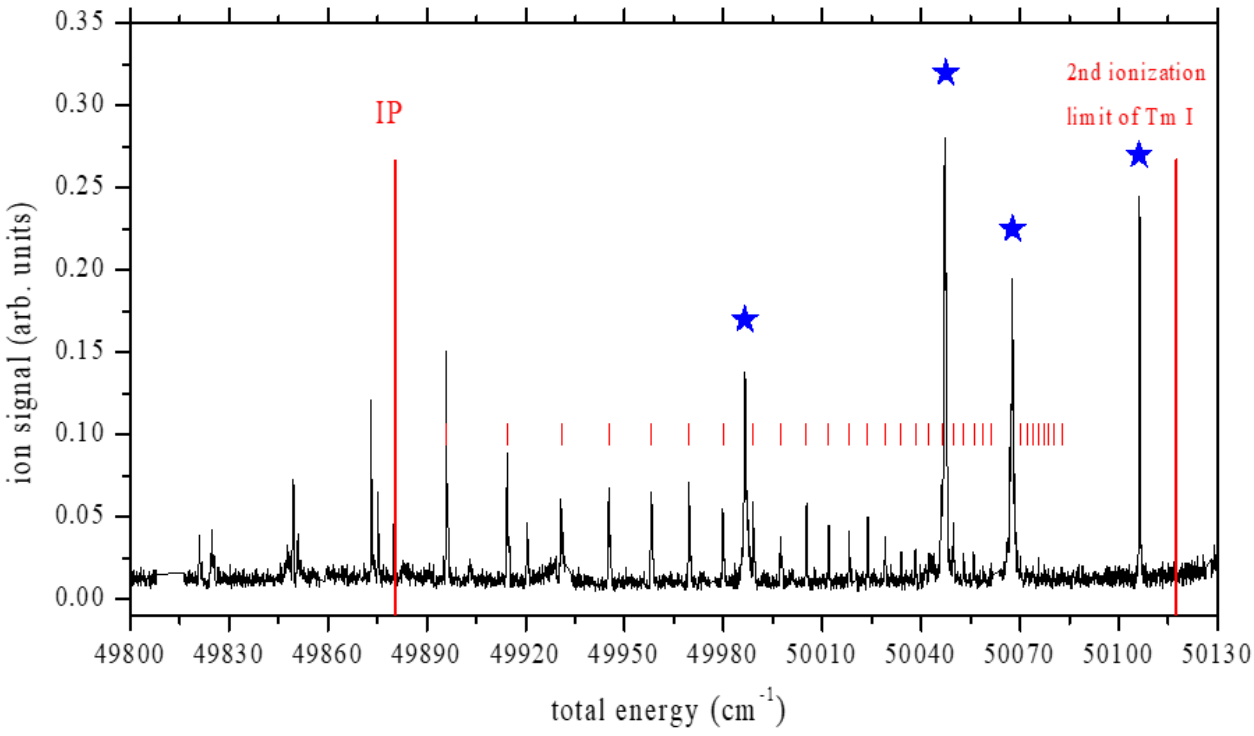

Figure 7.4: Tm odd-parity AI Rydberg states excited from the state $4f^{12}(^3H_5)5d_{5/2}6s^2$ (J = 9/2) 26889.125 cm^{-1} (scheme B). The assigned levels are labeled with " | ". The blue stars label the levels that result from the first excitation step only.

To determine the uncertainty, the spectrum has been scanned several times. A total of 31 resonance lines in the range of int[n*] = 22-56 are identified to belong to a series converging to the first excited state of Tm ion which is 236.95 cm^{-1} above IP. A Gaussian profile was used to fit the resonances of AI Rydberg series since no asymmetries were observed. No obvious perturbations from other series were observed to cause deviations in the intensity distributions and the quantum defect. In Figure 7.5 the convergence of the AI Rydberg series are shown with the fit from the Rydberg-Ritz formula (Eq. 7.1) and the corresponding quantum defects and residuals.

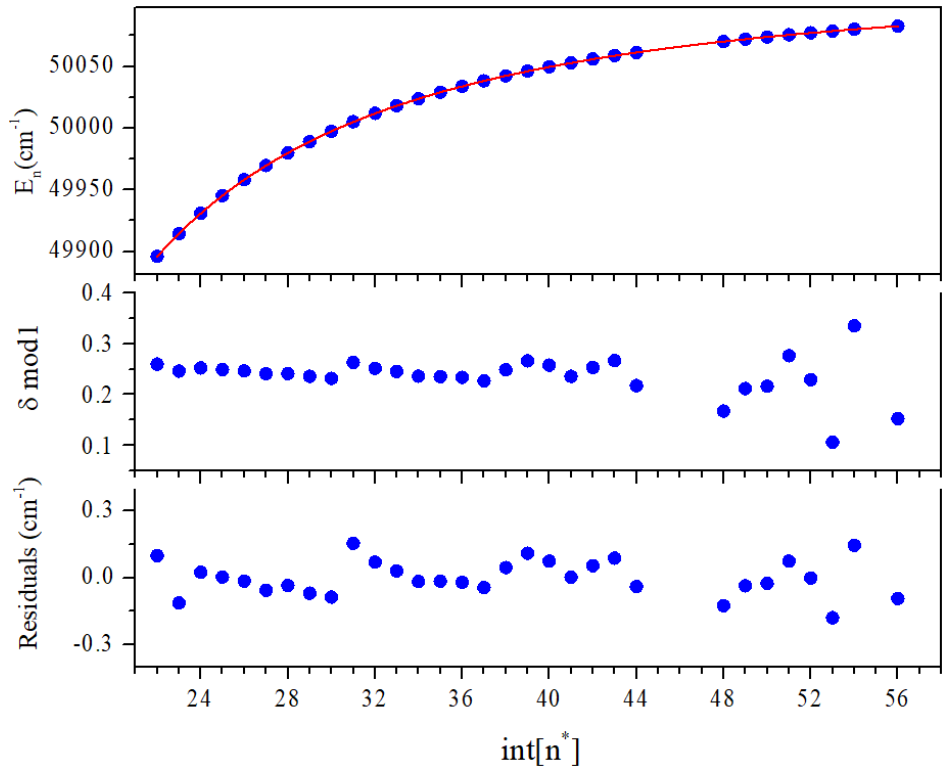

Figure 7.5: Rydberg-Ritz fit for Tm odd-parity AI Rydberg series (Tab. 7.2) converging to 50117.46(4) cm^{-1}. Quantum defects and fitting residuals are given.

The best fit convergence limit of this series results the second ionization limit of 50117.46(4) cm^{-1} = IP + 236.95(2) cm^{-1} for Tm, where 236.95 cm^{-1} is the energy level for first excited state of Tm ion [128]. With this known energy level, the IP for Tm I was extracted as 49880.51(6) cm^{-1} which indicates good agreement with measured IP from Rydberg series in Section 7.4.1.

The weighted average of two extracted values from odd parity Rydberg and AI Rydberg series including an additional systematic uncertainty of 0.04 cm^{-1} from the wavemeter, results in the final value of IP(Tm) = 49880.52(1)$_{stat}$(4)$_{sys}$ cm^{-1}, which is one order of magnitude more precise than the previously reported value of 49879.8(5) cm^{-1} by P. Camus [128]. The statistical error is scaled by reduced Chi-square method.

The comparison between the even-parity Rydberg series of the experiment [131] and the odd-parity series from this work is shown in Figure 7.6. Both measurements indicate fairly constant quantum defects with the ionization potential, 49880.52(3) cm^{-1}, measured from the observed odd parity series. One should note that both n^* and δ in Vidolova's work were recalculated using this new IP value.

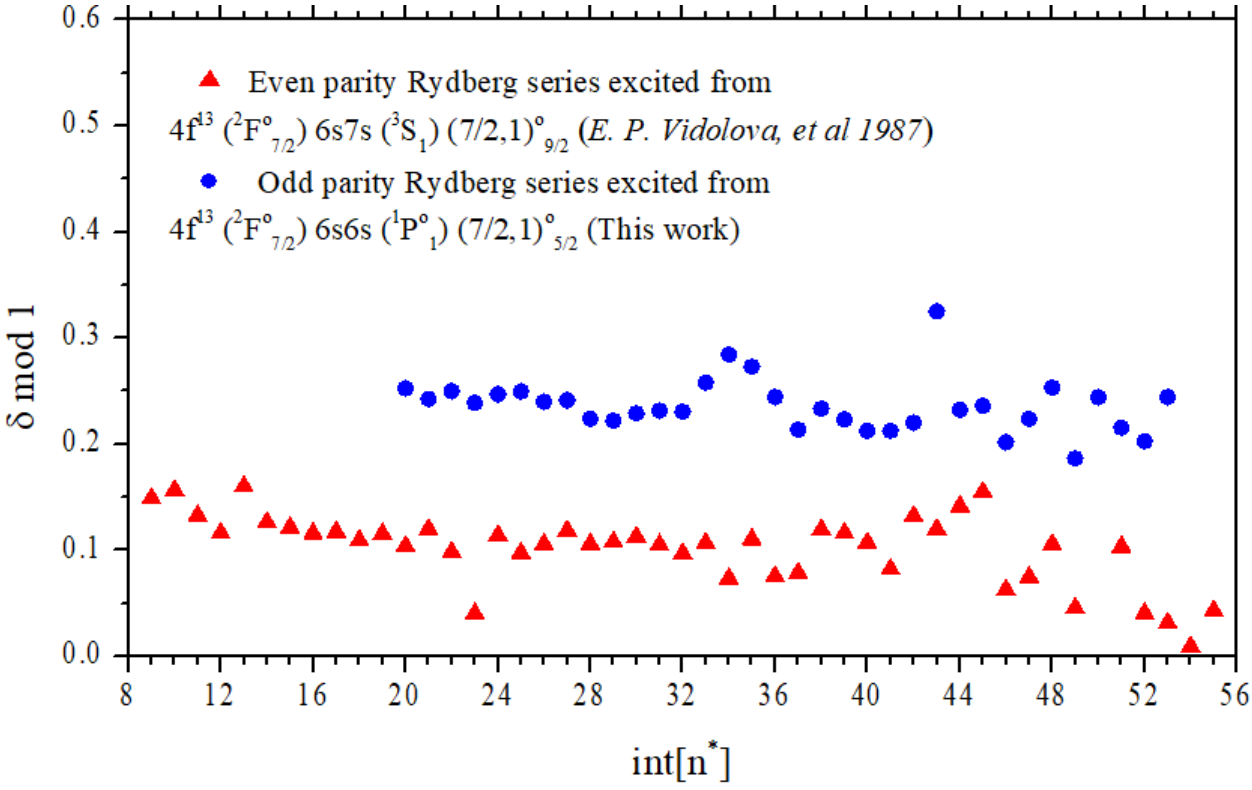

Figure 7.6: Fano-Lu plot of Rydberg series converging to the IP obtained through excitation scheme A and from Vidolova's work [131], as x-axis for the integer part of effective principal quantum number int[n^*] and y-axis for the decimal part of the quantum defect δ as calculated from E_∞ = 49880.52cm^{-1}.

Table 7.1: Odd parity Rydberg series converging to IP = 49880.52(3) cm^{-1}, which was observed via excitation scheme A. δmod1 is the decimal part of the quantum defect δ.

	this work		Vidolova [131]	
int[n^*]	experimental (odd parity)		experimental (even parity)	
	σ(cm^{-1})	δmod1	σ(cm^{-1})	δmod1
9			48569.5	0.15
10			48816.7	0.16
11			48995.1	0.13
12			49133.0	0.12
13			49246.9	0.16
14			49330.6	0.13
15			49400.6	0.12
16			49458.0	0.11
17			49506.0	0.12
18			49545.9	0.11
19			49580.2	0.11
20	49612.97	0.25	49609.0	0.10
21	49637.33	0.24	49634.5	0.12
22	49658.85	0.25	49655.8	0.10
23	49677.32	0.24	49673.8	0.04
24	49693.86	0.25	49691.8	0.11
25	49708.39	0.25	49706.3	0.10
26	49721.14	0.24	49719.5	0.10
27	49732.64	0.24	49731.3	0.12
28	49742.76	0.22	49741.6	0.10
29	49752.01	0.22	49751.0	0.11
30	49760.43	0.23	49759.5	0.11
31	49768.01	0.23	49767.1	0.10
32	49774.88	0.23	49774.0	0.10
33	49781.31	0.26	49780.4	0.11
34	49787.16	0.28	49786.0	0.10
35	49792.32	0.27	49791.5	0.11
36	49796.98	0.24	49796.2	0.10
37	49801.28	0.21	49800.7	0.10
38	49805.45	0.23	49805.0	0.12
39	49809.19	0.22	49808.8	0.12
40	49812.65	0.21	49812.3	0.11
41	49815.91	0.21	49815.5	0.10
42	49818.96	0.22	49818.7	0.13
43	49822.06	0.32	49821.5	0.12
44	49824.43	0.23	49824.2	0.14
45	49826.90	0.24	49826.7	0.15
46	49829.11	0.20	49828.8	0.06
47	49831.31	0.22	49831.0	0.07
48	49833.39	0.25	49833.1	0.10
49	49835.16	0.19	49834.9	0.05
50	49837.05	0.24		
51	49838.68	0.21	49838.5	0.10
52	49840.25	0.20	49840.0	0.04
53	49841.81	0.24	49841.5	0.03
54			49842.9	0.01
55			49844.3	0.04

Tab. 7.1 presents the observed levels from both this work (odd-parity Rydberg series) and Vidolova's work (even-parity Rydberg series) [131]. Observed level energies, corresponding integer part of effective quantum numbers n* and decimal part of the quantum defects δ are presented in Tab. 7.2.

Table 7.2: Odd parity AI Rydberg series converging to an energy level of 50117.46(4) cm^{-1}, which corresponds to the ion $4f^{13}(^2F^o_{7/2})6s_{1/2}(7/2,1/2)^o_3$ level at $\sim$ 236.95 cm^{-1} above the ion ground state.

	this work	
	experimental (odd parity)	
int[n*]	$\sigma(cm^{-1})$	$\delta mod 1$
22	49895.99	0.26
23	49914.39	0.25
24	49930.89	0.25
25	49945.34	0.25
26	49958.17	0.25
27	49969.59	0.24
28	49979.88	0.24
29	49989.08	0.23
30	49997.40	0.23
31	50005.19	0.26
32	50011.97	0.25
33	50018.18	0.24
34	50023.84	0.23
35	50029.08	0.23
36	50033.88	0.23
37	50038.28	0.23
38	50042.46	0.25
39	50046.30	0.26
40	50049.76	0.26
41	50052.93	0.23
42	50056.00	0.25
43	50058.85	0.26
44	50061.34	0.22
45		
46		
47		
48	50070.17	0.17
49	50072.16	0.21
50	50073.95	0.21
51	50075.73	0.27
52	50077.24	0.23
53	50078.56	0.11
54	50080.30	0.33
55		
56	50082.67	0.15

7.5 Highly efficient two-photon ionization scheme for Tm

Comparing the ion signals from scheme A, B and C, the scheme B obviously provides high ionization efficiency. Among all of the observed resonances in scheme B, as shown in Figure 7.7, an AI resonance at 51436.78 cm^{-1} was identified to give the best ionization yield.

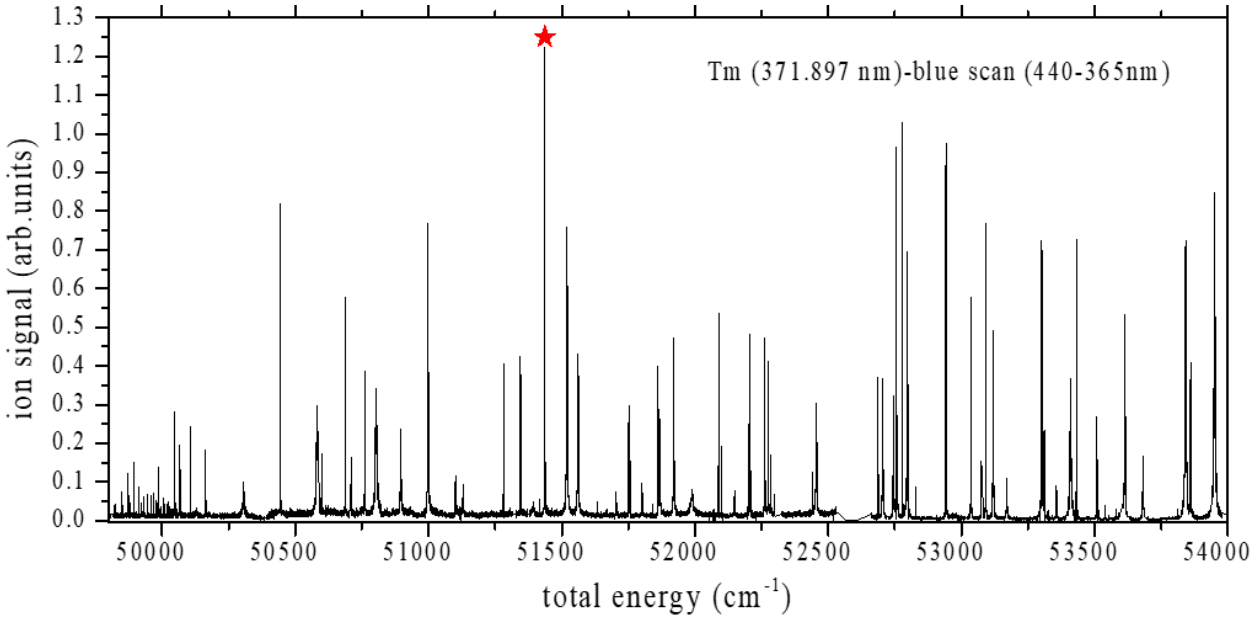

Figure 7.7: Tm spectrum excited from $4f^{12}(^3H_5)5d_{5/2}6s^2$ via scheme B. The red star labels the strongest transition in this scheme, which corresponds to the AI state of 51436.78 cm^{-1}.

The details of this resonance is shown in Figure 7.8. The line shape was fitted with Lorentzian profile to determine the center energy.

To evaluate this excitation scheme (λ_1 = 371.897 nm, λ_2 = 407.371 nm), the saturation behavior of both transitions was measured for radioactive ^{164}Tm in ISAC facility at TRIUMF by varying the laser power with an adjustable attenuator. To measure saturation curve in FES (transition (a) in Figure 7.9), the laser power for the second excited state (SES) was kept at 950 mW. Accordingly, for the measurements in SES (transition (b)), FES laser power was at 220 mW. The measured Tm ion current as a function of the laser power for each excitation indicates that the two steps were all well saturated. The power dependence of the ion current was fitted using

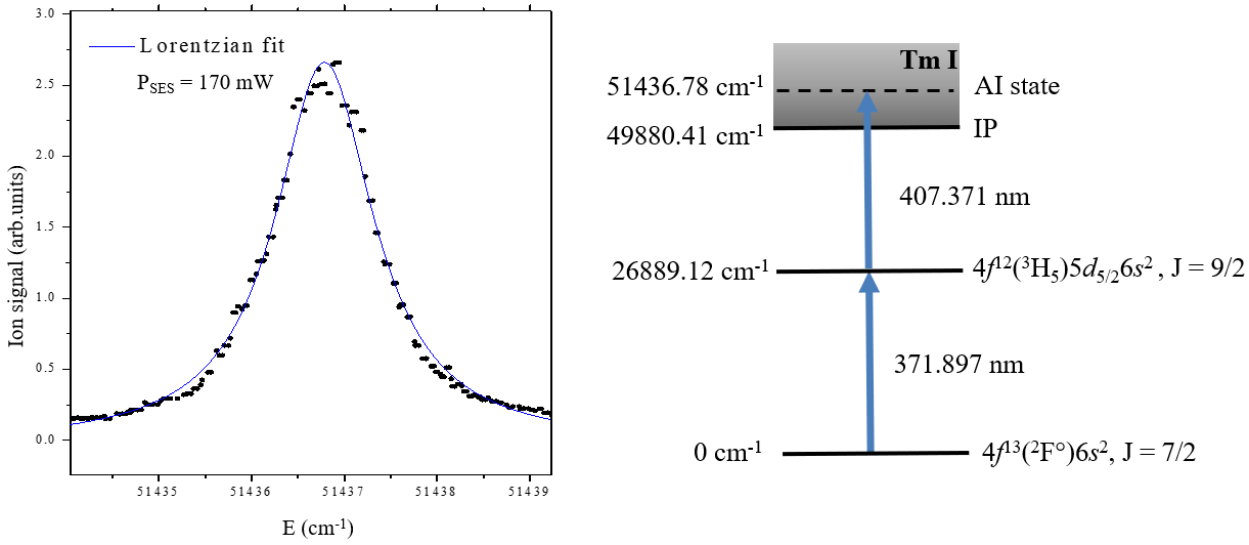

Figure 7.8: Tm excitation scheme used in the on-line measurements. Level energies and configurations are taken from [26]. The laser wavelength are given in vacuum. The saturation intensity for FES was at 12 mW and the resonance has a FWHM = 20 GHz.

$$I(P_{in}) = I_0 + C_1 \frac{1}{1 + P_{sat}/P_{in}} + C_2 P_{in}, \tag{7.3}$$

where linear term accounts for non-resonant photo-ionization as well as background signal, I is the ion current, P_{in} is the laser power, P_{sat} is the saturation power , I_0 is the background ion current, C_1 and C_2 are constants.

Fitting from Eq. 7.3 extracts a P_{sat} = 12(1) mW for the first excited step. The resonance to the AI state has a FWHM = 20 GHz while the Ti:Sa laser linewidth was at 5 GHz. Power broadening in this step is not as strong in the first transition with the saturation power P_{sat} = 140(21) mW. The broad profile of the AI state may come from its natural short lifetime or underlying substructures. This excitation scheme is well suited for use in a resonant ionization laser ion source, with the large resonance linewidth ensuring an efficient excitation, even in the case of small wavelength drift. Ionization efficiency of this scheme was compared to the non-resonant ionization using the first transition in scheme C with high power 532 nm laser at 6.7 W (297.408 nm — 532 nm), and the results show at least 10 times higher efficiency from resonant ionization scheme.

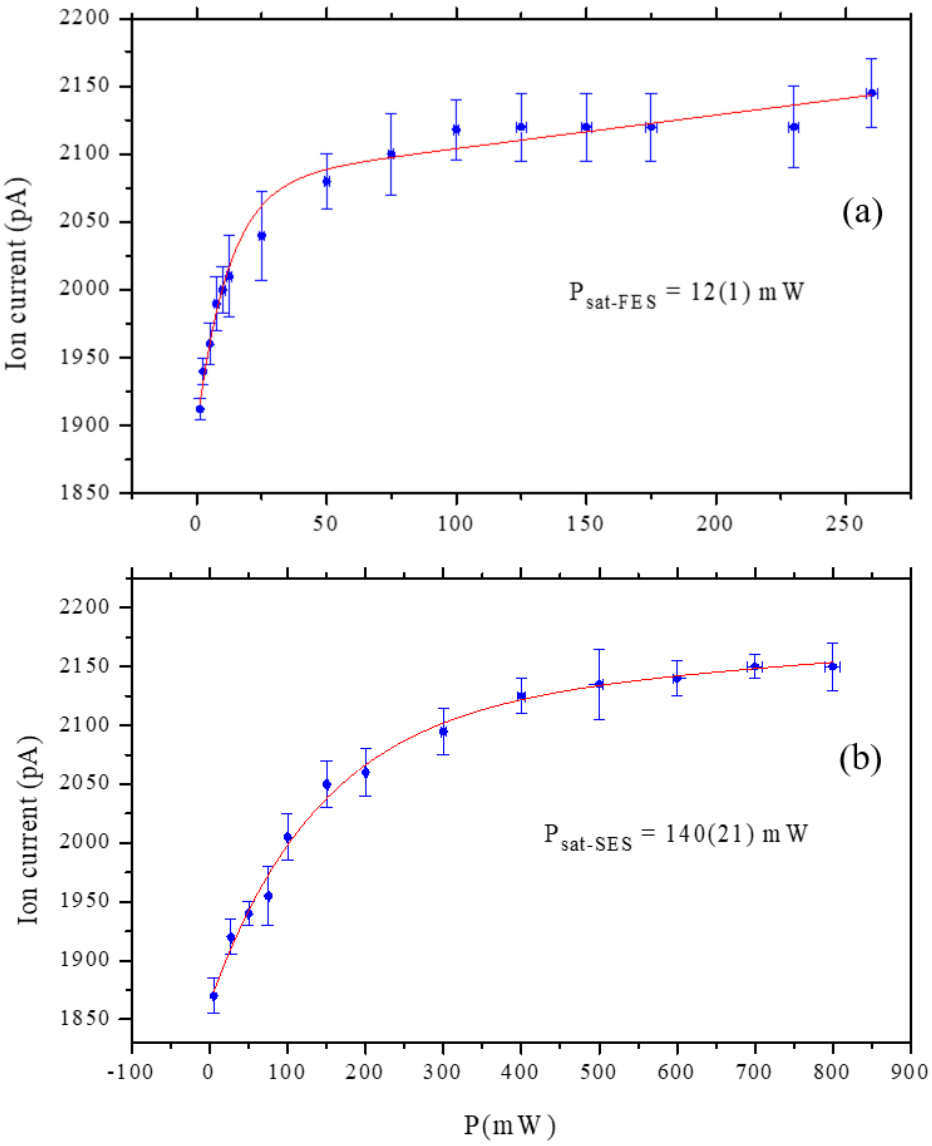

Figure 7.9: Saturation curves of (a) first and (b) second excitation steps. Dots represent the experimental data and lines are the fits to Eq. 7.3. The measurements were performed with radioactive isotope ^{164}Tm. Both transitions were well saturated.

7.6 Radioactive isotopes yield measurements of Tm

The ISAC yield station facility at TRIUMF is built for the rapid and reliable characterization of RIB compositions and intensities. It allows for simultaneous collection of α, β, and γ decay data from RIB. With radioactive decay detection, isotopes can be identified and beam intensities quantified. Intensities between a few and $\sim 10^{11}$ ions per second can be detected and analyzed at the ISAC

yield station. Analysis of individual decay time structures and unambiguous assignment of α and γ lines are demonstrated by data acquisition and analysis software. The coupling of the yield station to the laser ion source, TRILIS, allows the correlation of radiometric data with automated laser frequency scans [143].

The ionization scheme shown in Figure 7.8 was applied for the first time to an on-line Re-lined hot cavity RILIS facility with a 60 μA proton beam on a tantalum (Ta) target in August 2018. Figure 7.10 represents a histogram of ion yields for different isotopes of thulium as the ion count rates with laser on and off. The laser powers were 220 mW and 950 mW for the FES and SES respectively during the yield measurements. The ion yields were derived with the ISAC yield station through evaluating gamma decay counts.

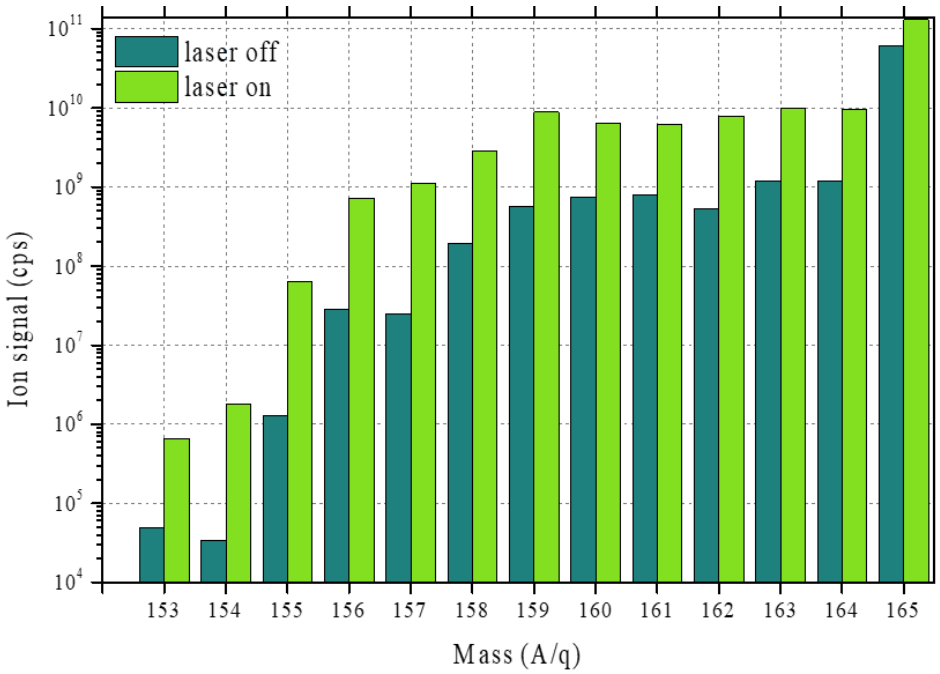

Figure 7.10: Tm radioactive isotope yield from a thick Ta target coupled to a Re lined hot cavity surface ion source bombarded with a 60 μA 480 MeV proton beam. The ionization scheme in Figure 7.8 was used and the ion yields were derived from evaluating characteristic γ lines at the ISAC decay station with laser on and off [143].

7.7 Conclusion

Two step resonant ionization using auto-ionizing states for Tm has been developed at TRIUMF in an IG-LIS off-line laser ion source test stand using tunable Ti:Sa lasers. Ionization schemes involving odd-parity Rydberg states and AI Rydberg states by two-step resonant ionization has been established. Investigation of Rydberg series converging to the IP (the ground state of the core $4f^{13}(^2F^o_{7/2})6s_{1/2}(7/2,1/2)^o_4$) and AI Rydberg series converging to the second ionization limit of 50117.46(4) cm^{-1} (the excited core state of $4f^{13}(^2F^o_{7/2})6s_{1/2}(7/2,1/2)^o_3$) yields the value 49880.52(1)$_{stat}$(4)$_{sys}$ cm^{-1} for the IP, which is one order of magnitude more precise than the quoted value from NIST database. The level energies of the observed autoionizing states were measured and presented. The laser scheme, scanned regions and the total covered energy regions of Tm is summarized in Tab. 7.3.

Table 7.3: Scanned regions to search for Rydberg states and autoionizing states in thulium.

Scheme	Ti:Sa range (nm)	Total energy (cm^{-1})
409 | blue scan	403...357	49240...52415
371 | blue scan	440...365	49600...54250
297 | blue scan	440...367	56375...60900

The most efficient laser ionization scheme (λ_1 = 371.897 nm, λ_2 = 407.371 nm) was found, evaluated and later applied to on-line radioactive Tm isotope delivery. The yields of a radioactive isotope chain $^{153-163}$Tm using a hot cavity RILIS with a Ta target were measured and presented.

8 | Laser spectroscopy of lanthanum

In this chapter, using resonance ionization spectroscopy in conjunction with TRIUMF's off-line test stand, the IP of lanthanum (La) has been determined by analyzing different AI Rydberg series in two step resonant Ti:Sa laser based excitation. Four AI Rydberg series resulting from three different schemes were investigated which converge towards third, eighth and tenth excited state of the lanthanum ion. A combined analysis of the convergence limits leads to a consistent value for the IP of La which is two orders of magnitude more precise than what has been reported previously. The result of this spectroscopy is aimed to be submitted in *Phys. Rev. A* journal [25].

8.1 Properties and history of lanthanum

Lanthanum with atomic number 57 is the first element of the lanthanides in the periodic table. In natural abundance it has only one stable isotope ^{139}La, and a long living isotope ^{138}La (t = 1.02$\times$ 10^{11} years), with abundances of 99.911% and 0.089%, respectively. The unique properties of the lanthanide elements are their small radii of the $4f$ orbitals (smaller than even those of $5s$ electrons) such that the $4f$ electrons are well shielded from outer valence electrons and environmental effects, together with the fact that their binding energies are relatively small and comparable with those of $5d$, $6s$, and $6p$ electrons. Because the binding energies of $4f$, $5d$, $6s$, and $6p$ electrons in neutral lanthanides differ from each other by only a couple of electron volts whereas the spread of energies within a configuration is 5 to 10 eV or more, the various configurations overlap each other to a very high degree. As a result the density of energy levels becomes very high, even at energies as low

as 2.5 eV above the ground level and the interpretation of experimental spectra and energy levels is extremely difficult [144].

La is an important element for estimating the life time of stars. The knowledge of abundance of La and other rare elements helps in understanding the nucleosynthesis process of astrophysical objects and supports the determination of the age of various stars, since their spectral lines are present in stellar spectra. Precise atomic and ionic data are essential for this purpose. Furthermore, accurate determination of the IP is a key to investigate systematic trends in binding energies of neighboring elements and gives valuable information about individual atomic structure. The complexity of the La atomic spectrum has so far prevented a conclusive analysis towards a determination of the IP via Rydberg convergences. First analysis of the La I spectrum was carried out by Russel and Meggers in 1958 [145]. They could estimate the IP to an accuracy of only $\pm 334\ cm^{-1}$ by classification of 540 lines, and the value of 45293 cm^{-1} was obtained from the lowest two members of three series and comparison of quantum defects of the levels with those known for levels of Ca I, Sr I, and Ba I. In 1966 Garton and Wilson [146] observed the ultraviolet absorption spectrum of lanthanum vapor and two odd-parity series interpreted as $5d6s^2\ ^2D_{5/2}$–$6s^2np\ ^2P^o_{3/2}$ and $5d6s^2\ ^2D_{3/2}$–$6s^2np\ ^2P^o_{1/2,3/2}$ (n = 8–23). The lines are broadened by AI for n≥9, and none of the theoretical doublets of the latter series were resolved. Measurement of the higher series members, those not affected severely by autoionization, to an accuracy of about $\pm 2\ cm^{-1}$ led to determination of the $6s^2\ ^1S_0$ limit which lies 7394.550 cm^{-1} above the ground state of La II ($5d^2\ ^3F_2$). Using the known value of La II, $5d^2\ ^3F_2$–$6s^2\ ^1S_0$ from Moore [145], they determined the IP of La I as $44981 \pm 5\ cm^{-1}$. Atomic energy levels of La including the IP derived from Garton and Wilson's work was compiled by Martin *et al.* in 1978 [128]. These results are the last recorded data in the NIST database [26].

Eventually, investigation of highly excited states of lanthanum using two step laser RIS ($5d6s^2\ ^2D_{3/2} \xrightarrow{515.868\ nm} 5d^2\ (^3F)\ ^2D^o_{5/2} \xrightarrow{394\rightarrow371\ nm}$ RS or AIS) by P. Xue *et al.* In 1997 [147] resulted in the value of 44979.8(3) cm^{-1} for the first ionization threshold of La, based on the measured wavelengths of the three Rydberg series. The IP of La was calculated by considering relativistic

corrections in 1998 [148]. Using this method the theoretical IP of lanthanum was reduced from 7.135 to 5.582 eV, which is in better agreement to the experimental value of 5.577 eV. Since then, different spectroscopy and theoretical calculation methods were carried out to find new energy levels and revise the known transition energies of neutral and singly ionized La [149–151]. This work presents spectroscopic data of lanthanum using laser resonance ionization to improve the accuracy of the measured IP of La.

Previous measurements used dye laser based schemes which are not suitable for the Ti:Sa laser based RILIS systems at TRIUMF. Therefore, laser resonance ionization spectroscopy of lanthanum using Ti:Sa lasers at TRIUMF's off-line laser ion source test stand [135] was carried out.

The ionic $5d^2\ ^1D_2$, $5d^2$ a$^3P_1$ and the $6s^2\ ^1S_0$ states lie respectively 1394.471 cm^{-1}, 5718.115 cm^{-1} and 7394.550 cm^{-1} [151] above the ground state of La II. The investigated AI Rydberg series in this work are located below these quoted ionization limits. Using the known excited states of La II [151] and a combined analysis of the convergence limits, a consistent value for the IP of lanthanum was obtained and the level energies of additional states were reported. The ionization efficiency of the strongest AI states from three different schemes were compared and an optimal Ti:Sa laser based scheme suitable for on-line delivery of La radioactive ion beams was identified.

8.2 Ionization scheme development for lanthanum

The ionization is based on two step resonant ionization scheme, which is suitable for Ti:Sa laser based RILIS system. The subject of our two-step laser ionization investigation are four even-parity AI Rydberg series through different ionization schemes.

Ground state transitions

The ground states of La I and La II are $5d6s^2\ ^2D_{3/2}$ and $5d^2$ a$^3F_2$, respectively.

Different excitation and ionization schemes were chosen to investigate Rydberg and AI Rydberg states of lanthanum (Figure 8.1).

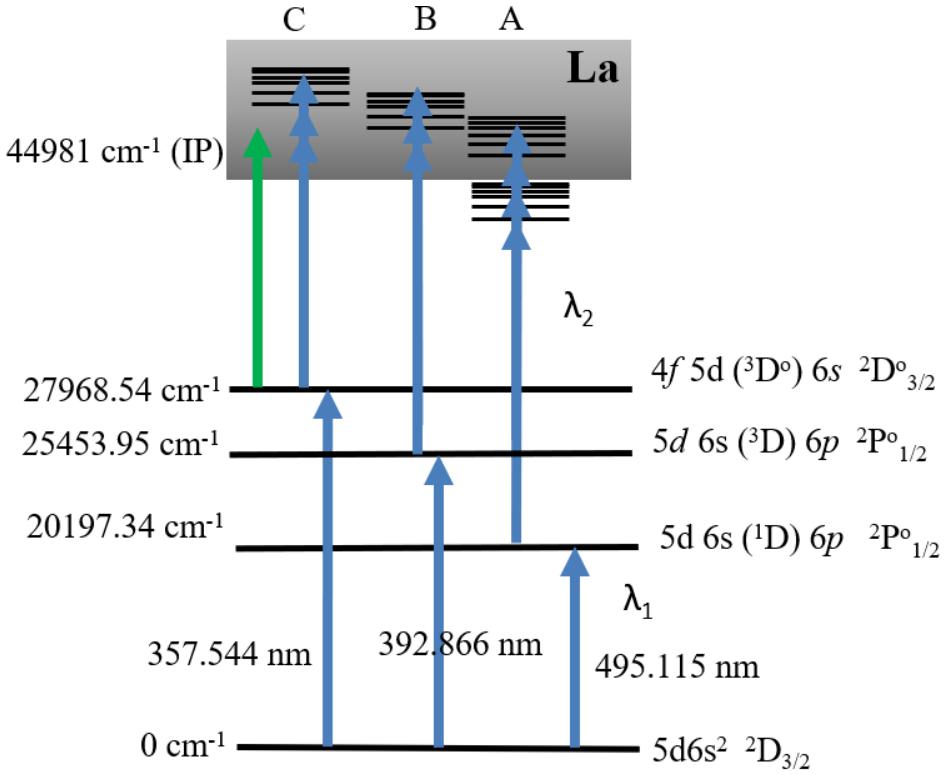

Figure 8.1: lanthanum excitation schemes, presenting the Rydberg and AI Rydberg resonances reached through different second excited state. Green arrow shows the non-resonant ionization which was applied to compare the ionization efficiency of non-resonant scheme to resonant ones.

A transition of 495.115 nm with transition probability $A_{ki} = 9.0 \times 10^7\ s^{-1}$ from the ground state $5d6s^2\ ^2D_{3/2}$ to the excited state of $5d6s\ ^1D\ 6p\ ^2P^o_{1/2}$ was chosen as the FES [26]. This transition is suitable to reach high lying Rydberg series below the IP, as well as AI Rydberg series, while with FES of 357.544 nm transition ($A_{ki} = 9.5 \times 10^7\ s^{-1}$) high lying AI Rydberg series are accessible. Through the FES of 392.866 nm in scheme B (Figure 8.1), two series of AI Rydberg states converging to the 8th excited state of La II $5d^2\ a\ ^3P_1$, were observed.

8.3 Experimental setup

The schematic experimental setup including Ti:Sa laser system for laser resonance ionization of La and the test stand system is shown in Figure 8.2.

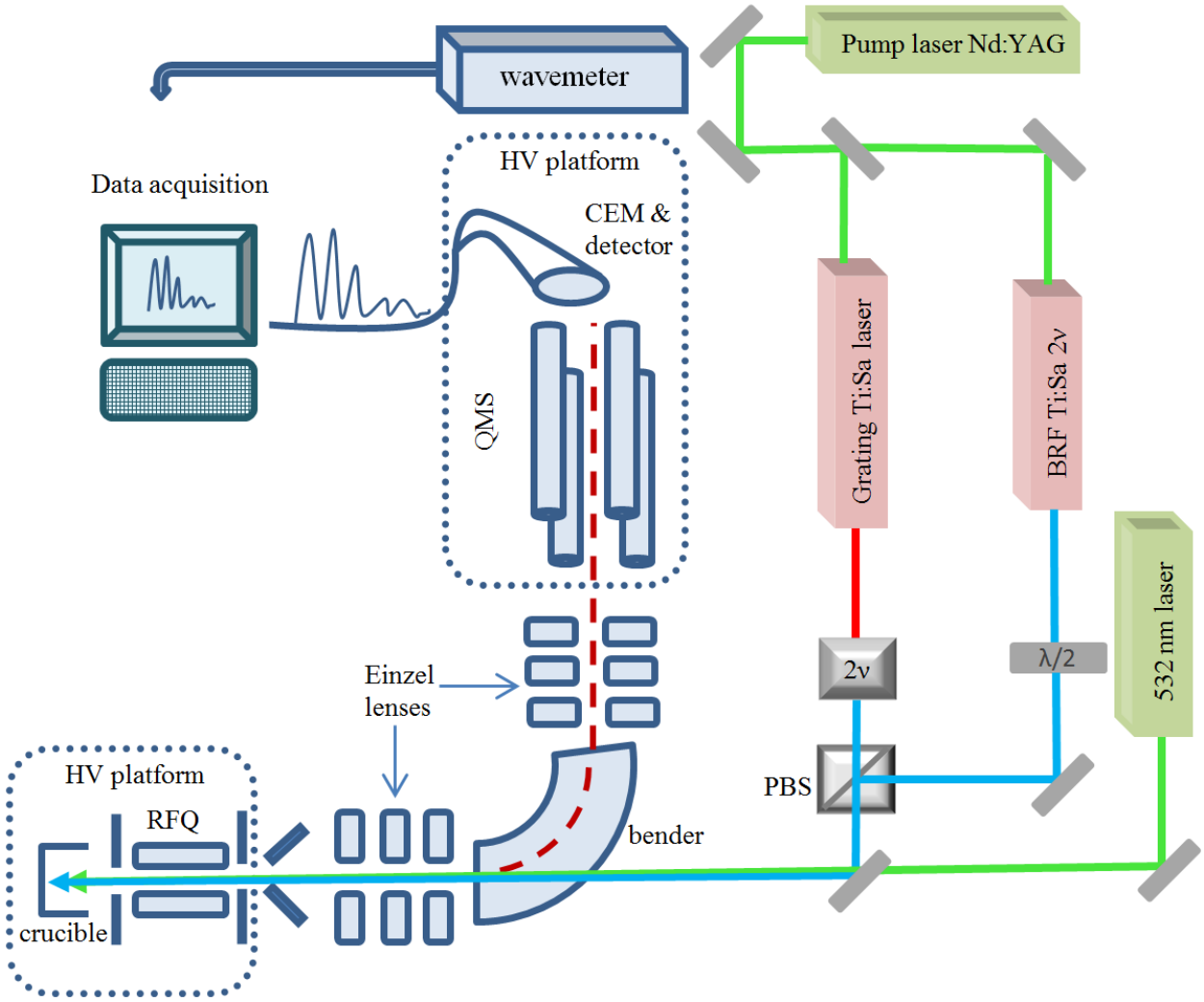

Figure 8.2: Schematic experimental setup for laser ionization spectroscopy of lanthanum at TRIUMF's off-line laser ion source test stand.

The laser system consists of two tunable Ti:Sa pulsed laser, BRF-tuned and grating-tuned. Both lasers were pumped simultaneously by a 30 W Q-switched Nd:YAG laser at 532 nm and 10 kHz repetition rate. BRF-tuned laser was intra-cavity doubled via a nonlinear optical crystal S-LBO and was used for the FES. The linewidth of BRF-tuned Ti:Sa laser fundamental is typically ~ 4 GHz and

6–12 GHz for the grating-tuned laser. The wavelength selection of BRF-tuned laser was achieved by a combination of a 3-plate BRF filter and a solid etalon with 0.3 mm thickness and 40% reflection for the wavelength range of 700-900 nm.

To search for unknown atomic transitions and investigate Rydberg, and AI states a grating-tuned Ti:Sa laser, which allows continuous tuning of $\sim$ 240 nm (700-940 nm), was applied [69]. The grating-tuned laser was externally doubled via a nonlinear optical crystal mounted on a rotary stage and automated continuous second harmonic laser scans with the scan rates as fast as 5 GHz/s were achieved. A commercial TEM BeamLock system was employed to stabilize laser pointing during laser scans.

For non-resonant photoionizaion, a frequency doubled Nd:YVO_4 laser with a temporal pulse width of about 30 ns and an optical output of 12 W for the fundamental wavelength at 1064 nm or 6 W for the second harmonic at 532 nm is available. To synchronize laser pulses temporally, the grating tuned Ti:Sa laser was Q-switched by an intra-cavity Pockel cell. Two laser beams are combined and spatially overlapped in the ionization region by the use of a PBS and dichroic mirrors. The laser wavelengths were monitored and measured by a high Finesse WS6-200 wavemeter with a precision of 10^{-6}. The laser beams were expanded 3-4 times by telescopes and were focused by a $f = 5$ m uncoated lens into the 3 mm diameter ionizer tube located in the vacuum system ($\sim$ 8 m away). A standard 50 μg La solution was loaded into the Ta crucible. The crucible was heated electrically to produce neutral atom vaporization. In the vacuum chamber at a residual pressure of $\sim 10^{-6}$ Torr, neutral atoms interact with laser beams, and are stepwise excited and ionized. The generated La ions are guided through IGLIS [103, 104] and then extracted and accelerated to 10 keV. The ion beam is deflected 90° into the detection system which consists of a quadrupole mass spectrometer and electron multiplier for analysis and detection.

8.4 Spectroscopy results

To investigate possible Rydberg and AI states, the grating-tuned Ti:Sa laser was scanned over the tuning range of $\sim 3500\,\mathrm{cm}^{-1}$ as the SES from energy level of $20197.34\,\mathrm{cm}^{-1}$. A series of even-parity high-lying Rydberg levels converging to the IP $5d^2\ ^3F_2$ and AI Rydberg series converging to the third excited state of La II $5d^2\ a\ ^1D_2$ were observed (scheme A in Figure 8.1). This excited state is located $1394.471\,\mathrm{cm}^{-1}$ above the ground state of La II. Through the FES of 392.866 nm in scheme B (Figure 8.1), two series of AI Rydberg states converging to the 8th excited state of La II $5d^2\ a\ ^3P_1$, were observed. The series of AI Rydberg states converging to $6s^2\ \mathrm{a}^1S_0$ were identified using FES of $4s5d(^3D^o)6s\ ^2D^o_{3/2}$, 357.544 nm (Scheme C, Figure 8.1). The convergence limit of these series reaches to the 10th excited state of La ion. To compare the ionization efficiency through resonant ionization scheme with respect to the non-resonant ionization scheme, a 6 W 532 nm Nd:YVO_4 was employed along with FES transition from scheme C.

8.4.1 Even-parity autoionizing Rydberg states via scheme A

To observe and identify suitable Rydberg series, transitions with strongest transition probability were chosen as FES from NIST database. Among these transitions, FES from scheme A, $20197.34\,\mathrm{cm}^{-1}$, was chosen as an ideal transition to search for Rydberg series below the IP. From this FES, even-parity Rydberg series and AI Rydberg series were observed by applying a frequency doubled grating-tuned Ti:Sa laser which allowed the recording of the spectrum in the range 43450–$46800\,\mathrm{cm}^{-1}$. However, due to the high density of spectral lines below IP, analysis and investigation of the Rydberg series in that region of spectrum was not possible. By excluding the FES and tuning frequency doubled grating laser only, some of these spectral lines were identified as multi-photon excitation/ionization from the ground state or from meta-stable states of $1053.16\,\mathrm{cm}^{-1}$ and $2668.18\,\mathrm{cm}^{-1}$. There is a possibility that some of the other spectral lines, arise from two photon transitions as well. However there are no recorded level energies from the literature to compare these transitions with, therefore assigning them to the two photon resonances will not be reliable. These

spectral lines observed among AI Rydberg resonances, act as perturbers and consequently perturb and shift the Rydberg resonances. Therefore, to calculate the IP of La, only AI Rydberg series converging to different ionization limits above IP were taken into consideration. Figure 8.3 shows a spectrum of even parity AI Rydberg series converging to the ionization limit of 46375.61(7) cm^{-1}, $5d^2\ a\ ^1D_2$, through FES λ_1 = 495.115 nm. The spectrum was taken at a resolution of ~ 2 GHz per step and several measurements with different target temperatures were carried out. The statistical error is estimated as 0.15 cm^{-1} by scanning multiple times over the same energy region.

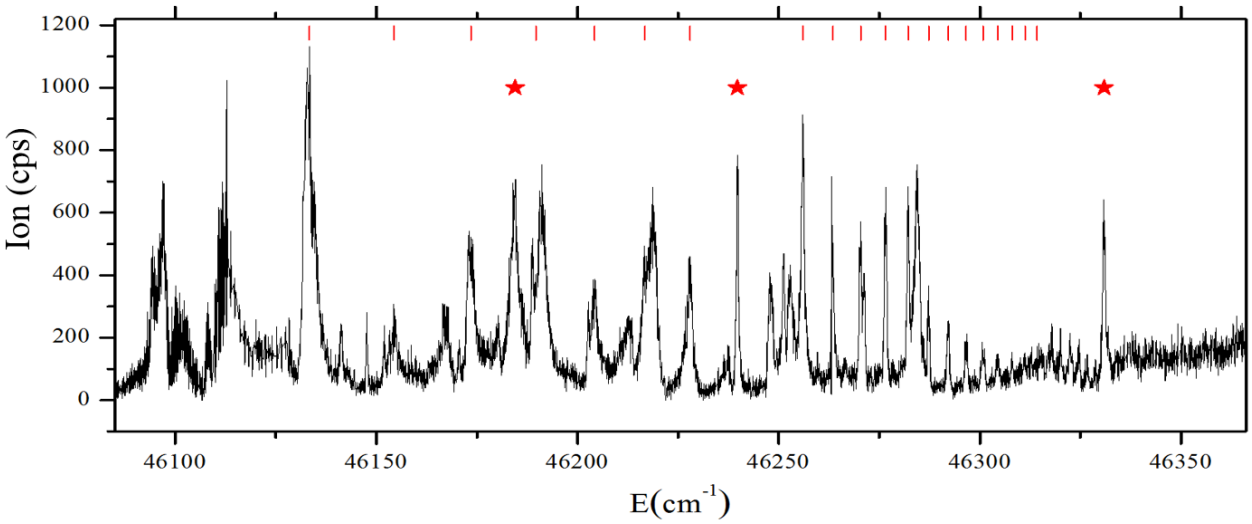

Figure 8.3: Observed AI Rydberg series excited from level energy at 20197.34 cm^{-1} and converging to the 2nd excited state of La ion at 46375.61 cm^{-1}. The red stars show where perturber states exist.

The AI Rydberg series shown in Figure 8.3, reveals several perturbers (marked by an asterisk) which cause asymmetries of the peak shapes and deviations of the neighboring Rydberg members from their expected positions. These interferences result from the interaction of the Rydberg series and the interloping resonances. Therefore, to evaluate Rydberg series, the strongly interloped members were not taken into account. In total, only 20 Rydberg states were assigned in this spectrum. The line shape of the obtained Rydberg resonances are fitted with a Gaussian profile. The position of each resonance is well determined and the systematic uncertainty from High Finesse wavemeter (WS6-200) is 0.04 cm^{-1}. No asymmetries of resonance profile were observed for this series and the combination of laser linewidth along with Doppler broadening was much larger than the natural linewidth of AI Rydberg transitions. The convergence limits of the AI Rydberg series are extracted

by fitting their energy levels to the Rydberg-Ritz formula (Eq. 7.1) with R replaced by R_{La} = 109736.882 cm^{-1}, the mass-reduced Rydberg constant for ^{139}La.

A Fano-Lu plot as well as the Rydberg-Ritz fit for the AI Rydberg series converging to $5d^2\ a\ ^1D_2$ state and the residuals between the experimental data and the fitted value are shown in Figure 8.4.

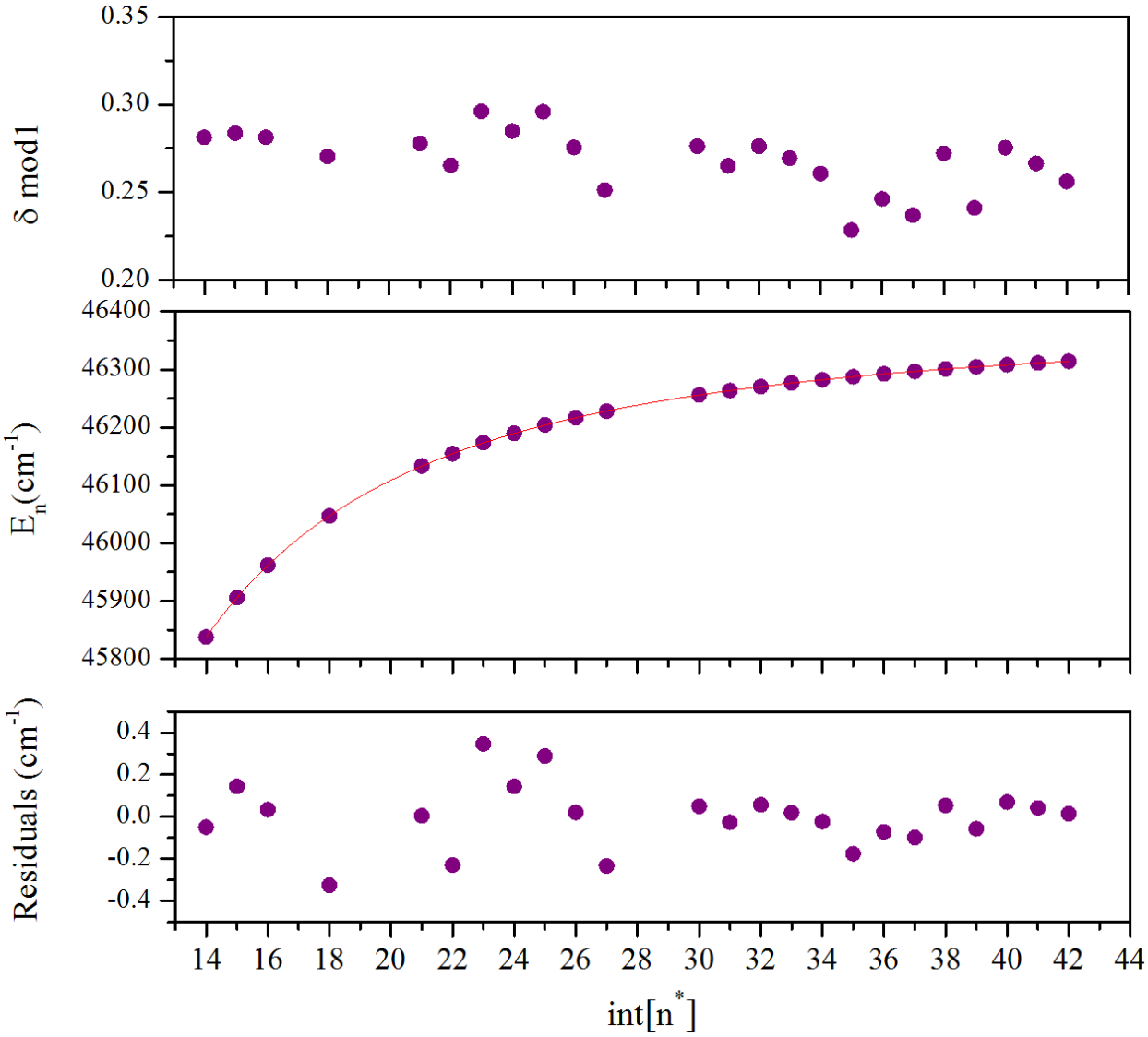

Figure 8.4: The Lu plot and Rydberg-Ritz fit of the series converging to the $a\ ^1D_2$ state of La II. n^* is effective quantum number.

The extracted ionization limit from Rydberg-Ritz fit of observed levels with int[n^*] = 14–42, is E_{limit} = 46375.61(7) cm^{-1} = IP + 1394.471(4) cm^{-1}, where 1394.471 cm^{-1} is the energy level for the second excited state of La ion which has been revised with a good precision in 2018 by weighted

global fits and taking into account the hyperfine constants of involved levels, if possible [151]. With this known energy level, the IP for La I was extracted as 44981.14(7) cm^{-1} which indicates good agreement with the IP from [26] and yet two orders of magnitude more precise.

8.4.2 Even-parity autoionizing Rydberg states via scheme B

In Figure 8.5 the convergence limit of the excitation energies of the observed resonances from scheme B for two AI Rydberg series are shown with fits from the Rydberg-Ritz formula and the corresponding residuals. The energy range of 49835–51300 cm^{-1} was reached through this scheme which allowed the identification of AI Rydberg series converging to the 8th excited state of La II, IP + 5718.115(4) cm^{-1}.

The convergence limits of 50699.25(7) cm^{-1} (series with δ mod1 ~ 0.8) and 50699.24(8) cm^{-1} (series with δ mod1 ~ 0.22) were extracted from these two AI Rydberg series which result in the IP of 44981.14(8) cm^{-1} and 44981.13(8) cm^{-1}, respectively.

8.4.3 Even-parity autoionizing Rydberg states via scheme C

The energy range of 51800–55000 cm^{-1} was accessed using scheme C using FES, 27968.54 cm^{-1}, and scanning a Ti:Sa grating laser from 370 nm to 420 nm. The identified AI Rydberg series from scheme C converge on two excited La ion core states, 7394.550 cm^{-1} and 7473.342 cm^{-1} with configurations of $6s^2$ a^1S_0 and $5d^2$ a^1G_4 respectively [151]. The AI Rydberg series are heavily mixed and form a dense complex of overlapping levels. Figure 8.6 shows a spectrum and corresponding Fano-Lu plots of even-parity AI Rydberg series derived from scheme C.

The quantum defects of the series converging to $6s^2$ a^1S_0 state are varying slowly enough to be fit to Eq. 7.1, while series converging to $5d^2$ a^1G_4 state are dominated by perturbers and cannot be used to evaluate the IP of La I. Fitting data for n=26-56 of the series converging to $6s^2$ a^1S_0 state, resulted in the ionization limit of 52375.71(3) cm^{-1}. With the known energy level from the

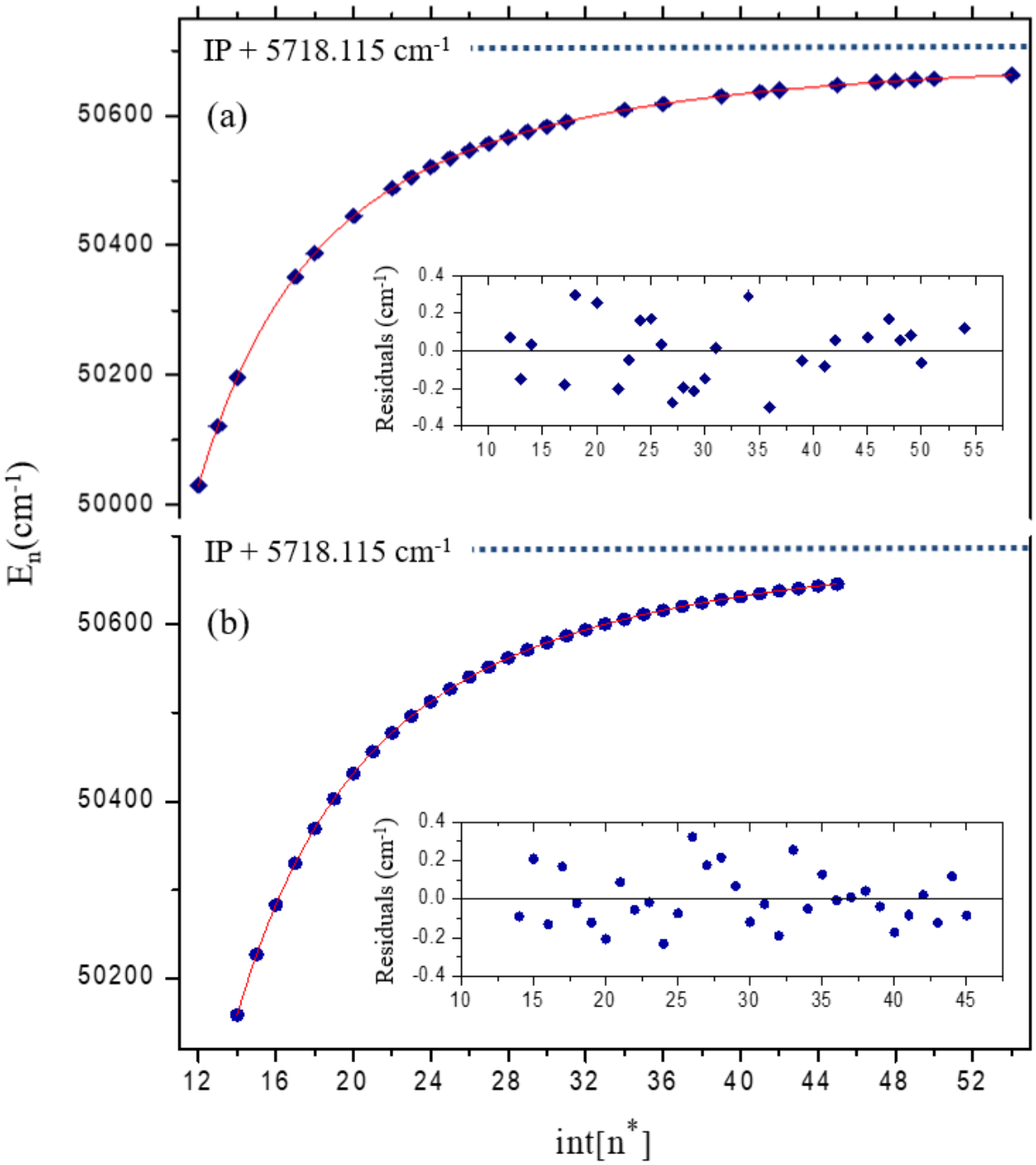

Figure 8.5: Convergences with Rydberg-Ritz fits of individual AI Rydberg series to the 8th excited state of La ion, IP + 5718.115(4) cm^{-1}. (a) for δ mod1 ~ 0.8 and (b) for δ mod1 ~ 0.22. The insets show the residuals of the corresponding series.

excited state of La ion, 7394.550(5) cm^{-1}, the IP of 44981.16(4) cm^{-1} was extracted for La atom. Figure 8.7 shows the Rydberg-Ritz fit of this series along with their fitting residuals.

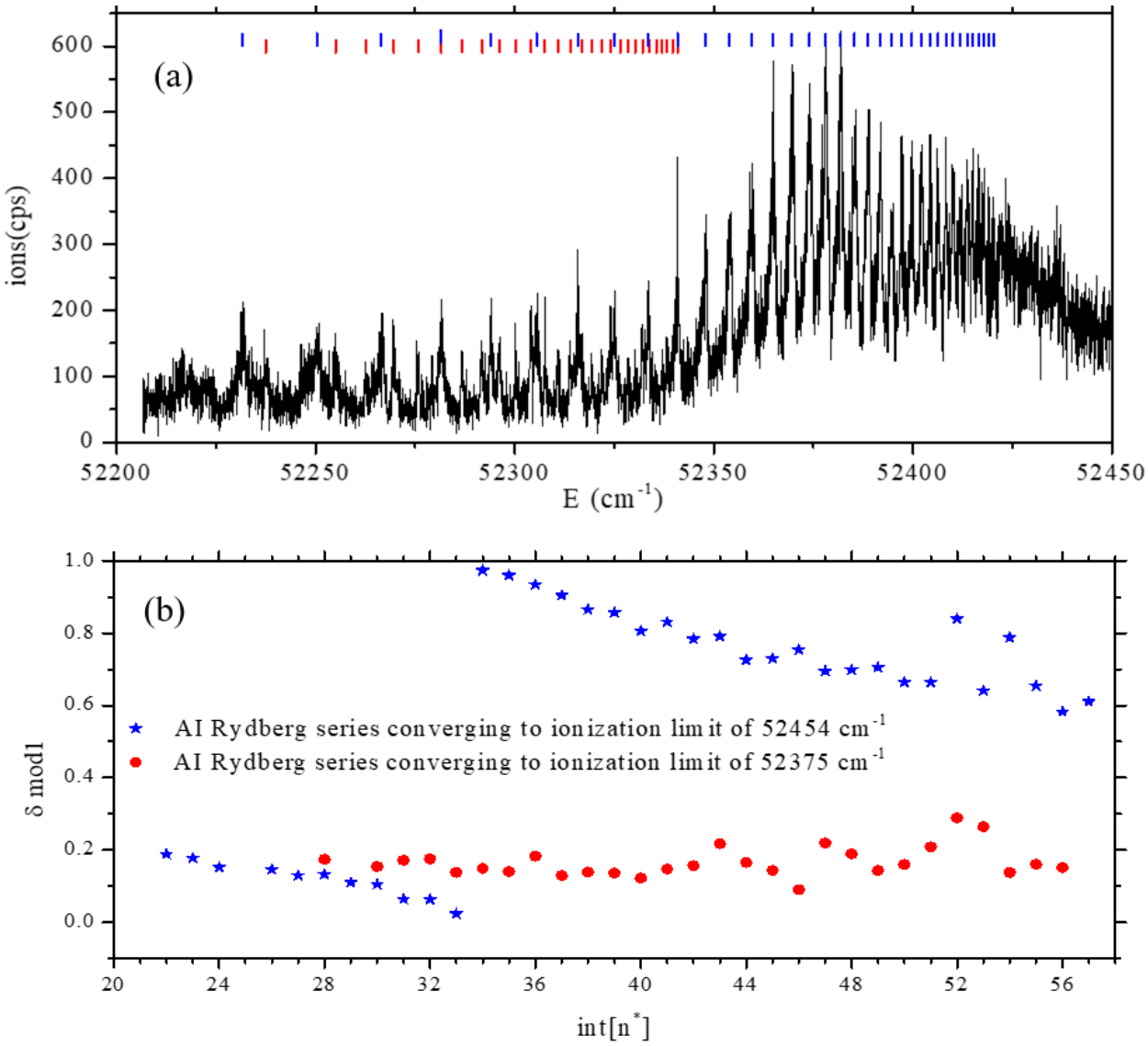

Figure 8.6: La even-parity AI Rydberg a) spectrum, b)Fano-Lu plot, excited from the level of $4s5d(^3D^o)6s\ ^2D^o_{3/2}$ 27968.54 cm^{-1}. The levels assigned with the red and blue labels "|" indicate the series converging to the ionization limits $6s^2\ a^1S_0$ 52375 cm^{-1} and $5d^2\ a^1G_4$ 52454 cm^{-1}, respectively.

8.4.4 Extracted ionization potential for lanthanum

The weighted average from the four extracted values of even parity AI Rydberg series is 44981.15(1) cm^{-1}. Considering the systematic uncertainty of 0.04 cm^{-1} [152], the IP is $44981.15(1)_{stat}(4)_{sys}$ cm^{-1}. The statistical error is scaled by reduced Chi-square method. Calculated ionization potentials from

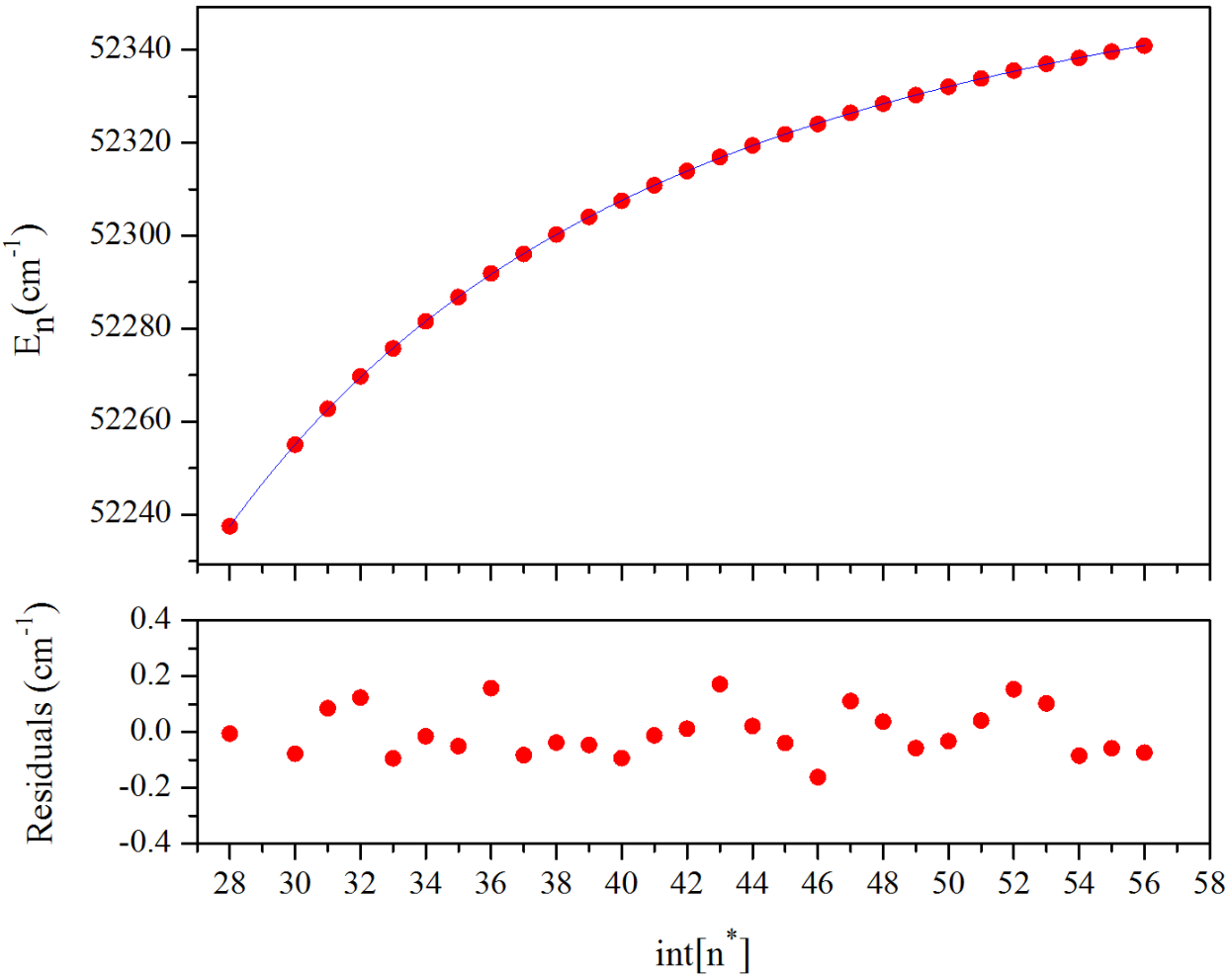

Figure 8.7: The Lu plot for even-parity AI Rydberg series converging to the ionization limit $6s^2$ a^1S_0, 52375.71(3) cm^{-1}.

obtained AI Rydberg convergence limits using corresponding La II excitation energies are tabulated in Tab. 8.1.

Table 8.1: Convergence limits for the individual AI Rydberg series and resulting values for ionization potential IP from known excitation energies E_{exc} for the ionic states. Statistical errors for convergence limits and resulting IP values are given. Two series converge to the limit 50699 cm^{-1} which are related to two different δ mod1, 0.8 and 0.22.

La II E_{exc}(cm^{-1}) [151]	Limit(cm^{-1})	IP(cm^{-1})
1394.471(4)	46375.61(7)	44981.14(7)
5718.115(4)	50699.25(7)	44981.14(8)
5718.115(4)	50699.24(8)	44981.13(8)
7394.550(5)	52375.71(3)	44981.16(4)

Tab. 8.2 presents the identified even-parity AI Rydberg levels derived from schemes A, B, and C corresponding to the integer part of effective quantum number n^* and the decimal part of the quantum defect δ.

8.5 Efficient two-photon ionization scheme of lanthanum

Comparing the two ionization schemes under similar operating conditions, scheme A (Figure 8.1) yielded the highest counts of La ions via an AI state. The corresponding laser wavelengths are λ_1 = 495.115 nm and λ_2=394.431 nm. Figure 8.8 shows the La ionization scheme and the spectral profile of this efficient resonance which was fitted using a Gaussian profile. The FWHM width in this transition is significantly large, ~ 100 GHz, which makes it an excitation scheme well suited for use in a resonant ionization laser ion source as it is robust against frequency drifts and isotope shifts when switching from one isotope to another.

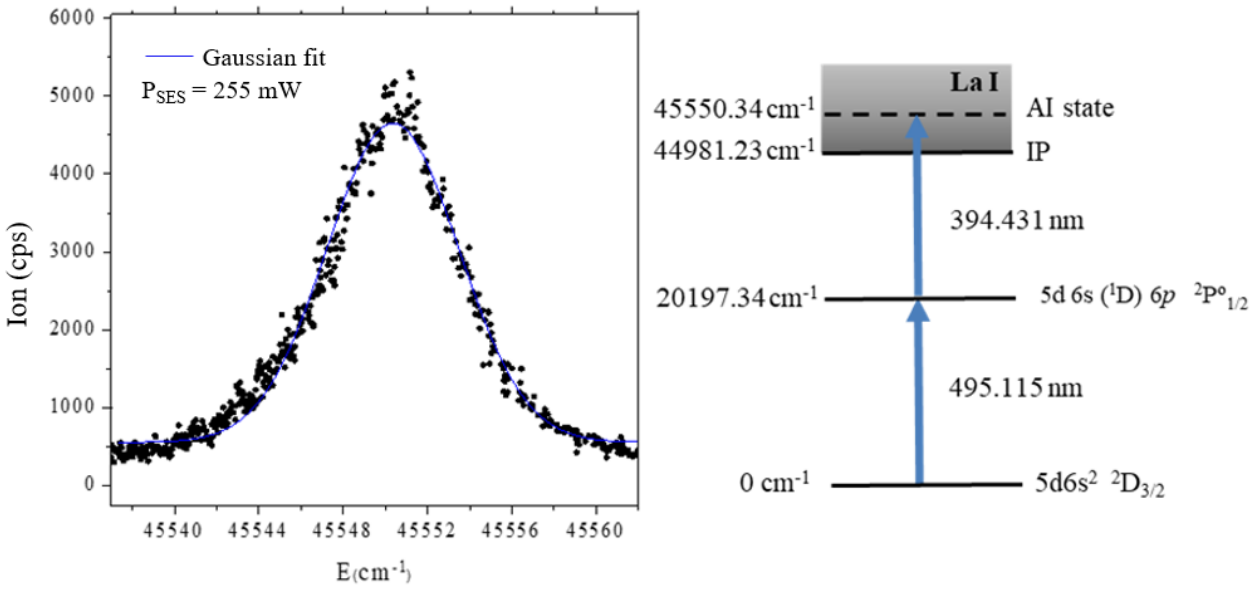

Figure 8.8: La excitation scheme suited for on-line measurements. Level energies and configurations are taken from NIST.

To evaluate this excitation scheme, the saturation behavior of both transitions was recorded by varying the laser power with an adjustable attenuator. The results of these measurements are presented in Figure 8.9.

Table 8.2: Even-parity AI Rydberg series converging to ionization limits 46375.61(7) cm^{-1} and 52375.71(3) cm^{-1} observed from scheme A and B, respectively. The energies are counted from the ground atomic state. δ mod1 is the decimal part of quantum defect δ.

	46375.61(7) cm^{-1}		52375.71(3) cm^{-1}		50699.25(7) cm^{-1}		50699.24(8) cm^{-1}	
int[n*]	$5d^2\ a\ ^1D_2$ state		$6s^2\ a^1S_0$ state		$5d^2\ a\ ^3P_1$ state		$5d^2\ a\ ^3P_1$ state	
	$\sigma(cm^{-1})$	δ mod1	$\sigma(cm^{-1})$	δ mod1	$\sigma(cm^{-1})$	δ mod1	$\sigma(cm^{-1})$	δ mod1
12					50030.01	0.80		
13					50121.36	0.78		
14	45837.65	0.28			50196.34	0.77	50158.23	0.24
15	45905.91	0.28					50226.71	0.24
16	45961.72	0.28					50282.67	0.23
17					50351.53	0.76	50329.91	0.23
18	46046.96	0.27			50388.17	0.78	50369.20	0.23
19							50402.61	0.23
20					50445.42	0.79	50431.19	0.23
21	46133.32	0.28					50456.19	0.25
22	46154.34	0.27			50487.78	0.78	50477.49	0.24
23	46173.50	0.30			50505.39	0.79	50496.25	0.25
24	46189.63	0.29			50520.98	0.80	50512.48	0.24
25	46204.20	0.30			50534.60	0.81	50527.16	0.25
26	46216.75	0.28			50546.57	0.80	50540.44	0.28
27	46227.93	0.26			50557.08	0.78	50551.78	0.28
28			52237.46	0.17	50566.87	0.79	50562.11	0.28
29					50575.60	0.79	50571.21	0.27
30	46255.98	0.28	52255.01	0.15	50583.56	0.80	50579.37	0.25
31	46263.44	0.27	52262.76	0.17	50590.89	0.82	50587.01	0.26
32	46270.36	0.29	52269.70	0.17			50593.71	0.24
33	46276.56	0.28	52275.77	0.14			50600.40	0.31
34	46282.21	0.27	52281.60	0.15	50609.07	0.88	50605.80	0.26
35	46287.27	0.24	52286.83	0.14			50611.21	0.30
36	46292.17	0.26	52291.88	0.18	50618.06	0.76	50615.87	0.27
37	46296.56	0.25	52296.10	0.13			50620.31	0.28
38	46300.78	0.29	52300.26	0.14			50624.41	0.29
39	46304.43	0.26	52304.05	0.14	50630.05	0.81	50628.10	0.27
40	46308.05	0.30	52307.53	0.12			50631.46	0.23
41	46311.26	0.29	52310.88	0.15	50636.48	0.80	50634.79	0.25
42	46314.24	0.28	52313.95	0.16	50639.51	0.85	50637.90	0.29
43			52316.95	0.22			50640.56	0.24
44			52319.44	0.16			50643.42	0.33
45			52321.85	0.14	50647.11	0.87	50645.66	0.25
46			52324.04	0.10				
47			52326.48	0.22	50651.48	0.92		
48			52328.44	0.19	50653.31	0.87		
49			52330.26	0.14	50655.17	0.89		
50			52332.08	0.16	50656.75	0.80		
51			52333.85	0.21				
52			52335.56	0.29				
53			52337.02	0.26				
54			52338.26	0.14	50662.90	0.90		
55			52339.63	0.16				
56			52340.89	0.15				

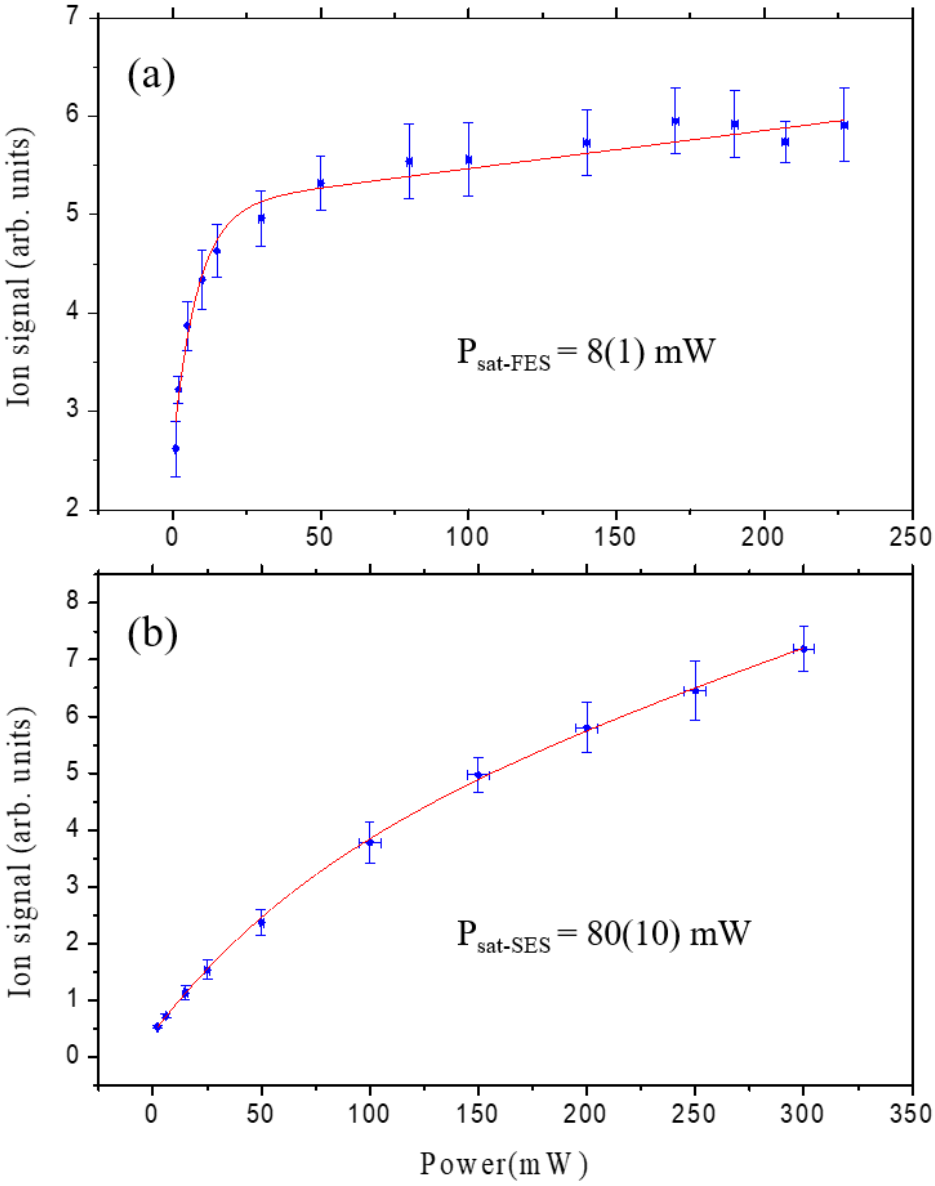

Figure 8.9: Saturation curves of (a) first and (b) second excitation steps. Dots represent the experimental data and lines are fits to the Eq. 7.3. Both transitions were well saturated.

To measure saturation curve in FES (transition (a) in Figure 8.9), the laser power for SES was kept at 255 mW. Accordingly, for the measurements in SES (transition (b)), FES laser power was at 210 mW. The measured Tm ion signal as a function of the laser power for each excitation indicates that the two steps were all well saturated. The power dependence of the ion signal was fitted using Eq. 7.3.

FES was saturated at P_{sat} = 8(1) mW. The resonance to the AI state has a saturation power of about P_{sat} = 80(10) mW. Ionization efficiency of this scheme was compared to the surface ionization and the results show at least 17 times higher efficiency from laser resonant ionization at our source conditions.

8.6 Conclusion

An efficient two step Ti:Sa laser based resonance ionization scheme of La was developed at TRIUMF's off-line test stand. Even-parity AI Rydberg series converging to $5d^2\ a\ ^1D_2$ 46375.61(7) cm^{-1}, $5d^2\ a\ ^3P_1$ 50699.25(7) cm^{-1} and 50699.24(8) cm^{-1}, and $6s^2\ a^1S_0$ 52375.71(3) cm^{-1}, excited respectively from intermediate states of $5d6s\ ^1D\ 6p\ ^2P^o_{1/2}$ 20197.34 cm^{-1}, $5d6s\ ^3D\ 6p\ ^2P^o_{1/2}$ 25453.95 cm^{-1} and $4s5d(^3D^o)6s\ ^2D^o_{3/2}$ 27968.54 cm^{-1}, were observed. Using weighted average value of these four ionization limits, the ionization potential of 44981.15(1)$_{stat}$(4)$_{sys}$ cm^{-1} was extracted for La atom. The measured IP from this work is two orders of magnitude more precise than the quoted value in the NIST database. The observed autoionizing states from three different schemes were compared and the most efficient scheme (λ_1=494.976 nm, λ_2=394.431 nm) was chosen for La on-line beam delivery at TRIUMF. The laser scheme, scanned regions and the total covered energy regions of lanthanum are summarized in Tab. 8.3.

Table 8.3: Scanned regions in search of Rydberg states and autoionizing states in lanthanum.

Scheme	Ti:Sa range (nm)	Total energy (cm^{-1})
495 | blue scan	430...375	43450...46850
392 | blue scan	410...387	49835...51300
357 | blue scan	420...370	51770...54410

Part V

In-source laser resonance ionization spectroscopy

9 | Astatine laser resonance ionization spectroscopy

In this chapter the results of the on-line in-source laser spectroscopy of astatine are presented. The spectroscopy aims to search for autoionizing states of radioactive element astatine. The properties and the motivation for the development of astatine ion beams are summarized. Multi-step RIS schemes in search of efficient ionization schemes for astatine are described. Two new levels were found using the scheme 216.225 nm – 392.540 nm – blue scan. So far no autoionizing states have been observed as a result of this spectroscopy. However, new measurement plan is considered for the future spectroscopy of astatine.

9.1 Properties of astatine

Astatine ($_{85}$At) is the rarest of all the elements found in nature. The extremely short half-lives of all At isotopes preclude the possibility of their independent existence. Isotopes of At occur naturally in both the $4n$ + 2 (^{238}U) and the $4n$ + 3 (^{235}U) decay chains. ^{217}At, a member of the artificial $4n+1$ (^{237}Np) series, has also been detected in natural materials. The longest-lived isotope is ^{210}At, a β^+-emitter with a half-life of 8.3 h, produced by the bombardment of ^{209}Bi with high-energy α-particles. The longest-lived naturally occurring isotope is ^{219}At ($t_{1/2}$= 0.9 min), an α-emitter resulting from the rare α decay-branch of ^{223}Fr ($t_{1/2}$= 22 min) which itself is produced by the 1.38

% α decay-branch of ^{227}Ac (a member of the ^{235}U series), therefore sufficient quantities of ^{219}At for scientific research cannot be provided from natural sources [153].

Astatine is chemically available only as a result of nuclear synthesis. Therefore, its preparation is more difficult than isotopes which are accessible through neutron irradiation. Instead of the conventional nuclear reactor, a particle accelerator is required for the synthesis or production via high energy particle induced fission of the astatine isotopes. Most of the isotopes having more than 126 neutrons are descendants of the neutron-deficient protactinium isotopes prepared in the bombardment of thorium or uranium with high energy particle beams. Heavier isotopes are certainly β-unstable with half-lives of less than a minute. Almost all the known isotopes of astatine are formed by high energy proton induced fission of thorium and uranium. This is the primary production method used at ISAC.

9.2 Ionization scheme development for astatine

Resonance ionization spectroscopy of astatine allows finding atomic energy levels and consequently, via the hyperfine interactions, information about nuclear structure. The focus of this work is to find auto-ionizing atomic states of At, with the aim to boost the overall ionization efficiency of RILIS such that the rare At in particular those heavier than ^{220}At become accessible for study and eventually experiments that rely on the predicted large octupole deformation of these At isotopes.

High ionization efficiency of astatine will open up a path to its neutron-rich isotopes which have been predicted to have octupolar deformed nuclei. Laser spectroscopic identification of auto-ionizing atomic states is a means to provide laser resonance ionization efficiencies beyond those presently achieved with non-resonant ionization.

So far, all studies of astatine have been based on non-resonant ionization schemes. These schemes use two-step resonant laser excitation followed by non-resonant ionization. The non-resonant

ionization step is nowhere near saturation with our available 6 W frequency doubled Nd:YAG lasers. The ion current displays a linear dependence on the ionization laser intensity.

9.2.1 Physics interest in autoionizing states of astatine

The development of an efficient ionization scheme for astatine at ISAC was triggered by the letter of intent S1241LOI [154] where the mass measurements of the neutron-rich astatine isotopes $^{221-224}$At was proposed. On-line isotope separator facilities are ideally suited for fundamental research on nuclear structure and atomic energy levels of rare isotopes of radioactive elements such as astatine or radium.

The chemical element astatine is classified as a halogen and a nonmetal. The known chemical properties of At had been studied in the early days of TRIUMF [155]. Astatine is the least chemically reactive of the halogens and exhibits the most metallic properties of the halogen group elements. ^{211}At is being developed as a radioactive tracer and for cancer treatment. Although there are about 100 radionuclides that decay by the emission of α-particles, only a few have physical half-lives that are compatible with radiotherapy applications. For a radiopharmaceutical with an infinite residence time in a tumor, a radionuclide with a long physical half-life will deliver more decays than one with a short half-life if both have the same initial radioactivity. There is also a striking difference in the time-dependent dose rate delivered by the two. For example, if the number of radionuclide atoms per unit of tumor mass is n and the energy emitted (and absorbed) per decay is E, then the absorbed-dose rate is proportional to nE/T where T is the half-life. The ratio E/T is an important indicator of the intrinsic radiotherapeutic potency of the radionuclide. From a radiobiologic standpoint, higher dose rates delivered over shorter treatment times are more effective than lower dose rates delivered over longer periodes. Thus, a radionuclide with a shorter half-life will tend to be more biologically effective than one with a similar emission energy but longer half-life. Several other criteria that must be considered in selecting an α-emitter for radiotherapy are half-lives of radionuclide daughters, fraction of decays that yield an α-particle, presence γ rays or X-rays, other emissions (β-particles), and radionuclide production methods. ^{211}At not only has

long enough half-life to permit multi-step radiosynthetic strategies, but also has a pure nuclear decay scheme that involves a double-branched pathway [156, 157]. One branch (42 %) is emission of 5.866 MeV α-particles to the long 33.4 year half-life of ^{207}Bi which is not a major safety concern, because the activity of ^{207}Bi generated is only 0.033 MBq (0.0009 mCi) from each 37 MBq (1 mCi) of ^{211}At. The other branch (58 %) is by electron-capture to 520 msec ^{211}Po which then decays by the emission of 7.450 MeV α-particles. The range in tissue of these α-particles is 50 μm and 70 μm respectively [158].

Laser spectroscopic identification of auto-ionizing atomic states is also motivated by enhancing the ionization efficiency of At to establish a delivery path of the heaviest Rn isotopes via decay of At$\rightarrow$ Rn to enable fundamental symmetry studies. Heavier astatine isotopes, in particular ^{223}At which decays into ^{223}Rn, are of special interest to several research programs which study fundamental symmetries. Experiments have shown that $^{219-221}$Rn are likely to have smaller octupole-enhanced EDMs than ^{223,225}Ra, though more favourable Rn candidates may emerge from future studies of the low-lying structure of heavier isotopes [159].

In general, main areas of interest in the development and use of the astatine beams, both at the neutron-deficient and neutron-rich sides are:

a) Studies of the beta-delayed fission (βDF) in the lead region [160, 161];

b) Hyperfine Structure (HFS), Isotope Shift (IS) and charge radii measurements within the long chain of At isotopes, from the very neutron-deficient side across the $N = 126$ neutron closure, up to the most neutron-rich isotopes [60, 162];

c) Shape coexistence in the lightest Po isotopes (β^+/EC- decay products of At), in particular the search for coexisting oblate, prolate and spherical 0^+ band-heads and corresponding excitations in the odd-A Po isotopes [163, 164];

d) Search for octupole collectivity in the neutron-rich Rn isotopes (β -decay products of At). Studies on heavy radon nuclei will contribute to understanding the onset of octupole collectivity in the light actinide region [165, 166];

e) Few-nucleon transfer reactions of At isotopes to study single-particle properties around $N = 126$ and multi-particle multi-hole structures in the neutron-deficient and neutron-rich isotopes [167].

Therefore, successful development of efficient astatine laser ionization schemes would have a significant impact on the progress of these research areas.

9.2.2 Ground state transitions

The first-step transitions from the At atomic ground state were reported in 1964 by McLaughlin as two spectral lines at $\lambda = 224.401$ nm and 216.225 nm [168]. These lines were assigned to the transitions $^2P_{3/2} - ^4P_{5/2}$ and $^2P_{3/2} - ^4P_{3/2}$ between configurations $6p^5$ and $6p^47s$. The investigations of an efficient laser ionization scheme for astatine started in 2010 with the confirmation of the only reported ground state transitions at ISOLDE/CERN and the discovery of three new excited states at ISAC/TRIUMF [169]. In 2011 at ISOLDE, the first ionization potential of astatine (9.31751(8) eV), was measured by means of Rydberg series convergence [170]. However, no autoionizing resonances have been observed so far.

9.2.3 Previously developed laser ionization schemes for astatine

Figure 9.1 shows the ionization schemes and atomic energy levels of At with non-resonant ionization at 532 nm that were developed during previous spectroscopic investigations.

In Figure 9.1(a): the two transitions from the ground states at $\lambda_1 = 216$ nm and 224 nm are verified through ionization path a. Ionization paths b are a two-colour ionization scheme and were applied for scanning the second-step laser wavelength [170]; however, this ionization scheme has an order of magnitude lower efficiency compared to three-colour schemes (paths c and d). The three-colour ionization scheme enabled laser scans across the ionization threshold and consequently

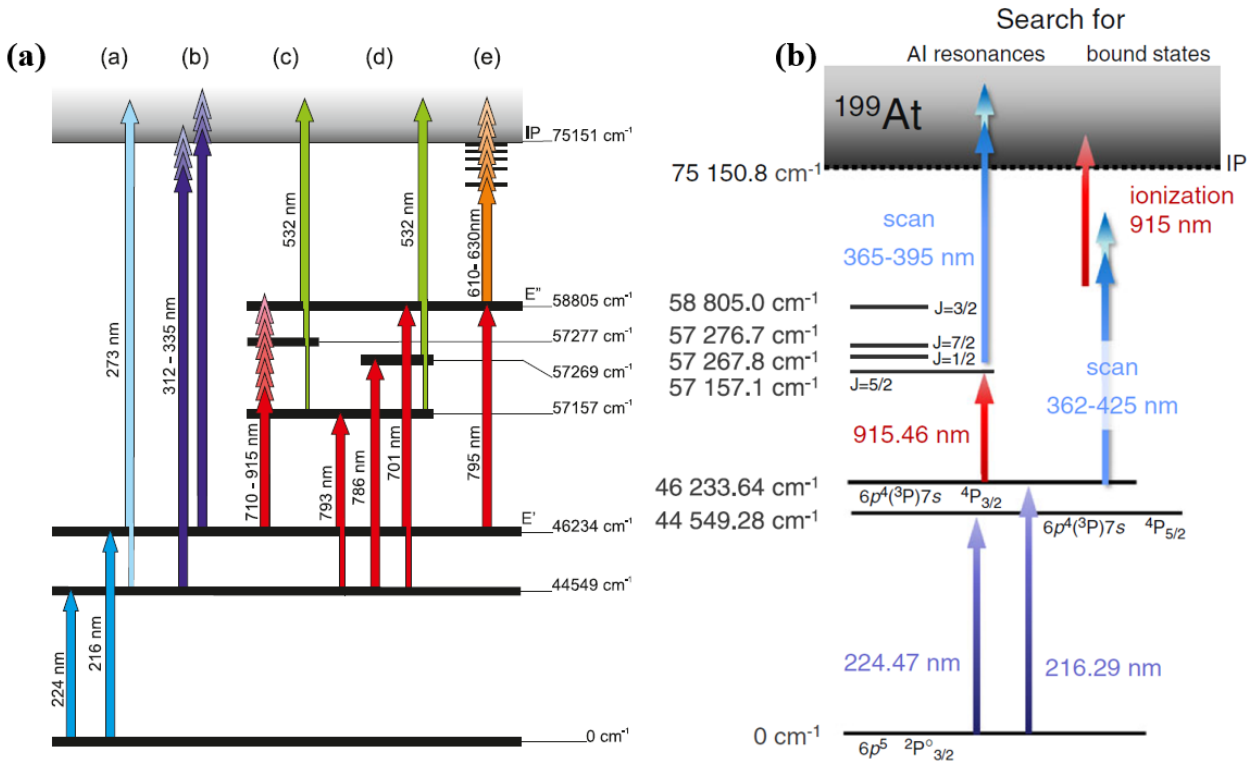

Figure 9.1: Currently known atomic energy levels of At. a) precision determination of the At ionization potential at ISOLDE [170] and b) spectroscopic search for high lying atomic levels in astatine at ISAC [169].

resulted in the discovery of new transitions [171]. The search for these transitions was first performed at TRIUMF and subsequently confirmed at ISOLDE-CERN. Ionization path *e* was used for spectroscopy of Rydberg states in ^{205}At which resulted in a high-accuracy measurement of astatine's IP in 2013 [170]. Spectroscopic search for high lying atomic levels in astatine at TRIUMF is shown in Figure 9.1(b).

9.3 Experimental setup

The target ion source systems at ISAC are irradiated with up to 100μA of protons from the TRIUMF 500 MeV H^- cyclotron. Typically singly charged beams of rare isotopes are extracted from the target station. A mass separator with a resolution of up to $m/\Delta m = 2000$ is used to select particular

isotope beams. It allows some suppression of isobaric contamination below 30 amu. At higher masses, the resolving power is no longer sufficient for efficient isobar suppression.

The option to operate the TRIUMF laser ion source directly with the yield station control system for laser scans opens up the opportunity for hyperfine structure investigations, the possibility of isomer identification and separation and the measurement of optical isotope shifts [60].

Due to the Doppler broadening of spectral lines — which results from the around 2000°C temperature of the ISAC on-line target and ion source combination — and matching laser bandwidth, the resolution for in-source measurements is typically Doppler limited.

To overcome the ionization energy limit, the excited atom is either further excited with a powerful (6 W) pulsed, Nd:YVO_4 laser for non-resonant ionization, or an additional tunable Ti:Sa laser is used for the final excitation of the valence electron into an auto-ionizing state or a subsequently ionized Rydberg-level. All laser beams are overlapped in space and time in the transfer tube/ionization region that connects the target with the ion extraction system and subsequent transport infrastructure. A schematic is given in Figure 9.2.

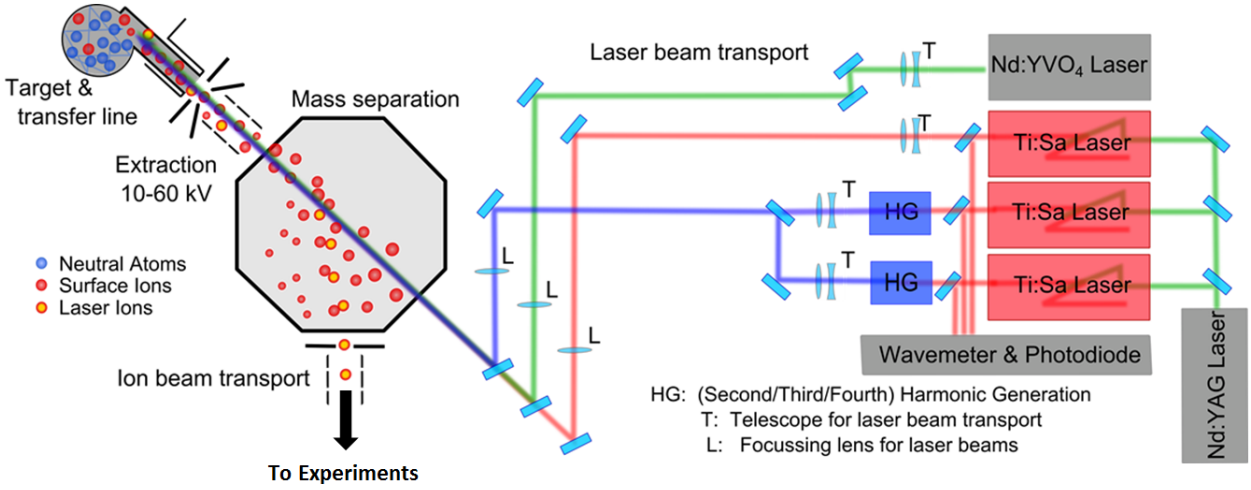

Figure 9.2: Schematic setup for in-source spectroscopy at ISAC. The laser radiation from all solid state laser systems is directed into the transfer tube of the ISAC target ion source. The extracted RIB consisting of laser-ionized species and surface-ionized background is mass-separated and then monitored or delivered to the experiments [169].

At TRIUMF, in-source laser spectroscopy experiments with highly efficient resonant laser ionization in combination with ion counting can be performed. The high sensitivity of ion counting is advantageous for investigation of the heavy astatine isotopes where the in-target production yield starts to drop and limits the achievable yield for short lived isotopes. Unfortunately, a good portion of the At isotopes are accompanied by surface-ionized Fr isotopes at substantial intensity. This isobaric contamination does complicate the search for particularly the heavy At isotopes as one has to refer to nuclear decay counting except for the mass region 199-203 where the Fr isobars have a few ms half lives.

Therefore, laser spectroscopy of astatine was performed on ^{199}At produced from UC_x targets. For ionization spectroscopy, the TRILIS on-line laser ion source with the addition of a diffraction grating Ti:Sa laser was used. The grating-tuned Ti:Sa laser was tunable in its fundamental wavelength from 690 up to 960 nm. Also, automated scanning was accomplished with the frequency doubled grating-tuned laser for extended spectral coverage.

Beam purity is important for many experiments. Due to hot surfaces that are typical in hot cavity ISOL systems, the composition of radioactive beam contaminants can appear in the form of surface ionized isobars and molecular beams. Therefore, to purify RIB, mass separation should be adjusted and optimized for the required beam. Ions of the selected mass can be monitored with either channel electron multipliers (CEM), Faraday-cups (FC), or nuclear decay counting (α, β, and γ-detectors), in parallel to the laser wavelength information using a wavemeter.

9.4 Astatine Spectroscopy

The astatine spectroscopy was performed in 2017 and 2018 with two different measurement plans to scan for AI states in different spectral regions. In both experiments ^{199}At was used for spectroscopy, since this isotope is feasible and there is no contamination from Fr in this region of astatine isotopes due to the short half-life of ^{199}Fr ($t_{1/2}$= 12 ms). This also points to the limits of the ISAC production method for isotopes. Isotopes with half-life on the order of 10 ms no longer can be

extracted successfully from the target. The 216.225 nm (46233.6 cm^{-1}) transition was used as FES for both measurement plans. Due to the high IP of At, three-colour schemes are required. Various intermediate transitions, which were discovered in previous experiments at ISAC/TRIUMF, were applied. To search for AI states, laser scans using an automated doubled frequency of Ti:Sa grating-tuned laser and an automated tripled frequency of Ti:Sa laser (combination of BRF-tuned and grating-tuned Ti:Sa laser described in Section 4.4.2) were performed.

9.4.1 Spectroscopy results from blue scans (2017)

The measurement plan for the 2017 experiment campaign to search for AI states is shown in Figure 9.3.

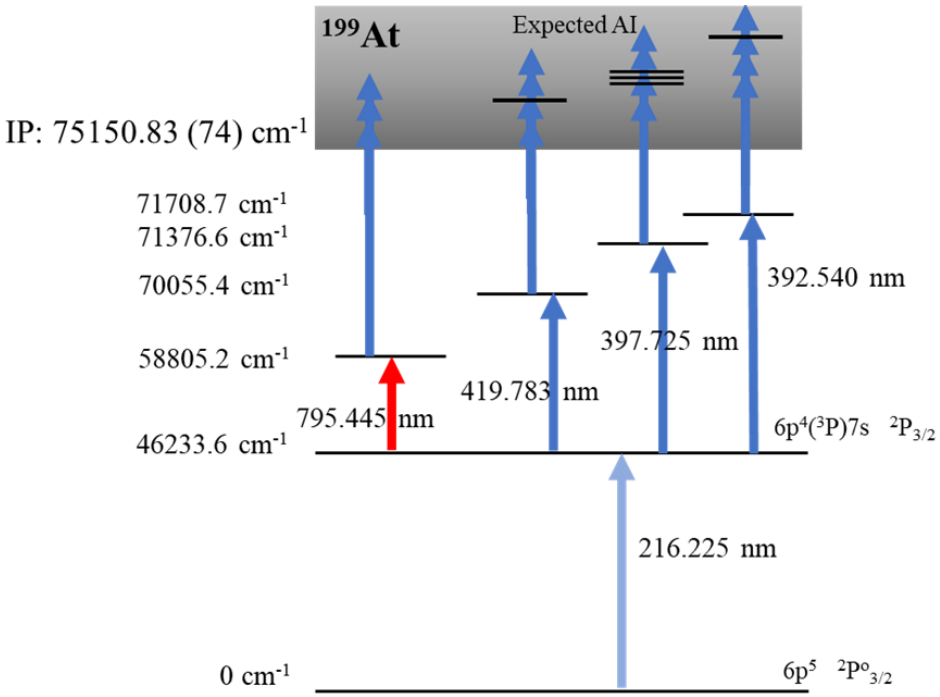

Figure 9.3: Spectroscopic search for high-lying atomic levels in astatine. Plan to scan for autoionization, starting from the 46233.64 cm^{-1} first excited state populated using the frequency-quadrupled output of a Ti:Sa laser. Resonances at 58805.2 cm^{-1}, 70055.4 cm^{-1}, 71376.6 cm^{-1}, and 71708.7 cm^{-1} are odd-parity high-lying bound levels of astatine which were found in previous spectroscopy [169, 171].

As a starting point, three previously identified second excitation steps were applied with a 532 nm laser for non-resonant ionization to confirm these transitions. The transitions 397.725 nm (located

at 71376.6 cm^{-1}) and 419.783 nm (located at 70055.4 cm^{-1}) in Figure 9.3 were not observed in this experiment. Therefore, the spectroscopy was performed from the levels at 71708.7 cm^{-1} and 58805.2 cm^{-1}. Extended laser scans above the ionization potential using a frequency doubled grating laser were done. To confirm the beam from a frequency doubled grating-tuned laser which was used for scanning in this experiment is passing through the source, the FES of thallium (Tl) at 377.686 nm with a green laser (532 nm) for non-resonant ionization was observed successfully.

The experimental proposal for experiment (S1703) [172] was approved with high priority as 4 shifts (each shift is 12 hours). Unfortunately, during the experimental run the proton beam intensity showed severe fluctuations and eventually the main cyclotron went down for unscheduled repairs.

During this spectroscopy three transitions were found and one of which was identified as the Tl resonance at 377.686 nm. The other two resonances were identified as SES of astatine (Figure 9.4) where final ionization was achieved through non-resonant ionization. The ionization schemes using these resonances are 10 times smaller than in the current ionization scheme of At. No AI resonances were observed in this experiment.

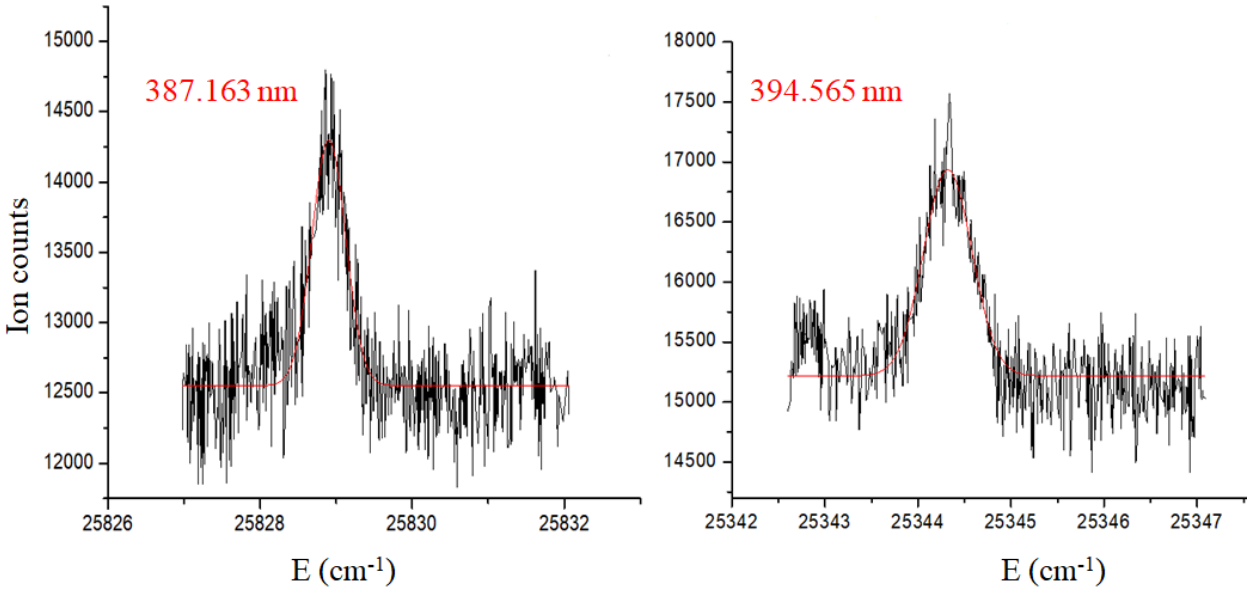

Figure 9.4: Two second excited state resonances found in experiment 2017.

9.4.2 Spectroscopy results from UV scans (2018)

The experiment in 2018 was based on UV (tripled frequency of Ti:Sa laser) scans and make use of the intermediate states found previously in 2012 [171]. The measurement scheme is shown in Figure 9.5.

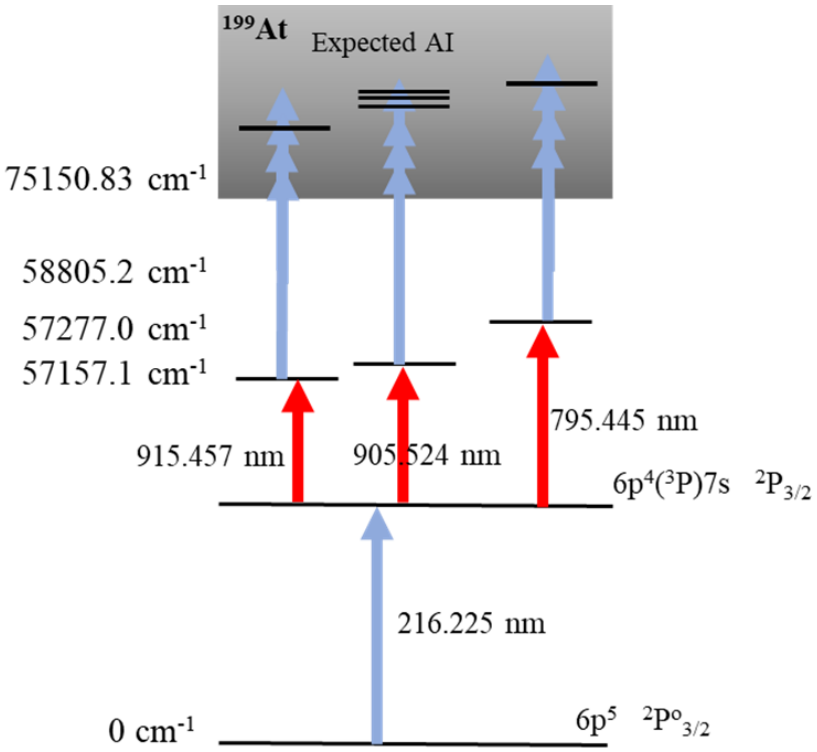

Figure 9.5: Spectroscopic search for high-lying atomic levels in astatine. Plan to scan for autoionization, starting from the 46233.64 cm^{-1} first excited state. Resonances at 58805.2 cm^{-1}, 57277.0 cm^{-1}, and 57157.1 cm^{-1} are odd-parity high-lying bound levels of astatine which were found in previous spectroscopy [171].

The experiment was scheduled to use a UC_x-target bombarded with 5 μA proton beam and the spectroscopy was performed with the mass separator set to $A = 199$. Due to low isobaric contamination at this mass, a suitable signal-to-noise ratio is accessible for ion detection. The 40 mm long and 3 mm diameter hot transfer tube also operates as a surface ion source, and during the spectroscopy of astatine, is responsible for possible background. The target container was heated to about 1500 ^oC. The frequency mixing to access UV region is performed using the method described in Section 4.4.2. The fundamental wavelength from a grating-tuned laser was mixed

with the intra-cavity doubled light from the BRF-tuned laser. Two frequency doubled Nd:YAG lasers were applied to pump the Ti:Sa lasers in this experiment. One of the pump lasers was specifically used for the grating-tuned laser in order to synchronize all the lasers efficiently. The other pump laser was responsible for pumping three BRF-tuned Ti:Sa lasers simultaneously, one intra-cavity doubled frequency (for frequency mixing), one fundamental (for SES), and one quadrupled frequency (for FES). With 3 W output power from grating-tuned laser mixing with 750 mW from frequency doubled Ti:Sa laser, an output power of $\sim$ 100 mW could be achieved for UV wavelength. All excitation steps were saturated with the available laser power. A laser power of 5 mW was available for the FES excitation where from previous measurements the saturation power is at $\sim$ 4 mW [60]. All the three different SES for astatine's ionization could be saturated below 200 mW, while a laser power of $\sim$ 1 W was available. To make sure the last excited step (UV laser) is going through the source, one of the thallium (Tl) resonances (258.092 nm as FES) was chosen in that mass region for spatial beam optimization. Thallium ionization happens through non-resonant ionization (FES+green laser). For spatial optimization of astatine's FES and SES, also a non-resonant ionization path was applied (FES+SES+green).

As a result of this spectroscopy no AI resonances were observed.

9.5 Summary and outlook

Astatine spectroscopy with five different measurement schemes using the 46233.6 cm^{-1} transition as the FES was performed in 2017 and 2018. The continuous scan range using automated doubled frequency and tripled frequency of Ti:Sa laser, covered different energy regions above ionization potential. Laser pointing stability during laser scans was provided. Two new resonances which were identified as SES were recorded as a result of the spectroscopy in 2017. The laser scheme, scanned regions and the total covered energy regions of astatine are summarized in Tab. 9.1.

The future plan is to continue spectroscopy studies of astatine in order to search for autoionizing states via a different scheme using the 44549.28 cm^{-1} (224.401 nm) transition as the first excitation

Table 9.1: Scanned regions in search of autoionizing states in astatine, 2017 and 2018 experiments.

Scheme	Ti:Sa range (nm)	Total energy (cm^{-1})
216 | 392 | blue scan	450...345	93930...100694
		68455...75219
216 | 795 | blue scan	415...381	82901...85052
		70330...72480
216 | 795 | UV scan	313.83...284.69	90669...93931
		78097...81359
216 | 905 | UV scan	277.25...257.43	93345...96122
		82302...85079
216 | 915 | UV scan	275.81...257.43	93413...96002
		82489...85079

step. This transition has higher angular momentum, J value, and may enable a higher probability of finding autoionizing resonances.

Part VI

Conclusion and outlook

10 | Overview and conclusion

The TRIUMF resonance ionization laser ion source (TRILIS) laser system is all solid state laser based and uses home built, pulsed Ti:Sa laser systems. The Ti:Sa laser resonators were designed for use under on-line conditions to fulfill the expected high efficiency and stability over long experimental runs. The fundamental tuning range of 680-1000 nm, frequency doubled of 350-480 nm, tripled frequency of 250-310 nm, and quadrupled frequency of 200-230 nm, efficiently gives access to Ti:Sa-only laser resonance ionization and in principle highly efficient, element selective, isobarically pure RIB's at the ISAC-ISOL facility. Some upgrades were performed on Ti:Sa laser system during this work. My contributions were particularly on grating-tuned Ti:Sa laser system towards the stability of the laser beam pointing, boosting the efficiency of the laser using dual cavity method, and improvement of automatic tracking of doubling/tripling crystal with respect to the grating angle. The latter helped to optimize wavelength recording during scans. My development work on the Cr:forsterite laser helped fill the gap in the visible spectrum covering (600-640 nm) by developing an intra-cavity frequency doubled Cr:forsterite laser pumped by a Nd:YAG laser at 1064 nm. The extended wavelength coverage can be accessed by optimizing the cooling system for Cr:forsterite crystal.

For spectroscopy purposes, TRILIS was upgraded with a self-seeded grating-tuned Ti:Sa laser [73]. Automated scans in the blue (350-460 nm) and UV (250-310 nm) spectral range using this grating-tuned Ti:Sa laser provided opportunities to study different atoms and their respective structures and to discover strong autoionizing resonances for production of RIBs. I set up and extensively used

this system on-line for in-source laser spectroscopy of At. This facilitates access to the isotopes far from stability. Laser beam pointing stability of external cavity frequency doubling and tripling of grating-tuned Ti:Sa laser during wavelength scans was improved with the addition of a beam lock system.

The availability of tunable Ti:Sa lasers and the data recording software in combination with a laser ion source test stand enables the ionization scheme developments for different elements. In this context, I developed off-line efficient two-colour laser ionization scheme for two lanthanide elements, thulium and lanthanum, and fully characterized these ionization schemes, before performing on-line yield measurements at ISAC. With the upgraded Ti:Sa laser systems the ionization potential measurements of the Tm and La atom were determined to be IP(Tm) = 49880.41(5)(4) cm^{-1} and IP(La) = 44981.23(5)(4) cm^{-1}. The IP values were determined in different ways with the most precise result stemming from the analysis of a series of observed high lying Rydberg and autoionizing Rydberg states. The ionization potential, as the binding energy of the valence electron, determines the chemical properties of these elements which can be predicted by means of quantum chemistry calculations. These calculations benefit from the measured value as reference data to assess the various theoretical methods used to simulate Tm and La chemistry, as well as that of their heavier actinide homologues. Journal publications for the La and Tm ionization spectroscopy are in preparation [24, 25].

The ion guide-laser ion source (IG-LIS) is a significant addition to the classical on-line hot cavity RILIS. In IG-LIS the ions generated in the hot production cavity are repelled, and only neutral atoms are admitted into a cold ionization region. The IG-LIS allows to suppress isobaric background from surface ionization substantially and thus deliver isobar free RIBs. The simulation studies derived in this thesis were intended to further understanding and improvement of the operating parameters and to reduce the energy spread of ions extracted from IG-LIS. Ion energy spread reduction improves mass separation and beam transport of the extracted beam. My results will be the basis of an improved IG-LIS to be build and characterized as part of a post doctoral researcher's project in

2020. My development and understanding of the basic IG-LIS operation parameters allows for reliable and knowledge based tuning of IG-LIS operating parameters for transmission mode as well as suppression mode tuning and operation of IG-LIS at highest efficiency.

In-source laser spectroscopy of astatine with five different measurement schemes was performed in search of autoionizing resonances by me during several beam development runs at ISAC. The main purpose for including the At spectroscopy in this thesis was to demonstrate the stability and reliability of the upgraded grating-tuned Ti:Sa laser system in TRILIS for automatic tuning in blue and UV spectrum. The continuous scan range covered a vast energy region above ionization potential of astatine. No autoionizing resonances have been observed so far. However, a different measurement plan is being considered for the continued high priority efforts in astatine in-source laser resonance ionization spectroscopy. Performed At spectroscopy still contributes to the body of spectroscopic knowledge on At.

An updated TRIUMF RILIS status in 2019 using Ti:Sa laser based resonance ionization is presented in Figure 10.1. The development results from this dissertation are shown in red circles. The development allowed direct mass measurements of short lived Tm isotopes via the multiple reflection - time of flight (MR-TOF) mass spectrometry [to be published].

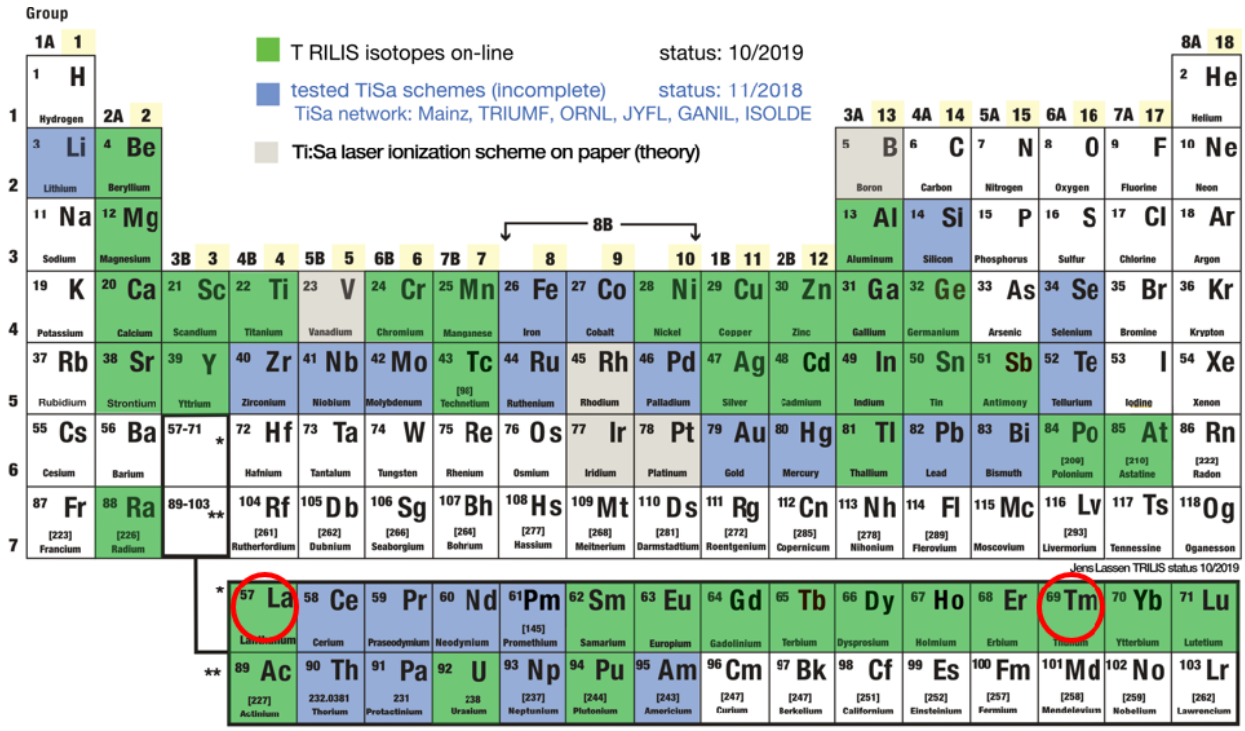

Figure 10.1: Elements delivered with the TRIUMF RILIS (status 10/2019) using Ti:Sa laser based resonance ionization. Laser ionized U is used as a pilot beam for mass separator and beam-line tuning with the ion guide-laser ion source (IG-LIS).

11 | Future prospects

The narrow line-width operation of the TRILIS lasers is key to in-source laser spectroscopy of heavy elements as well as isomer separation. To improve the capabilities and versatility, additional methods for line-width reduction can be implemented. The line-width of the Ti:Sa laser can be reduced further if it is configured as a ring cavity and the pump power is reduced. The tuning range of the Cr:forsterite laser can be extended and more stabilized by optimizing the cooling system of the crystal. For instance, the cooling system can be improved by using different Peltier or lower temperature cooling circuit. To extend the dynamic range of the particle detection and also the FC and CEM measurement ranges, a beam attenuator (10× and 100×) would be helpful as well as further development of the CEM setup and the data acquisition system for on-line yield and spectroscopy measurements. In addition, inserting a CEM before the main mass separator would help with acquiring data on the IG-LIS performance under different operation parameters. From the simulation studies laser repetition rate and the modification of ion guide from a quarupole to an octupole would increase overall efficiency and the energy spread of extracted ions could be well within 1 eV, which can be tested and investigated in the future.

In-source laser spectroscopy of astatine should be pursued further using the different FES of 44549.28 cm^{-1} to search for autoionizing resonances. An ionization scheme through AI resonances gives access to the neutron-rich isotopes of At which are the main interest for electric dipole moment and nuclear octupole deformation studies.

Acronyms

AI autoionizing

BBO β-barium-borate

BiBO bismuth-borate

BRF birefringent filter / Lyot filter

CEM channeltron electron multiplier

CERN Organisation Européenne pour la Recherche Nucléaire (renamed from Conseil Européen pour la Recherche Nucléaire) (Switzerland)

Cr:Forsterite or Cr:Mg_2SiO_4 chromium-doped forsterite

ECR Electron Cyclotron Resonance

EI electron impact

FEBIAD Forced Electron Beam Induced Arc Discharge

FHG forth harmonic generation

FRIB Facility for Rare Isotope Beam

FSR free spectral range

FWHM full-width half-maximum

GANIL Le Grand Accélérateur National d'Ions Lourds (France)

GSI Helmholtzzentrum für Schwerionenforschung (Germany)

HR high reflector

HRIBF Holifield Radioactive Ion Beam Facility

IF in-flight

IG-LIS ion guide laser ion source

IGISOL Jyväskylä Ion Guide Isotope Separator On-Line

IP ionization potential

IPN Institut de Physique Nucléaire Orsay (France)

ISAC Isotope Separator and ACcelerator

ISOL Isotope Separator On-Line

ISOLDE Isotope Separator On-line DEvice

KDP potassium dihydrogen phosphate

LBO lithum-triborate

LIS Laser Ion Source

LIST laser ion source trap

MSU Mitchigan State University

Nd:YAG neodymium-doped yttrium aluminum garnet

Nd:YVO_4 neodymium-doped yttrium orthovanadate

NIR near infrared

OC output coupler

ORNL Oak Ridge National Laboratory

QDT Quantum defect theory

RFQ radio frequency quadrupole

RIB radioactive ion beam

RIKEN Rikagaku Kenkyujo, The Institute of Physical and Chemical Research (Japan)

RILIS resonant ionization laser ion source

RIS resonance ionization spectroscopy

SHG second harmonic generation

SIS surface ion source

THG third harmonic generation

Ti:Sa titanium-doped sapphire

TRILIS TRIUMF's Resonant Ionization Laser Ion Source

TRIUMF Canada's National Laboratory for Particle and Nuclear Physics and Accelerator-based Science (renamed from Tri University Meson Facility) (Canada)

UV ultraviolet

VIS visible spectrum

Bibliography

[1] M. Lieuvin. Design issues of radioactive ion beam facilities. *EPAC96, Sitges, SPAIN,*, (1996).

[2] Gelletly W., Morrissey D. J., and Sherrill B. M. Radioactive nuclear beam facilities based on projectile fragmentation. *P. Roy. Soc. A-Math. Phys*, 356(1744):1985–2006, (1998).

[3] Y. Blumenfeld, T. Nilsson, and P. Van Duppen. Facilities and methods for radioactive ion beam production. *Phys. Scr*, T152:014023, (2013).

[4] D. J. Morrissey. Status of the FRIB project with a new fragment separator. *J. Phys*, 267(1), (2011).

[5] H. Geissel, P. Armbruster, K. H. Behr, A. Brunle, and et al. The GSI projectile fragment separator (FRS): A versatile magnetic system for relativistic heavy ions. *Nucl. Instrum. Meth. B*, B70:286–297, (1992).

[6] D. J. Morrissey, B. M. Sherrill, M. Steiner, A. Stolz, and I. Wiedenhoever. Commissioning the a1900 projectile fragment separator. *Nucl. Instrum. Meth. B*, 204:90–96, (2003).

[7] A. G. Artukh, Yu. M. Sereda, S. A. Klygin, G. A. Kononenko, and et al. The COMBAS fragment separator. *Instrum. Exp. Tech*, 54(5):668, (2011).

[8] T. Kubo. Recent progress of in-flight separators and rare isotope beam production. *Nucl. Instrum. Meth. B*, 376:102–110, (2016).

[9] P. Bricault, F. Ames, M. Dombsky, P. Kunz, and J. Lassen. Rare isotope beams at ISAC—target & ion source systems. *Hyperfine Interact*, 225, (2013).

[10] R. Kirchner. Review of ISOL target–ion-source systems. *Nucl. Instrum. Meth. B*, 204:179–190, (2003).

[11] R. Kirchner. Progress in ion source development for on-line separators. *Nucl. Instrum. Meth*, 186(1):275–293, (1981).

[12] R. Kirchner and E. Roeckl. Investigation of gaseous discharge ion sources for isotope separation on-line. *Nucl. Instrum. Meth*, 133(2):187–204, (1976).

[13] R. Geller. Highly charged ECR ion sources: Summary and comments (invited). *Rev. Sci. Instrum*, 61(1):659–661, (1990).

[14] J. Lassen, P. Bricault, M. Dombsky, J. P. Lavoie, Ch. Geppert, and K. Wendt. Resonant ionization laser ion source project at TRIUMF. pages 69–75. Springer Berlin Heidelberg, (2006).

[15] M. Marchetto. Magnetic field study for a new generation high resolution mass separator. *PhD thesis, University of British Columbia*, (2017).

[16] J. Lassen, et al. Current developments with TRIUMF's titanium-sapphire laser based resonance ionization laser ion source. *Hyperfine Interact*, 238(1):33, (2017).

[17] A. Sen, F. Ames, P. Bricault, J. Lassen, A. Laxdal, and A. Mjϕs. Extraction and low energy beam transport from a surface ion source at the TRIUMF-ISAC facility. *Nucl. Instrum. Meth. B*, 376:97–101, (2016).

[18] R. V. Ambartzumian and V. S. Letokhov. Selective two-step (STS) photoionization of atoms and photodissociation of molecules by laser radiation. *Appl. Opt*, 11(2):354–358, (1972).

[19] G. D. Alkhazov, E. Ye. Berlovich, and V. N. Panteleyev. A new highly efficient selective laser ion source. *Nucl. Instrum. Meth. A*, 280(1):141–143, (1989).

[20] A. E. Barzakh, D. V. Fedorov, A. M. Ionan, V. S. Ivanov, F. V. Moroz, K. A. Mezilev, S. Yu. Orlov, V. N. Panteleev, and Yu M. Volkov. Changes in the mean square charge radii of neutron-deficient europium isotopes measured by the laser ion source resonance ionization spectroscopy. *Eur. Phys. J. A*, 22(1):69–74, (2004).

[21] U Köster, V. N Fedoseyev, and V. I Mishin. Resonant laser ionization of radioactive atoms. *Spectrochim. Acta. B*, 58(6):1047–1068, (2003).

[22] R. E. Horn. Aufbau einers Systems gepulster, abstimmbarer Festkörperlaser zum Einsatz in der Resonanzionisations-Massenspektrometrie. *PhD thesis, Johannes Gutenberg-Universität Mainz*, (2003).

[23] M. Mostamand, R. Li, J. Romans, F. Ames, P. Kunz, A. Mjϕs, and J. Lassen. Production of clean rare isotope beams at TRIUMF ion guide laser ion source. *To be submitted in Hyperfine Interact.*, (2019).

[24] M. Mostamand, R. Li, J. Romans, and J. Lassen. Study of odd-parity Rydberg and autoionizing states of thulium by laser resonance ionization spectroscopy. *To be submitted in Spectrochim. Acta. B.*, (2019).

[25] M. Mostamand, R. Li, B. B. Reich, and J. Lassen. Laser resonance ionization spectroscopy of even-parity autoionizing Rydberg states of thulium by laser resonance ionization spectroscopy. *To be submitted in Phys. Rev. A.*, (2019).

[26] A. Kramida, Yu. Ralchenko, J. Reader, and NIST ASD Team. *NIST Atomic Spectra Database (version 5.6.1),National Institute of Standards and Technology, Gaithersburg, MD*, (2018).

[27] R. F. Stebbings and F. B. Dunning. *Rydberg States of Atoms and Molecules*. Cambridge University Press, (1983).

[28] T. F. Gallagher. *Rydberg Atoms*. Cambridge University Press, (2005).

[29] I. L Beigman and V. S Lebedev. Collision theory of Rydberg atoms with neutral and charged particles. *Phys. Rep*, 250(3):95–328, (1995).

[30] N. Ramsey. *Molecular Beams*. OUP Oxford, (1956).

[31] Wolfgang Demtröder. *Atoms, Molecules and Photons*. Springer-Verlag, 2nd edition, (2010).

[32] P. J. Mohr, B. N. Taylor, and D. B. Newell. CODATA recommended values of the fundamental physical constants: 2010. *Rev. Mod. Phys*, 84(4), (2012).

[33] G. W. F. Drake and R. A. Swainson. Quantum defects and the 1/n dependence of Rydberg energies: Second-order polarization effects. *Phys. Rev. A*, 44(9):5448–5459, (1991).

[34] M. J. Seaton. Quantum defect theory. *Rep. Prog. Phys*, 46(2):167–257, (1983).

[35] J. P. Connerade. *Highly Excited Atoms*. Cambridge University Press, (1998).

[36] W. Ritz. *Gesammelte Werke Walter Ritz*. Paris: Gautier-Villars, (1911).

[37] T. R. Gentile, B. J. Hughey, D. Kleppner, and T. W. Ducas. Microwave spectroscopy of calcium Rydberg states. *Phys. Rev. A*, 42(1):440–451, (1990).

[38] J. von Neumann and E. P. Wigner. über merkwürdige diskrete Eigenwerte. In *The Collected Works of Eugene Paul Wigner*, pages 291–293. Springer Berlin Heidelberg, (1993).

[39] K. T. Lu and U. Fano. Graphic Analysis of Perturbed Rydberg Series. *Phys. Rev. A*, 2(1):81–86, (1970).

[40] I. V. Hertel and C.-P. Schulz. *Atoms, Molecules and Optical Physics 1: Atoms and Spectroscopy*. Springer-Verlag, (2015).

[41] U. Fano. Effects of configuration interaction on intensities and phase shifts. *Phys. Rev*, 124(6):1866–1878, (1961).

[42] B. A. Bushaw, W. Nörtershäuser, K. Blaum, and K. Wendt. Studies of narrow autoionizing resonances in gadolinium. *Spectrochim. Acta. B*, 58(6):1083–1095, (2003).

[43] S. Raeder. Spurenanalyse von Aktiniden in der Umwelt mittels Resonanzionisations-Massenspektrometrie. *PhD thesis, Johannes Gutenberg-Universität Mainz*, (2011).

[44] T. Gottwald. Studium hochkomplexer atomarer Spektren mittels Methoden der Laserresonanzionisation. *PhD thesis, Johannes Gutenberg-Universität Mainz*, (2010).

[45] D. Studer. Resonanzionisationsspektroskopie hochliegender Zustände in Dysprosium und Erbium zur Entwicklung effizienter Anregungsschemata und Bestimmung des ersten Ionisationspotentials. *Diploma, Johannes Gutenberg-Universität Mainz*, (2015).

[46] W. Demtröder. *Laser Spectroscopy*, volume 2. Springer Berlin Heidelberg, (2008).

[47] H. Haken and H. C. Wolf. *Atomic and Quantum Physics: An Introduction to the Fundamentals of Experiment and Theory*. Springer-Verlag, (1984).

[48] G. W. F. Drake. Springer handbook of atomic, molecular, and optical physics, (2006).

[49] H. N. Russell and F. A. Saunders. New regularities in the spectra of the alkaline earths. *J. Astrophys*, 61:38, (1925).

[50] R. Li, J. Lassen, J. Ruczkowski, A. Teigelhöfer, and P. Bricault. Laser resonance ionization spectroscopy of antimony. *Spectrochim. Acta. B*, 128:36–44, (2017).

[51] Sóti, Z., Magill, J., and Dreher, R. Karlsruhe nuclide chart 10th edition 2018. *EPJ Nuclear Sci. Technol.*, 5, (2019).

[52] E. B. Saloman. A resonance ionization spectroscopy/resonance ionization mass spectrometry data service. I—data sheets for As, B, Cd, C, Ge, Au, Fe, Pb, Si and Zn. *Spectrochim. Acta. B*, 45(1):37–83, (1990).

[53] E. B. Saloman. A resonance ionization spectroscopy/resonance ionization mass spectrometry data service. II—data sheets for Al, Ca, Cs, Cr, Co, Cu, Kr, Mg, Hg and Ni. *Spectrochim. Acta. B*, 46(3):319–378, (1991).

[54] E. B. Saloman. A resonance ionization spectroscopy/resonance ionization mass spectrometry data service: III—data sheets for Sb, Bi, P, Na and Sn. *Spectrochim. Acta. B*, 47(4):517–543, (1992).

[55] E. B. Saloman. A resonance ionization spectroscopy/resonance ionization mass spectrometry data service: IV—data sheets for Be, In, Li, K, Rb, Ag, Ti and V and an update of the data sheet for Ni. *Spectrochim. Acta. B*, 48(9):1139–1203, (1993).

[56] E. B. Saloman. A resonance ionization spectroscopy/resonance ionization mass spectrometry data service: V—data sheets for Ga, Mn, Sc and Tl. *Spectrochim. Acta. B*, 49(3):251–281, (1994).

[57] R. de Groote. Modeling and simulation of two-step resonance ionization processes using CW and pulsed lasers, (2013).

[58] N. V. Vitanov, B. W. Shore, L. Yatsenko, K. Böhmer, T. Halfmann, T. Rickes, and K. Bergmann. Power broadening revisited: theory and experiment. *Opt. Commun*, 199(1):117–126, (2001).

[59] M. L. Citron, H. R. Gray, C. W. Gabel, and C. R. Stroud. Experimental study of power broadening in a two-level atom. *Phys. Rev. A*, 16(4):1507–1512, (1977).

[60] A. Teigelhöfer. Isotope shift and hyperfine structure measurements on silver, actinium and astatine by in-source resonant ionization laser spectroscopy. *PhD thesis, University of Manitoba*, (2017).

[61] A. Agnesi, S. Dell'Acqua, and P. G. Gobbi. All-solid-state gain-switched Cr^{4+}:forsterite laser. *Opt. Commun*, 127(4):273–276, (1996).

[62] W. Koechner. *Solid-State Laser Engineering*. Springer-Verlag, 6th edition, (2006).

[63] C. Grüning, G. Huber, P. Klopp, J. V. Kratz, P. Kunz, G. Passler, N. Trautmann, A. Waldek, and K. Wendt. Resonance ionization mass spectrometry for ultratrace analysis of plutonium with a new solid state laser system. *Int. J. Mass. Spectrom*, 235(2):171–178, (2004).

[64] K. D. A. Wendt, K. Blaum, Ch. Geppert, R. Horn, G. Passler, N. Trautmann, and B. A. Bushaw. Laser resonance ionization for efficient and selective ionization of rare species. *Nuc. Instrum. Meth. B*, 204:325–330, (2003).

[65] E. Hecht. *Optics*. Addison Wesley, 4th edition, (2001).

[66] D. Albers. Assembly and characterization of a double-sided-pumped, high repetition rate titanium sapphire laser system. *M.Eng. thesis, Fachhochschule Oldenburg Ostfriesland Wilhelmshaven*, (2007).

[67] S. M. Kobtsev and N. A. Sventsitskaya. Application of birefringent filters in continuous-wave tunable lasers: a review. *Opt. Spectrosc*, 73:114–123, (1992).

[68] B. E. A. Saleh and M. C. Teich. *Fundamentals of photonics*. Hoboken, N.J. : Wiley-Intersci, 2nd edition, (2007).

[69] A. Teigelhöfer, P. Bricault, O. Chachkova, M. Gillner, J. Lassen, J. P. Lavoie, R. Li, J. Meißner, W. Neu, and K. D. A. Wendt. Grating tuned Ti:Sa laser for in-source spectroscopy of Rydberg and autoionizing states. *Hyperfine Interact*, 196:161–168, (2010).

[70] C. Mattolat. Spektroskopische Untersuchungen an Technetium und Silizium - Ein Festkörperlasersystem für die Resonanzionisationsspektroskopie. *PhD thesis, University of Mainz*, (2010).

[71] P. Naubereit. Entwicklung eines weitabtimmbaren hochrepetierenden Titan:Saphir-Lasers und Spektroskopie hochliegender Resonanzen an Holmium-165. *M.Sc. thesis, University of Mainz*, (2015).

[72] Y. Liu. ORNL developments in laser ion sources for radioactive ion beam production. *Hyperfine Interact*, 227(1):85–99, (2014).

[73] R. Li, J. Lassen, S. Rothe, A. Teigelhöfer, and M. Mostamand. Continuously tunable pulsed Ti:Sa laser self-seeded by an extended grating cavity. *Opt. Express*, 25(2):1123–1130, (2017).

[74] T. W. Hänsch. Repetitively pulsed tunable dye laser for high resolution spectroscopy. *Appl. Opt*, 11(4):895–898, (1972).

[75] R. D. Boyd, J. A. Britten, D. E. Decker, B. W. Shore, B. C. Stuart, M. D. Perry, and L. Li. High-efficiency metallic diffraction gratings for laser applications. *Appl. Opt*, 34(10):1697–1706, (1995).

[76] C. E. Webb and J. D. C. Jones. *Handbook of laser technology and applications*, volume 1. Principles. Institute of Physics, (2004).

[77] D. A. Fink, S. D. Richter, K. Blaum, R. Catherall, B. Crepieux, V. N. Fedosseev, A. Gottberg, and et al. On-line implementation and first operation of the laser ion source and trap at ISOLDE/CERN. *Nuc. Instrum. Meth B*, 344:83–95, (2015).

[78] S. Rothe. Aufbau eines Chrom:Forsterit lasers und Resonanzionisationsspektroskopie an Strontium, Titan, Nickel, Scandium und Silicium. *Diploma, Johannes Gutenberg-Universität Mainz*, (2009).

[79] V. Petričević, S. K. Gayen, R. R. Alfano, Kiyoshi Yamagishi, H. Anzai, and Y. Yamaguchi. Laser action in chromium-doped forsterite. *Appl. Phys. Lett.*, 52(13):1040–1042, (1988).

[80] R. Moncorge, G. Cormier, D. J. Simkin, and J. A. Capobianco. Fluorescence analysis of chromium-doped forsterite (Mg_2 SiO_4). *IEEE J. Quant. Electron*, 27(1):114–120, (1991).

[81] V. Petričević, S. K. Gayen, and R. R. Alfano. Laser action in chromium-activated forsterite for near-infrared excitation: Is Cr^{4+} the lasing ion? *Appl. Phys. Lett*, 53(26):2590–2592, (1988).

[82] W. Jia, H. Liu, S. Jaffe, W. M. Yen, and B. Denker. Spectroscopy of Cr^{3+} and Cr^{4+} ions in forsterite. *Phys. Rev. B*, 43(7):5234–5242, (1991).

[83] V. Petričević, S. K. Gayen, and R. R. Alfano. Laser action in chromium-activated forsterite for near infrared excitation. *Appl. Opt*, 27(20):4162–4163, (1988).

[84] A. Sennaroglu. Broadly tunable Cr^{4+}-doped solid-state lasers in the near infrared and visible. *Prog. Quant. Electron*, 26:287–352, (2002).

[85] T. Togashi, Y. Nabekawa, T. Sekikawa, and S. Watanabe. High-peak-power femtosecond Cr:forsterite laser system. *Appl. Phys. B*, 68(2):169–175, (1999).

[86] T. J. Carrig and C. R. Pollock. Tunable, CW operation of a multiwatt forsterite laser. *Opt. Lett*, 16(21):1662–1664, (1991).

[87] A. Sennaroglu, T. J. Carrig, and C. R. Pollock. Femtosecond pulse generation by using an additive-pulse mode-locked chromium-doped forsterite laser operated at 77 K. *Opt. Lett*, 17(17):1216–1218, (1992).

[88] S. G. Demos and R. R. Alfano. Upconverted luminescence from nonequilibrium vibronic states of Cr ions in forsterite. *Phys. Rev. B*, 46(14):8811–8817, (1992).

[89] A. A. Ivanov, B. I. Minkov, G. Jonusauskas, J. Oberlé, and C. Rulliére. Influence of Cr^{4+} ion concentration on cw operation of forsterite laser and its relation to thermal problems. *Opt. Commun*, 116(1):131–135, (1995).

[90] A. Sennaroglu and B. Pekerten. Determination of the optimum absorption coefficient in Cr^{4+}:forsterite lasers under thermal loading. *Opt. Lett*, 23(5):361–363, (1998).

[91] A. Sennaroglu and B. Pekerten. Experimental and numerical investigation of thermal effects in end-pumped Cr^{4+}:forsterite lasers near room temperature. *Quant. Electron., IEEE J.*, 34:1996–2005, (1998).

[92] A. Agnesi, E. Piccinini, and G. Reali. Threshold optimization of all-solid-state Cr:forsterite lasers. *J. Opt. Soc. Am. B*, 17(2):198–201, (2000).

[93] A. Sennaroglu. Analysis and optimization of lifetime thermal loading in continuous-wave Cr^{4+}-doped solid-state lasers. *J. Opt. Soc. Am. B*, 18(11):1578–1586, (2001).

[94] A. Sennaroglu, A. M. Kowalevicz, E. P. Ippen, and J. G. Fujimoto. Compact femtosecond lasers based on novel multipass cavities. *IEEE J. Quant. Electron*, 40(5):519–528, (2004).

[95] A. Sugimoto, Y. Nobe, T. Yamazaki, Y. Yamaguchi, K. Yamagishi, Y. Segawa, and H. Takei. Spectroscopic properties of Cr-doped and Cr,Li-doped synthetic forsterite crystals. *Phys. Chem. Min*, 24(5):333–339, (1997).

[96] Z. X. Jiang, I. T. McKinnie, L. A. W. Gloster, and T. A. King. Temporal and kinetic studies of chromium forsterite oscillators with 1064 nm laser excitation. *Pure. App. Opt*, 5:77, (1999).

[97] Z. X. Jiang, L. A. W. Gloster, H. Ahmad, and T. A. King. Laser characteristics of chromium doped forsterite with Ti:Sapphire laser excitation. *J. Mod. Opt*, 40(7):1411–1419, (1993).

[98] A. D. McNaught and A. Wilkinson. *IUPAC Compendium of Chemical Terminology- Gold Book*. IUPAC, Research Triagle Park, NC, 2.3.1 edition, (2012).

[99] Inc LEE Laser. *OPERATIONAL MANUAL MODEL LDP-100MQG DIODE – PUMPED LASER SYSTEMS*. LEE Laser, Inc. Orlando, Florida, (2009).

[100] K. Blaum, C. Geppert, H.-J Kluge, M. Mukherjee, S. Schwarz, and K. Wendt. A novel scheme for a highly selective laser ion source. *Nucl. Instrum. Meth. B*, 204:331–335, (2003).

[101] J. P Lavoie. Production of pure ion beams by laser ionization and a fast release RFQ. *PhD thesis, University of Laval*, (2010).

[102] J. P. Lavoie, P. Bricault, J. Lassen, and M. R. Pearson. Segmented linear radiofrequency quadrupole/laser ion source project at TRIUMF. *Hyperfine Interact*, 174(1):33–39, (2007).

[103] H. Heggen. Development of a radio frequency quadrupole- laser ion source (RFQ - LIS) for isobar suppression. *M.Sc thesis, Technische Universitat Darmstadt*, (2013).

[104] S. Raeder, H. Heggen, J. Lassen, F. Ames, D. Bishop, P. Bricault, P. Kunz, A. Mjϕs, and A. Teigelhöfer. An ion guide laser ion source for isobar-suppressed rare isotope beams. *Rev. Sci. Instrum*, 85(3):033309, (2014).

[105] S. Richter. Implementierung der Laserionenquellenfalle LIST bei ISOLDE und Validierung der Spezifikationen Effizienz und Selektivität. *PhD thesis, Johannes Gutenberg-Universität Mainz*, (2015).

[106] F. Schwellnus. Entwicklung von ionenquellen zur optimierung von selektivität und effizienz bei der resonanten laserionisation. *PhD thesis, Johannes Gutenberg-Universität Mainz*, (2010).

[107] D. A. Fink. Improving the selectivity of the ISOLDE resonance ionization laser ion source and in-source laser spectroscopy of polonium. *PhD thesis, Ruprecht-Karls-Universität Heidelberg*, 45(47), (2014).

[108] K. Wiest. Entwicklung des Laserionenquellen- und fallenprojekts LIST für Ultraspurendetektion und Grundlagenforschung. *PhD thesis, Johannes Gutenberg-Universität Mainz*, (2006).

[109] Y. Kudryavtsev, P. Creemers, R. Ferrer, C. Granados, L. Gaffney, and et al. A new in-gas-laser ionization and spectroscopy laboratory for off-line studies at KU leuven. *Nucl. Instrum. Meth. B*, 376, (2016).

[110] T. Kron, R. Ferrer-Garcia, N. Lecesne, V. Sonnenschein, S. Raeder, J. Rossnagel, and K. Wendt. Control of RILIS lasers at IGISOL facilities using a compact atomic beam reference cell. *Hyperfine Interact*, 216(1):53–58, (2013).

[111] R. Ferrer, V. T. Sonnenschein, B. Bastin, and et al. Performance of a high repetition pulse rate laser system for in-gas-jet laser ionization studies with the leuven laser ion source @ LISOL. *Nucl. Instrum. Meth. B*, 291:29–37, (2012).

[112] D. A. Dahl. SIMION for the personal computer in reflection. *Int. J. Mass. Spect.*, 200(3), (2000).

[113] W. Paul and M. Raether. Das elektrische Massenfilter. *Z. Physik*, 140(3):262–273, (1955).

[114] W. Paul, H. P. Reinhard, and U. von Zahn. Das elektrische Massenfilter als Massenspektrometer und Isotopentrenner. *Z. Physik*, 152(2):143–182, (1958).

[115] P. H. Dawson. Quadrupole mass spectrometry and its applications, (1976).

[116] R. E. March, R. J. Hughes, and John F. J. Todd. *Quadrupole Storage Mass Spectrometry*. Wiley, (1989).

[117] Z. Du, D. J. Douglas, and K. Nikolai. Elemental analysis with quadrupole mass filters operated in higher stability regions. *J. Anal. Atom. Spectrom*, 14:1111–1119, (1999).

[118] D. R. Denison. Operating parameters of a quadrupole in a grounded cylindrical housing. *J. Vac. Sci. Technol*, 8(1):266–269, (1971).

[119] J. Schulte, P. V. Shevchenko, and A. V. Radchik. Nonlinear field effects in quadrupole mass filters. *R. Sci. Instrum*, 70(9):3566–3571, (1999).

[120] J. R. Gibson and S. Taylor. Prediction of quadrupole mass filter performance for hyperbolic and circular cross section electrodes. *Rapid. Commun. Mass. Spectrom*, 14(18):1669–1673, (2000).

[121] J. R. Gibson and S. Taylor. Numerical investigation of the effect of electrode size on the behaviour of quadrupole mass filters. *Rapid. Commun. Mass. Spectrom*, 15(20):1960–1964, (2001).

[122] D. J. Douglas and N. V. Konenkov. Influence of the 6th and 10th spatial harmonics on the peak shape of a quadrupole mass filter with round rods. *Rapid. Commun. Mass. Spectrom.*, 16(15):1425–1431, (2002).

[123] D. Gerlich. Inhomogeneous RF fields: A versatile tool for the study of processes with slow ions. In *Advances in Chemical Physics*. John Wiley & Sons, Ltd, (2007).

[124] J. A. Richards, R. M. Huey, and J. Hiller. A new operating mode for the quadrupole mass filter. *Int. J. Mass. Spectrom*, 12(4):317–339, (1973).

[125] N. V. Konenkov, M. Sudakov, and D. J. Douglas. Matrix methods for the calculation of stability diagrams in quadrupole mass spectrometry. *J. Am. Soc. Mass. Spectrom*, 13(6):597–613, (2002).

[126] M. Sudakov and E. Nikolaev. Ion motion stability diagram for distorted square waveform trapping voltage. *Eur. Mass. Spectrom*, 8, (2002).

[127] C. Niculae and M. Niculae. Numerical method for calculating of potential distribution in non-ideal multipole ion guides. *Optoelectron. Adv. Mater.- Rapid. Commun*, 3:1073–1075, (2009).

[128] W.C. Martin, R. Zalubas, and L. Hagan. *Atomic energy levels–the rare-earth elements*. NSRDS-NBS. U.S. Dept. of Commerce, NBS, (1978).

[129] J. Sugar, W. F. Meggers, and P. Camus. Spectrum and energy levels of neutral thulium. *Res. NBS*, 77A, (1973).

[130] E. Vidolova-Angelova, G. I. Bekov, L. N. Ivanov, V. Fedoseev, and A. A. Atakhadjaev. Laser spectroscopy investigation of highly excited states of the Tm atom. *J. Phys. B*, 17(6):953–961, (1984).

[131] E. P. Vidolova-Angelova, D. A. Angelov, S. T. Mincheva, V. N. Fedoseev, V. I. Mishin, and A. D. Zuzikov. Rydberg and autoionization Tm states investigation by the three-step laser

excitation and electric field ionization method. *Z. Phys. D - Atoms, Molecules and Clusters*, 5(4):287–292, (1987).

[132] E. P. Vidolova-Angelova, D. A. Angelov, S. T. Mincheva, V. N. Fedoseev, V. I. Mishin, and A. D. Zuzikov. Tm autoionization rydberg states in the vicinity of the third and fourth atomic ionization limit. *Z. Phys. D - Atoms, Molecules and Clusters*, 13(2):115–121, (1989).

[133] A. A. Atakhodzhaev and V. N. Fedoseev. Laser photoionization spectroscopy of autoionization states of the thulium atom. *J. Appl. Spectrosc*, 45(3):915–919, (1986).

[134] A.A. Kwiatkowski, W. Plass, M. Reiter, C. Andreoiu, and et.al. Mass measurements of n=82 lanthanides, isotopes around z=70. *Proposal to the ISAC and subatomic physics Experiments Evaluation Committee (SAP-EEC), TRIUMF*, (2017).

[135] J. P. Lavoie, R. Li, P. Bricault, J. Lassen, O. Chachkova, and A. Teigelhöfer. A test stand for off-line laser ion source development at TRIUMF. *Rev. Sci. Instrum*, 84(1):013306, (2013).

[136] R. Li, J. Lassen, A. Teigelhöfer, J. P. Lavoie, P. Bricault, O. Chackakova, J. Meissner, and Y. Zlateva. Resonant Ionization Laser Ion Source (RILIS) off-line developments on Ga, Al and Ca. *Nucl. Instrum. Methods A*, 308:74–79, (2013).

[137] A. Teigelhöfer, J. Lassen, Z. Abboud, P. Bricault, H. Heggen, P. Kunz, R. Li, T. Quenzel, and S. Raeder. Yttrium ionization scheme development for Ti:Sa laser based RILIS. *Hyperfine Interact*, 216(1):65–70, (2013).

[138] S. Raeder, M. Dombsky, H. Heggen, J. Lassen, T. Quenzel, M. Södin, A. Teigelhöfer, and K. Wendt. In-source laser spectroscopy developments at TRILIS - towards spectroscopy on actinium and scandium. *Hyperfine Interact*, 216:33–39, (2013).

[139] R. Li, J. Lassen, Z. P. Zhong, F. D. Jia, M. Mostamand, X. K. Li, B. B. Reich, A. Teigelhöfer, and H. Yan. Even-parity Rydberg and autoionizing states of lutetium by laser resonance-ionization spectroscopy. *Phys. Rev. A*, 95(5):052501, (2017).

[140] M. Aymar, C. H. Greene, and E. Luc-Koenig. Multichannel Rydberg spectroscopy of complex atoms. *Rev. Mod. Phys*, 68(4):1015–1123, (1996).

[141] H. Friedrich. *Theoretical Atomic Physics*. Springer International Publishing, (2017).

[142] P. Camus and J. Sugar. Etude théorique et interprétation des configurations électroniques de Tm II I. Configurations paires $4f^{12}(5d + 6s)^2 + 4f^{13}6p$. *Physica. Scripta*, 4:257–261, (1971).

[143] P. Kunz, C. Andreoiu, P. Bricault, M. Dombsky, J. Lassen, A. Teigelhöfer, H. Heggen, and F. Wong. Nuclear and in-source laser spectroscopy with the ISAC yield station. *Rev. Sci. Instrum*, 85(5):053305, (2014).

[144] R. D. Cowan. *The theory of atomic structure and spectra*. Berkeley : University of California Press, (1981).

[145] C. E. Moore. *Atomic Energy Levels*, volume III. NBS Circ. Washington, D.C, (1958).

[146] W. R. S. Garton and M. Wilson. AutoIonization Rydberg series in the spectrum of La I. *J. Astrophys.*, 145, (1966).

[147] P. Xue, X. Y. Xu, W. Huang, C. B. Xu, R. C. Zhao, and X. P. Xie. Observation of the highly excited states of lanthanum. *AIP Conference Proceedings*, 388(1):299–302, (1997).

[148] E. Eliav, S. Shmulyian, U. Kaldor, and Y. Ishikawa. Transition energies of lanthanum, actinium, and eka-actinium (element 121). *J. Chem. Phys.*, 109(10):3954–3958, (1998).

[149] B. Kara¸coban and L. Özdemir. Transition energies of neutral and singly ionized lanthanum. *Indian. J. Phys*, 84(3):223–230, (2010).

[150] F. Güzelçimen, I. Siddiqui, G. Başar, S. Kröger, and L. Windholz. New energy levels and hyperfine structure measurements of neutral lanthanum by laser-induced fluorescence spectroscopy. *J. Phys. B*, 45(13):135005, (2012).

[151] F. Güzelçimen, M. Tonka, Z. Uddin, N. A. Bhatti, L. Windholz, S. Kröger, and G. Başar. Revised energy levels of singly ionized lanthanum. *J. Quant. Spectrosc. Ra*, 211:188–199, (2018).

[152] S. Raeder, H. Heggen, A. Teigelhöfer, and J. Lassen. Determination of the first ionization energy of polonium by resonance ionization spectroscopy - part I: Measurement of even-parity Rydberg states at TRIUMF-ISAC. *Spectrochim. Acta. B*, 151:65–71, (2019).

[153] J. Mague. Gmelin Handbook of Inorganic Chemistry. 8th edition. *Organometallics*, 3(6):948–948, (1984).

[154] J. Dilling, D. Lunney, and et al. Mass measurements of astatine isotopes. *Letter of intent to the ISAC and subatomic physics Experiments Evaluation Committee (SAP-EEC), TRIUMF*, (2011).

[155] T. J. Ruth, et al. Radiochemistry of elements. Radiochemistry of Astatine. *Nucl. Sci. Ser*, (3064), (1988).

[156] Amin I. Kassis. Therapeutic radionuclides: biophysical and radiobiologic principles. *Semin. Nucl. Med*, 38(5):358–366, (2008).

[157] M. R. McDevitt, et al. Radioimmunotherapy with alpha-emitting nuclides. *Eur. J. Nucl. Med. Mol.*, 25(9):1341–1351, (1998).

[158] M. R. Zalutsky and G. Vaidyanathan. Astatine-211-labeled radiotherapeutics: an emerging approach to targeted alpha-particle radiotherapy. *Curr. Pharm. Design*, 6(14):1433–1455, (2000).

[159] L. P. Gaffney, et al. Studies of pear-shaped nuclei using accelerated radioactive beams. *Nature*, 497(7448):199–204, (2013).

[160] L. Ghys. Beta-delayed fission in proton-rich nuclei in the lead region. *PhD thesis, KU Leuven*, (2015).

[161] V. L. Truesdale and et al. β -delayed fission and α decay of ^{196}At. *Phys. Rev. C*, 94(3):034308, (2016).

[162] J. G. Cubiss and et al. Charge radii and electromagnetic moments of $^{195\text{-}211}$At. *Phys. Rev. C*, 97(5):054327, (2018).

[163] Nele Kesteloot and et al. Deformation and mixing of coexisting shapes in neutron-deficient polonium isotopes. *Phys. Rev. C*, 92, (2015).

[164] A. M. Oros, K. Heyde, and et al. Shape coexistence in the light Po isotopes. *Nucl. Phys. A*, 645(1):107–142, (1999).

[165] P. A. Butler. Octupole collectivity in nuclei. *J. Phys. G*, 43(7):073002, (2016).

[166] T. Grahn and et al. Collective 2+1 excitations in ^{206}Po and ^{208,210}Rn. *Eur. Phys. J. A*, 52(11):340, (2016).

[167] P. A. Butler, J. Cederkall, and P. Reiter. Nuclear-structure studies of exotic nuclei with MINIBALL. *J. Phys. G*, 44(4):044012, (2017).

[168] R. McLaughlin. Absorption Spectrum of Astatine. *J. Opt. Soc. Am*, 54(8):965–967, (1964).

[169] S. Raeder, et al. In-source spectroscopy on astatine and radium for resonant laser ionization. *Hyperfine Interact*, 227(1-3):77–83, (2014).

[170] S. Rothe, et al. Measurement of the first ionization potential of astatine by laser ionization spectroscopy. *Nat. Commun*, 4:1835, (2013).

[171] A. Teigelhöfer. Astatine and yttrium resonant ionization laser spectroscopy. *M.Sc thesis, University of Manitoba*, (2012).

[172] J. Lassen and et al. In-source laser spectroscopy of At - search for auto-ionizing atomic states. *Proposal to the ISAC and Experiments Evaluation Committee (EEC), TRIUMF, https://mis.triumf.ca/science/experiment/view/S1703*, (2016).